DISSERTATION

ON INTENSITY CHANGE AND THE EFFECTS OF SHORTWAVE RADIATION ON TROPICAL CYCLONE RAINBANDS

Submitted by

Benjamin Trabing

Department of Atmospheric Science

In partial fulfillment of the requirements

For the Degree of Doctor of Philosophy

Colorado State University

Fort Collins, Colorado

Fall 2020

Doctoral Committee:

Advisor: Michael Bell

Christine Chiu
John Knaff
Bret Windom
Sue van den Heever

ABSTRACT

ON INTENSITY CHANGE AND THE EFFECTS OF SHORTWAVE RADIATION ON TROPICAL CYCLONE RAINBANDS

In this dissertation, the effects of shortwave radiation and the diurnal cycle of radiation on tropical cyclone rainbands are explored. In order to improve short term forecasts of tropical cyclone intensity and size, a better understanding of the processes that affect the inner rainbands of tropical cyclones is warranted. In Chapter 2, the distribution of intensity forecast errors from the National Hurricane Center (NHC) are characterized in the Atlantic and East Pacific basins. Analysis of the forecast error distributions and the relationship between the thermodynamic environments in which those errors occur leads to the conclusion that improvements need to be made to our understanding and prediction of inner-core processes, particularly to predict rapid changes in intensification and weakening.

The effect of shortwave radiation on tropical cyclone rainbands during an eyewall replacement cycle (ERC) is examined in Chapter 3. In the idealized experiments we vary the amount of incoming solar radiation to change the magnitude of the response and assess the sensitivity of the timing of the ERC. Shortwave radiation has a delaying effect on the ERC primarily through its modifications of the distribution of convective and stratiform heating profiles in the rainbands. Shortwave radiation reduces the amount and strength of convective heating profiles by stabilizing the thermodynamic profiles and reducing convective available potential energy. The idealized modeling study shows that the coupled interactions between the shortwave radiation and the cloud microphysics is at the crux of the experiment and requires further verification by observations.

Chapter 4 explores the diurnal cycle of convection in the rainbands of Typhoon Kong-rey (2018) using a suite of novel observations from the Propagation of Intraseasonal Tropical Oscillations (PISTON) field campaign. Convection in the rainbands of Typhoon Kong-rey had a more pronounced diurnal cycle compared to the rest of PISTON where shortwave heating in the upper-levels increased the static stability during the day. Pronounced diurnal oscillations in the brightness temperatures, which are out of phase with those documented in Dunion et al. (2014), are found to be coupled with outflow jets below the tropopause and radially outward propagating convective rainbands approximately ∼6 hours later.

In Chapter 5 an attempt is made to simulate the diurnal variations in the rainbands of Typhoon Kong-rey that were observed during PISTON. Four experiments are conducted using commonly used shortwave radiation and cloud microphysics schemes to determine the extent to which previous and future studies can reproduce diurnal variability. Of the four experiments, only one realistically simulated Typhoon Kong-rey's rapid intensification and none of the experiments reproduce the diurnal oscillations in the infrared brightness temperatures. The interactions between the shortwave radiation and cloud microphysics schemes cause variations in the distribution of convective and stratiform precipitation in the inner-rainbands and the extent of upper-level clouds that can largely explain the differences in the intensity. Sensitivity tests suggest that more work on documenting radiation-microphysics interactions is needed to improve model forecasts of inner-rainband structure.

ACKNOWLEDGMENTS

This work would not have been possible without support from numerous people who have helped me over the course of my life. I would like to first acknowledge and thank my advisor Michael Bell for the opportunity to complete my Masters and PhD with his wonderful group. I would also like to thank my committee members Christine Chiu, John Knaff, Bret Windom, and Sue van den Heever for their support. I recognize that my first experience conducting research at CSU with John Knaff and Kate Musgrave through the NOAA Hollings Scholar Program inspired to me to continue to learn and pursue graduate studies at CSU. I would have never made it to CSU without the help I received from Sophia Morren and the McNair Scholars Program at the University of Oklahoma.

I thank all of my family and friends for all that they have done for me. I would like to especially thank all the members of the Bell group for their friendship, encouragement, and lively scientific discussions. I have strongly benefited from the technical support on the Maui compute cluster from Bruno Melli and programming help from Jon Martinez and Chris Slocum. I would like to thank all the faculty and staff in the Department of Atmospheric Science for answering all my questions and helping me navigate through the program. I thank Steve Rutledge for providing support to allow my to take part in the PISTON field campaign which allowed me to collect first-hand the observations that I will be exploring here.

A special thanks goes to Oliver and Daisy for the welcome distractions but persistent motivation. This work would not have been possible without the support, motivation and love from Amberly.

This work has been funded by the Office of Naval Research Awards N000141613033, N000141712230, and N000142012069, and National Science Foundation award AGS-1701225. Computing resources were provided by the Texas Advanced Computing Center under grant request ATM190001.

DEDICATION

I would like to dedicate this dissertation to my wonderful wife Amberly and my two kids, Oliver and Daisy. I could not have finished without their love and support.

TABLE OF CONTENTS

LIST OF TABLES

LIST OF FIGURES

CHAPTER 1

INTRODUCTION

1.1 MOTIVATION

In order to mitigate losses from tropical cyclones (TCs) in the future and provide accurate impact-based forecasts, more precise forecasts of track, intensity, and storm size are required. Although track forecasts have been improving at a statistically significant rate over the decades, improvements to intensity and size forecasts remain a top research priority for the Hurricane Forecast Improvement Project (HFIP; Marks et al. 2019). The inner-core rainbands[1] play an important role in affecting the size[2] and intensity of tropical cyclones through processes such as eyewall replacement cycles (ERCs) and are therefore important to forecast. Hurricane Maria (2017) underwent an ERC just prior to making landfall in Puerto Rico which caused a slight weakening of the maximum winds but tripled the size of the eye causing the strongest winds to effect a larger area. As a result, Hurricane Maria became the third costliest hurricane in United States history behind only Hurricane Katrina (2005) and Hurricane Harvey (2017) earlier that year (Pasch et al. 2019). The processes that affect storm size and intensity are critical to understand and forecast because they are correlated with the damage potential of hurricanes (Powell and Reinhold 2007) and the storm surge risk (Irish et al. 2008). It is posited that through an enhanced understanding of processes in the inner rainbands, improved forecasts of TC size and intensity will result that could potentially save lives.

At the National Hurricane Center (NHC), mesoscale models such as the Hurricane Weather Research and Forecasting (HWRF) model have shown increasing skill in short term intensity forecast (Cangialosi et al. 2020). The mesoscale models are convection resolving and are able to explicitly resolve the inner-core structure of tropical cyclones and in some cases simulate ERCs, although it is unclear how skillful those forecasts are since they are difficult to verify. ERCs are difficult to forecast because they are driven by the inner-core dynamics and can cause substantial intensity forecast errors in the Statistical Hurricane Intensity Prediction Scheme (SHIPS), which is one of the primary intensity guidance models used by NHC (Kossin and DeMaria 2016). Before intensity forecast errors can be improved, which are negatively affected by ERCs, that factors contribute to intensity forecast errors

[1] Inner rainbands are loosely defined as the region of convective and stratiform precipitation between approximately 100-200 km from the TC center in the simulations observed in this dissertation. This definition is flexible and not driven solely based on the radius of maximum winds (RMW) because the RMW varies throughout time and between experiments which will be shown later.

[2] Here the size is in reference to the radius of maximum winds.

must be understood. By characterizing the error distributions and the thermodynamic environments in which large errors occur, future work can be target and reduce those errors. To improve both size and intensity forecasts, a better understanding of the processes in the inner rainbands, particularly in numerical models and during ERCs, is motivated.

One critical but often overlooked source of model error comes from the radiation scheme and the interactions with the cloud microphysics schemes. Modeling studies examining TCs often neglect or use idealized radiation schemes because radiation adds non-linear feedbacks that often complicates understanding of the system Nolan (2007); Rios-Berrios (2020). Fovell et al. (2016) showed that the radiation schemes and sensitivities with the microphysics parameters had an effect on the TC motion, strength and size of the wind field, inner-core diabatic heating asymmetries, outer-core convection, and the characteristics of the anvil clouds. In order to improve weather prediction models, comparisons between observations and the numerical models are needed; however, observation of the diurnal variability within the rainbands of TCs are difficult to attain and detailed comparisons with models have been lacking (Fovell et al. 2016). Because radiation schemes are computationally expensive, forecast models do not calculate radiative heating tendencies at each time step and often use oversimplified radiation schemes to reduce model latency. It is therefore a goal of this dissertation to improve the scientific community's understanding of the interactions between cloud microphysics and shortwave radiation schemes by comparing observations with both idealized modeling studies and realistic case studies.

1.2 Research Objectives

It is the goal of this work to advance our understanding of inner rainbands and the complex interactions with shortwave radiation to improve forecasts of size and intensity on short timescales (<48 hours). This goal will be achieved through four somewhat independent studies which will be introduced below. Each of the objectives of this work will be the topic of a chapter with more background into each topic discussed in the introduction to each chapter. The objectives of this dissertation are to:

- Characterize the error distributions for intensity forecasts and diagnose the environments in which large errors occur.
- Assess the sensitivity of eyewall replacement cycles to shortwave radiation.
- Explore the diurnal oscillations in the inner-rainbands of Typhoon Kong-rey from a suite of novel observations.

- Evaluate how different shortwave radiation and cloud microphysics schemes resolve the diurnal oscillations in Typhoon Kong-rey.

CHAPTER 2

UNDERSTANDING ERROR DISTRIBUTIONS OF HURRICANE INTENSITY FORECASTS DURING RAPID INTENSITY CHANGES [1]

2.1 INTRODUCTION TO INTENSITY FORECASTS

In 2009, the Hurricane Forecast Improvement Project (HFIP) was established with the goal of improving both track and intensity forecasts (Gall et al. 2013). It is well accepted that track forecasts have greatly improved and DeMaria et al. (2014) showed that hurricane intensity guidance has also improved at all forecast times on average at a statistically significant level. However, the prediction of rapid intensification (RI) and rapid weakening (RW) have shown little improvement and remain one of the highest-priority forecast challenges for forecasters at the National Hurricane Center (NHC) and other forecast agencies (Gall et al. 2013). RI and RW prediction is particularly critical for hurricanes approaching land with major implications on emergency management operations. It is important to understand the characteristics of the distribution of operational intensity forecast errors and not just the average error in order to improve intensity forecasts. Understanding how both RI and RW contribute to overall intensity forecast error distributions is a necessary step in improving RI and RW forecasts that has yet to be fully studied.

Rapid change in hurricane intensity is influenced by the large-scale environment, inner-core dynamics, and oceanic processes and requires detailed information across multiple scales to improve forecast skill (Kaplan et al. 2010). Hendricks et al. (2010) showed statistical differences between the environments of hurricanes that underwent RI and those that did not. An important finding of their study is that the rate of intensification is only weakly dependent on environmental conditions given a favorable environment, indicating the importance of inner-core dynamics to intensification rate. In the current study, whether official intensity forecast errors have a similar dependence on key large-scale environmental conditions is investigated.

Both RI and RW strongly affect intensity forecast errors (Kaplan et al. 2010; Wood and Ritchie 2015), although less attention has been given to RW prediction. RW events can often be attributed to landfall

[1] The content of this chapter has been published in Weather and Forecasting by the American Meteorological Society. Some formatting modifications were made to the text. The complete bibliographic citation of the original source follows: Trabing, B. C. and Bell, M. M., 2020: Understanding Error Distributions of Hurricane Intensity Forecasts during Rapid Intensity Changes, *Wea. Forecasting* . DOI:10.1175/WAF-D-19-0253.1

but a significant number of RW events take place over water. RW events associated with landfall generally have lower forecast errors because substantial weakening is already predicted, but track errors can lead to large intensity errors due to changes in the forecasted time of landfall. Wood and Ritchie (2015) found that over-ocean RW events occur when hurricanes transition to environments with low convective available potential energy, cold sea-surface temperature (SST), decreasing mid-level relative humidity (RH), and strong vertical wind shear. Over-ocean RW can also occur in somewhat favorable environments (Liang et al. 2016), in which case the inner-core dynamics may also become important. Little work has been done to examine the inner-core processes associated with over-ocean RW or evaluate the errors associated with RW.

A recent study by Na et al. (2018) showed a strong anti-correlation between operational forecast errors and intensity change. Official forecasts struggle with rapid intensity changes which leads to underestimates of hurricane intensity during RI and overestimates during RW (Cangialosi and Franklin 2014). A limited increase in official forecast skill of RI prediction, relative to persistence and climatology, in recent years was shown by Kaplan et al. (2015), but it is unclear how skillful RW forecasts have been and whether forecast biases have improved. With the improvement of operational intensity models and statistical RI guidance, it is important to understand whether the distributions have narrowed for RI and RW forecast errors or the average errors have improved over the years. Additionally, it is important to know whether over-ocean or landfall RW guidance has improved or not, and if there have been changes to forecast biases at different lead times.

Van Sang et al. (2008) showed that there may be an intrinsic predictability limit of the mesoscale processes in hurricanes that contribute to RI; however, Emanuel and Zhang (2016) showed that there is still a large gap between current intensity forecast skill and what is theoretically achievable. It is thought that improved models, better observations, and superior data assimilation techniques will lead to more accurate intensity forecasts (Emanuel and Zhang 2016). The representation of the mesoscale properties of the inner-core in forecast models is suggested to be critical for forecasting rapid intensity changes. The modeling study of Aberson et al. (2015) showed that assimilating Doppler radar observations improved short term intensity forecasts but did not show significant improvements to forecasting RI. The inner-core dynamics have been shown to be important in understanding Hurricane Patricia's (2017) both record-breaking RI and over-ocean RW (Doyle et al. 2017; Rogers et al. 2017; Martinez et al. 2019). Nystrom and Zhang (2019) found that assimilating inner-core radial velocities in Hurricane Patricia resulted in better forecasts of RI and a 40% reduction in forecast errors. In addition to intensity

guidance from dynamical models, the development and implementation of the Statistical Hurricane Prediction Scheme (SHIPS) Rapid Intensification Index (RII) has played a significant role in RI prediction and is a key operational forecast tool at NHC (Rozoff and Kossin 2011; Kaplan et al. 2015; Cangialosi et al. 2020). SHIPS-RII uses linear discriminant analysis in addition to a Bayesian and logistic regression model to create probabilistic RI guidance. The creation and improvement of the SHIPS decay model (DSHP) has provided guidance for land interactions, but a similar forecast tool explicitly for over-ocean RW has yet to be developed (Kaplan and DeMaria 1995; DeMaria et al. 2006).

The purpose of this study is to evaluate the characteristics and distributions of intensity forecast errors and demonstrate the relative contributions to the forecast errors from both RI and RW events. The spatial and temporal distributions will be analyzed in conjunction with environmental data to highlight where improvements can be made in forecasting RI and RW. Section 4.2 will discuss the data and RI/RW definitions used in this study. Section 4.4 will show the distributions of intensity forecast errors and the contributions from RI and RW. Section 4.3 will show the distribution of RI and RW errors in association with key environmental variables. Finally, section 4.5 will summarize and discuss the results of this study.

2.2 Data and Methods

In this study, the operational intensity forecasts of the maximum sustained (1-minute average) surface (10 m) winds at 6 hour intervals are analyzed. This study examines the NHC operational intensity forecast errors in the North Atlantic and East Pacific (East of 140W) from 1989–2018. The intensity and track forecast error statistics from NHC can be found online (`http://www.nhc.noaa.gov/verification/verify7.shtml`). This 30 year dataset includes tropical cyclones stronger than 20 kt and excludes extratropical stages and dissipation forecasts. These exclusions are consistent with the verification rules used by NHC and the Joint Typhoon Warning Center (JTWC) (DeMaria et al. 2014). Forecast intensity errors are defined as the difference between the forecasted intensity and the best track intensity at the verifying forecast time. Note that the absolute value of each intensity error is used to calculate the mean absolute error (MAE).

In this study, RI is considered over several forecast periods extending out to 48 hours to include when NHC issues watches and warnings. Intensity change is calculated over 12-h, 24-h, 36-h, and 48-h forecasts and the official forecast errors associated with those changes. Although there is some correlation with the previous time period, each forecast is treated as being independent to evaluate the

full distribution and improve sample size. The same definitions that are employed by SHIPS RII is used to categorize RI for the four forecast periods which are found in Kaplan et al. (2010). RI is therefore defined as an increase of at least 20 kt in 12 hours, 30 kt in 24 hours, 45 kt in 36 hours, and 55 kt in 48 hours. The same definitions for RI but corresponding to negative intensity changes are used to categorize RW over the same time periods for consistency, although past studies have used varying definitions (e.g. Liang et al. (2016): 20 kt in 24 h, Aberson et al. (2015): 25 kt in 24 h, Wood and Ritchie (2015): 30 kt in 24 h). The 24-h RI definition is consistent with that used by Na et al. (2018) and originally defined by Kaplan and DeMaria (2003). The values within the brackets shown in Table 2.1 are the number of events in the sample for each forecast length and basin.

Environmental variables are obtained from the SHIPS developmental dataset which extends from 1982-2017 in both the Atlantic and East Pacific (DeMaria et al. 2005). The SHIPS data is reduced to 1989-2017 based on the availability of NHC operational intensity forecast errors for the analysis. The SHIPS developmental database is based on the gridded analysis from the National Center for Environmental Prediction (NCEP) global forecast system (GFS) and was used to derive the SHIPS-RII. Environmental variables from SHIPS are used to evaluate the relationship between the thermodynamic environment and forecast errors. A focus is placed on 850–200 hPa deep layer vertical wind shear, Reynolds SST, and 850–700 hPa RH which have been shown to be important predictors for distinguishing RI and RW (Kaplan and DeMaria 2003; Hendricks et al. 2010; Kaplan et al. 2015). The 850–200 hPa vertical wind shear is averaged within a 500 km radius after the vortex circulation is removed from the background flow. The 850–700 hPa RH is averaged over the 200-800 km radii. Because the deep-layer vertical wind shear and mid-level RH are averaged over annuli, asymmetries in the environment are not well resolved and cannot be assessed in this study.

In order to understand the total distributions of RW events, landfall events are included in the statistics. Landfall events are included unless otherwise noted, as they contribute to a large distribution of forecast errors to be shown later. RW events that are attributed to land interactions versus over-water events are distinguished using the distance to land (DTL) variable in the SHIPS developmental database. RW due to land interactions will be identified based on whether the storm is within 50 km of any coastline. Major landmasses in addition to mountainous and large islands such as Puerto Rico and Jamaica are included in DTL, however, it is assumed that small relatively flat islands have negligible effects on rapid intensity changes (DeMaria et al. 2006).

TABLE 2.1. Official intensity forecast errors for the North Atlantic and East Pacific for the 12-h, 24-h, 36-h, and 48-h forecasts. The mean absolute error for only RI and RW events, all events, and all events excluding RI and RW are shown in kt. The last line is the percentage of MAE reduction relative to the total errors for each category. The units are in the parentheses and the numbers in the brackets are the number of events.

1989-2018	North Atlantic				East Pacific			
Forecast Period	12 h	24 h	36 h	48 h	12 h	24 h	36 h	48 h
MAE for RI/RW (kt)	15.78	21.56	29.57	33.37	14.67	20.99	28.53	31.86
[Number of Events]	[763]	[847]	[473]	[404]	[1090]	[1391]	[920]	[771]
MAE (kt)	6.17	9.58	12.05	14.21	6.11	10.48	13.76	15.84
[Number of Events]	[8403]	[7565]	[6767]	[6002]	[8766]	[7733]	[6762]	[5853]
MAE without RI/RW (kt)	5.21	8.06	10.73	12.83	4.90	8.17	11.43	13.41
[Number of Events]	[7640]	[6718]	[6294]	[5598]	[7676]	[6342]	[5842]	[5082]
MAE Reduction without RI/RW (kt)	.96	1.52	1.32	1.38	1.21	2.31	2.33	2.43
MAE Reduction (%)	15.6	15.9	10.9	9.7	19.8	22.0	16.9	15.3

2.3 FORECAST ERROR DISTRIBUTIONS

Figure 2.1 shows the relationship between official intensity errors and the change in surface wind speeds for the four forecast periods analyzed in this study. The RI and RW definitions for the forecast period are denoted by vertical red and blue lines, respectively, showing that the largest error magnitudes typically occur with RI and RW. The anti-correlation between intensity change and forecast errors is similar to that shown in the 24-h time period in Na et al. (2018), but here the analysis is expanded with the addition of multiple forecast periods. Forecast errors and intensity change have a correlation around -0.7 at all forecast times and are statistically significant at the 99.9% confidence level. As expected, when the forecast length increases, the distribution of forecast errors widens to include a larger range of errors. The distribution of errors between the Atlantic and East Pacific are similar at the 12-h and 24-h forecast periods, but as the forecast period length grows, the distribution widens faster in the East Pacific compared to the Atlantic. In the 36-h and 48-h distributions for the Atlantic, the larger absolute intensity forecast errors are shifted more toward RI events than RW events. East Pacific hurricanes are more prone to strong weakening events compared to the Atlantic, due in part to the climatologically unfavorable SST to the north and west of the basin. The wider distributions of errors in the East Pacific at longer forecast times could also be due to the effects of track errors along more common gradients of SST or shear. While longer forecast lead times are not analyzed in detail in this study, it is noted that the error distributions for intensity forecasts do not continue to widen with increasing lead time beyond 48 hours. Figure 2.2 shows the forecast error distributions normalized by

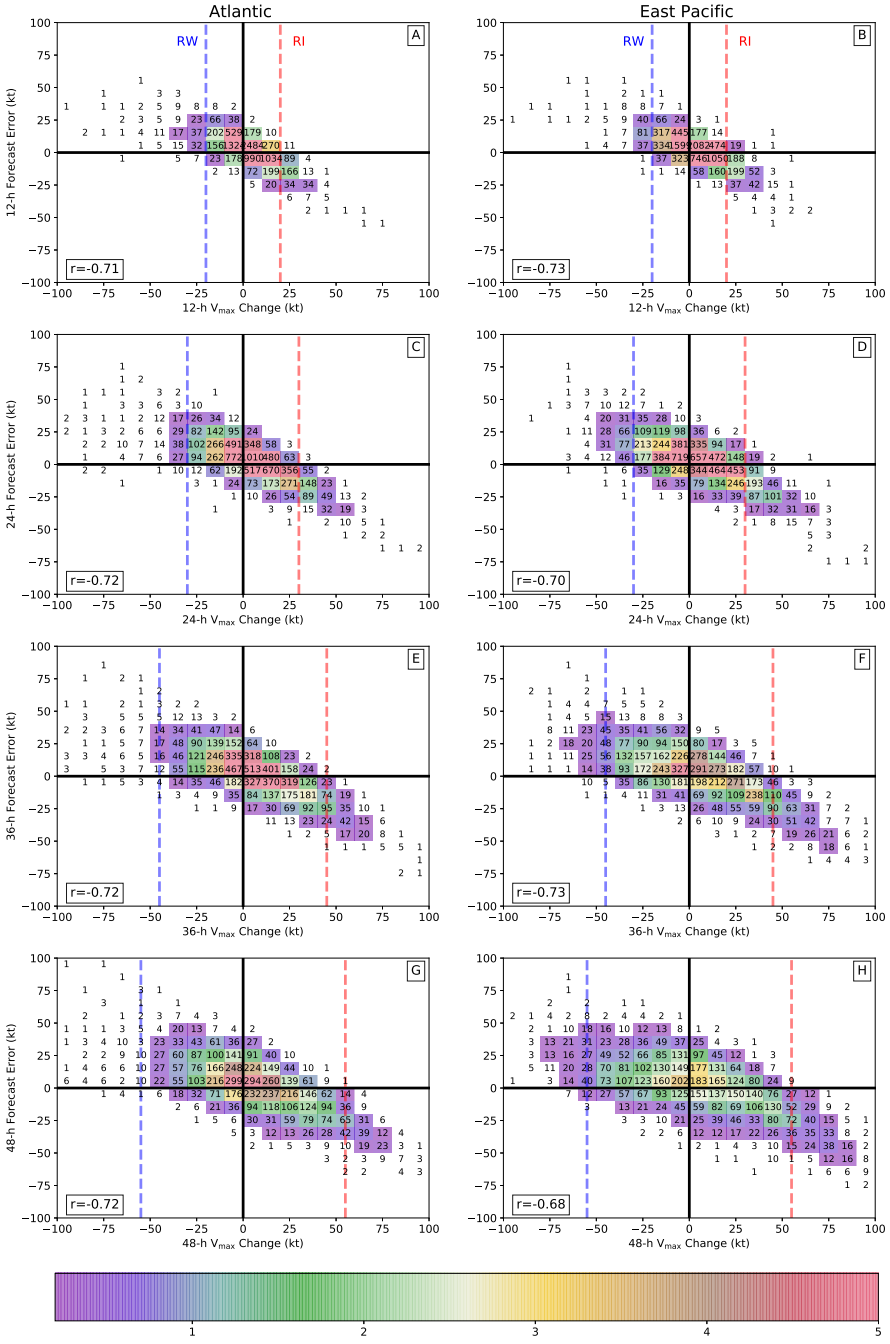

FIG. 2.1. Distribution of NHC official forecast errors and the corresponding intensity change for the Atlantic (a, c, e, g) and East Pacific (b, d, f, h) binned at 10 kt intervals. The 12-h (a, b), 24-h (c, d), 36-h (e, f), and 48-h (g, h) forecasts correspond to the wind speed change over that same duration of time. The colored boxes are normalized by the total number of events and are shaded by the % of the total. Bins that make up <.2% of the total are not shaded. The zero forecast error and zero intensity change lines are black. The correlation coefficient is shown for each curve which are all statistically significant at the 99.9% confidence level. The RI definition for each forecast length is shown by the red dashed lines and RW definition is shown by the blue dashed lines. For reference, the zero intensity change and zero error forecasts are found in the square above and to the right of the origin.

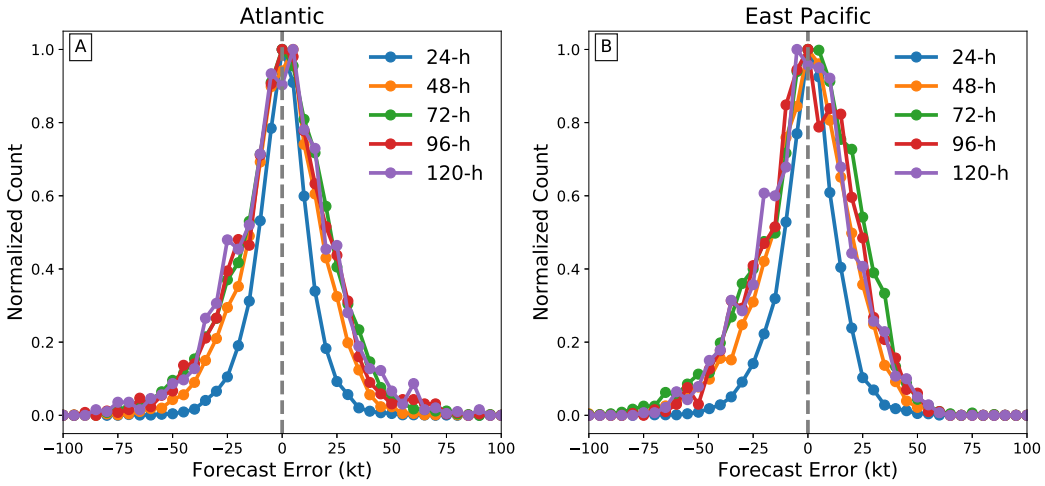

FIG. 2.2. Distribution of NHC official intensity forecast errors for forecasts lengths from 24 h to 120 h. The forecast errors for the Atlantic (a) and East Pacific (b) are normalized by the maximum number of events.

the maximum number of events for forecasts between 24–120 h. The normalized forecast error distributions for forecasts longer than 48 h are similar, suggesting that there is an intrinsic limit on the magnitude of intensity errors. The forecast error distributions for forecasts longer than 48 h are overall similar despite the differences in sample size and are centered near zero. This study will focus on forecasts extending through 48 hours for the remainder of the study because 3–5 day forecasts have a significantly lower sample size.

Figure 2.3 shows the distribution of official intensity forecast errors. The total distributions of all errors are approximately Gaussian with mean errors near zero in both basins for all forecast periods. The distributions for RI and RW confirm that these events represent the tails of the forecast error distributions in addition to the tails of the intensity change distribution (Kaplan and DeMaria 2003). The RI and RW distributions are also approximately Gaussian, but Atlantic and East Pacific RW events at longer lead times show a broader, almost bimodal distribution. The distributions widen with increasing forecast time period for both the total, RI, and RW events as previously noted. More RI and RW events occur in the East Pacific compared to the Atlantic and are accompanied by a slightly wider distribution of errors. The spatial distribution of 24-h RI and RW errors in Fig. 2.4 helps to explain the differences in number of RI and RW events. The higher number of East Pacific RI compared to Atlantic RI can be attributed to generally more favorable thermodynamic environments at lower latitudes in the East Pacific (Kaplan et al. 2010). The higher number of East Pacific RW events can be attributed to the sharp gradient in SST and lower instability to the northwest of the main East Pacific development

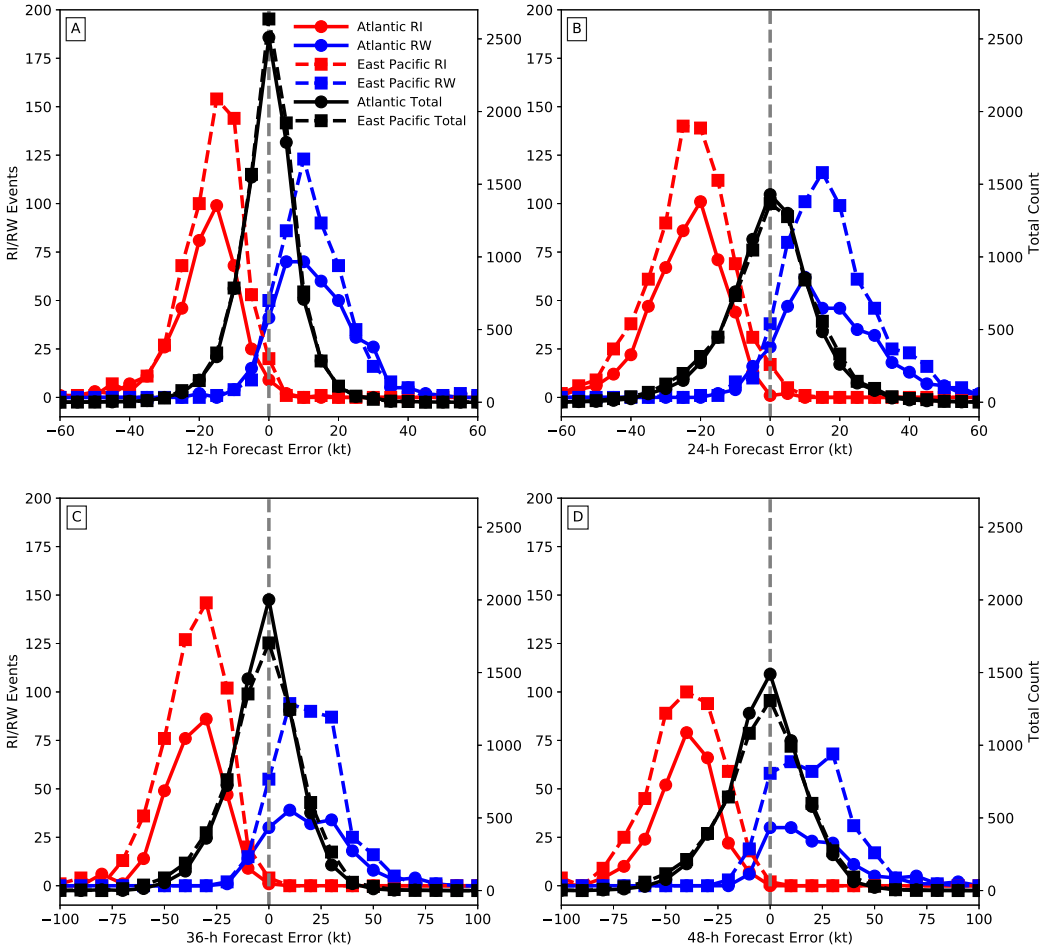

FIG. 2.3. The distribution of official intensity forecast errors for all events (black), RI events (red), and RW events (blue) for the Atlantic (circles) and East Pacific (squares). Forecast errors are shown for forecast lengths of 12 h (a), 24 h (b), 36 h (c), and 48 h (d). The 12-h and 24-h forecast errors are binned at 5 kt intervals while the 36-h and 48-h forecast errors are binned at 10 kt intervals. Note the change in ordinate scale for the 36-h and 48-h forecast errors. The number of RI and RW events use the left ordinate and the number of all events uses the right ordinate.

region (Wood and Ritchie 2015), in addition to the lower number of recurvatures and extratropical transitions (Jones et al. 2003).

The RI errors are almost always negative indicating that RI is associated almost exclusively with under-forecasted intensity change, consistent with Na et al. (2018). These distributions indicate that when RI occurred, the forecasts predicted slower intensification than what occurred on average. The RI distributions are also dependent on the forecast period, with the most frequent errors becoming more negative for longer forecast lead time. The most frequent RI errors are approximately -15, -20, -30, and -40 kt for the 12-h, 24-h, 36-h, and 48-h periods respectively.

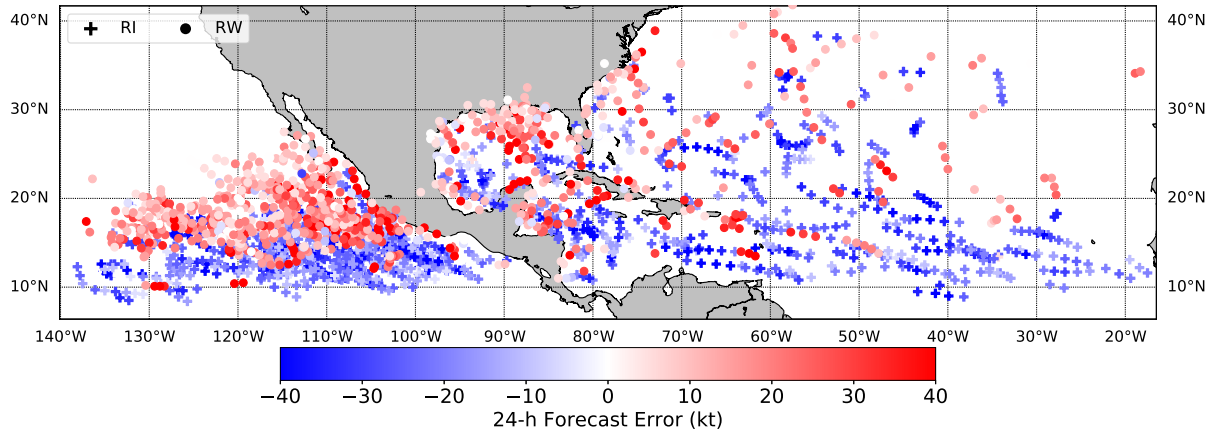

FIG. 2.4. Spatial distribution of all 24-h RW (circle) and 24-h RI (plus) events between 1989-2018 in the Atlantic and East Pacific. The events are shown at the initialization location and are colored by the intensity forecast error.

In contrast to RI, the RW events typically have positive forecast errors indicating a general under-prediction of the weakening rate. There is, however, a non-negligible component of negative forecast errors where the weakening was over-predicted. The RW distributions are wider than the RI distributions, and at longer forecast periods becomes slightly bimodal. The broadening and bimodality in the Atlantic can be attributed in part to differences between over-ocean RW and over-land RW for the 24–48-h forecast periods. For 24-h RW cases in the Atlantic, the center of the error distribution when the DTL <50 km is at 10 kt; however the center of the distribution when the DTL >50 km is at 20 kt suggesting that over-ocean weakening is harder to forecast (not shown). The spatial distribution of RW errors in Fig. 2.4 also shows that reduced errors with 24-h RW occur for hurricanes in the Gulf of Mexico approaching landfall. The rather large forecast errors associated with RW in the central Gulf of Mexico shown in Fig. 2.4 could be related to the initial storm intensity as it approaches landfall shown by Rappaport et al. (2010). The broad distribution in the 48-h RW forecasts for the East Pacific cannot be entirely explained by land interactions but could be related to track errors which become increasingly important at longer forecasts periods.

Table 2.1 shows how RI and RW events contribute to overall forecast errors. All RI and RW events are removed from the distributions and the MAE is recalculated to show the full impact of these forecasts. The average MAE for RI and RW events at all forecast times is larger in the Atlantic than the East Pacific, but the total MAE of all forecasts is lower in the Atlantic than the East Pacific for all forecast periods excluding the 12-h period. MAEs would be reduced by 10–22% if RI and RW events are neglected from the error calculations. The MAE in the Atlantic is reduced less than that of the East Pacific. The intensity

TABLE 2.2. Error statistics for when NHC forecasted intensity changes that meets the RI criteria thresholds at each forecast period. The MAE for only RI forecasted events with the sample size in parenthesis is shown for each basin. Verifying RI is the percentage of forecasted RI events that verified to the number of total RI forecasts by NHC. The probability of detection for RI events is shown as the number of verifying RI forecasts divided by the total number of RI events.

1989-2018	North Atlantic				East Pacific			
Forecast Period	12 h	24 h	36 h	48 h	12 h	24 h	36 h	48 h
Total RI Events	381	481	289	265	591	753	529	446
Forecasted RI Events	47	30	2	3	92	120	44	37
Verified RI Events	19	16	2	2	52	81	29	24
Successful RI Forecasts (%)	40	53	100	67	57	68	66	65
Probability of RI Detection (%)	5.0	3.3	0.7	0.8	8.8	10.8	5.5	5.3
Forecasted RI MAE (kt)	10.5	12.5	12.5	5.0	10.3	14.4	20.2	17.4

errors of both basins are reduced to nearly the same value at 24-h lead times when RI and RW are neglected. By removing RI and RW events, there is a reduction in MAE of 15.6%, 15.9%, 10.9%, and 9.7 % in the Atlantic and a reduction in MAE of 19.8%, 22%, 16.9%, and 15.3% in the East Pacific for the 12-h, 24-h, 36-h, and 48-h forecast periods respectively. The analysis suggests that the larger number of occurrence of RI and RW events in the East Pacific is a major contributor to why the basin has larger errors on average and would therefore have more improvement if they are neglected from the MAE calculations. It is noted that if root-mean squared error (RMSE) is used as the performance metric instead of MAE, the error reduction due to excluding RI/RW would increase due to the enhanced weight of more common large errors. Even larger improvements in overall performance would be possible at the 36-h and 48-h lead times with improved RI/RW forecasts using the RMSE metric (not shown).

Although it has been shown that there are large forecast errors for RI and RW overall, the errors when rapid intensity changes are actually forecast by NHC have not yet been considered. Table 2.2 shows the number of RI events, the number of forecasted RI events, the number of verifying RI forecasts, the verifying percentage or success ratio, the probability of detection, and the corresponding MAE for all RI forecasts. A forecast must meet or exceed the intensity change threshold magnitudes described in Section 4.2 to be considered. Therefore, a 25 kt intensity change forecast over 24-h is considered a missed RI forecast. In the Atlantic, RI is forecasted considerably less often compared to the East Pacific at all forecast periods which is related to the climatologically larger number of RI events in the East Pacific. The number of verifying forecasts are also higher in the East Pacific at the 12-h and 24-h forecast periods. It is difficult to compare RI between the two basins at the 36-h and 48-h thresholds

TABLE 2.3. Same as Table 2.2 but for rapid weakening events.

1989-2018	North Atlantic				East Pacific			
Forecast Period	12 h	24 h	36 h	48 h	12 h	24 h	36 h	48 h
Total RW Events	382	366	184	139	499	638	391	325
Forecasted RW Events	212	160	96	62	207	241	132	138
Verified RW Events	158	142	84	58	132	182	110	108
Successful RW Forecasts (%)	75	89	88	94	64	76	83	78
Probability of RW Detection (%)	41	39	46	42	26	29	28	33
Forecasted RW MAE (kt)	10.0	10.9	12.7	10.16	8.3	9.9	10.9	10.4

because only 2 and 3 forecasts meet that criteria in the Atlantic, respectively. When NHC made an RI forecast, they correctly forecasted the occurrence of 24-h RI events 53% of the time in the Atlantic and 68% of the time in the East Pacific with MAEs of 12.5 kt and 14.4 kt. The errors when RI is forecast are significantly lower than the average errors with RI/RW shown in Table 2.1, but still larger than the mean error for the forecast period. The probability of detection for RI cases is low for all forecast periods in both basins with 5%, 3.3%, 0.7%, and 0.7 % in the Atlantic and a probability of detection of 8.8%, 10.8%, 5.5%, and 5.3% in the East Pacific for the 12-h, 24-h, 36-h, and 48-h forecast periods respectively. The probability of detection is 7.5% larger for the 24-h RI in the East Pacific compared to the Atlantic which suggests that forecasters are more likely to forecast RI in the East Pacific because climatologically there are more frequent RI events there. A higher probability of detection for RI in the East Pacific could also be due to better performance by SHIPS-RII because of the more favorable environments there on average (Kaplan et al. 2010). Although this study did not find any trends using the 30 kt in 24 h RI threshold, Cangialosi et al. (2020) showed that using the 20 kt in 24-h RI threshold did suggest improvements in the probability of detection of Atlantic RI events in the last decade.

Next Table 2.3 is analyzed which shows the same elements as Table 2.2 but for RW events in both basins. Table 2.3 shows that RW events occur less often compared to RI events at all forecast periods except for 12-h forecasts in the Atlantic, which is also evident in Fig. 2.3. Despite the lower number of RW events, the number of forecasted RW events is much larger than RI events because RW is common for landfalling hurricanes. RW forecasts in the Atlantic verify 75% of the time for 12-h forecasts and 89% of the time for 24-h forecasts, which is 11% and 13% larger than the same RW forecast periods in the East Pacific. A smaller number of RW forecasts verify in the East Pacific compared to the Atlantic and there is also a lower probability of detection at all forecast periods. The differences in probability of detection of RW events between the basins can largely be explained by the larger number of over-ocean

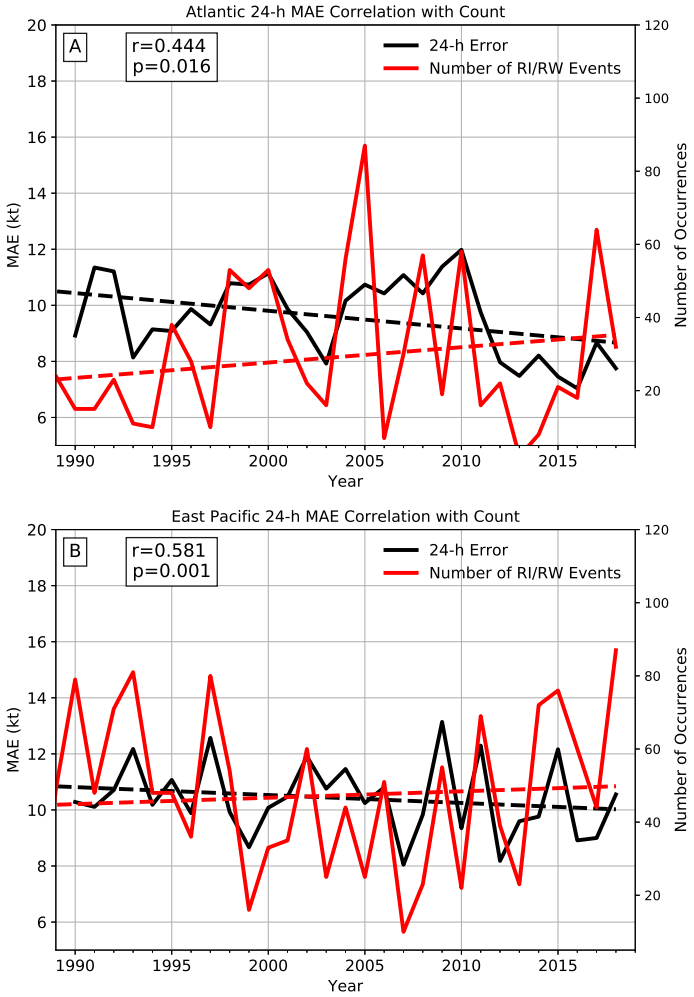

FIG. 2.5. The 24-h MAE and number of RI and RW events for the Atlantic (a) and East Pacific (b). The yearly averaged 24-h MAE (black) uses the left ordinate and the number of yearly RI and RW events (red) uses the right ordinate. Linear trend lines are shown in dashed lines and the r-value and p-value are shown testing the correlation.

weakening in the East Pacific and the larger number of landfall RW events in the Atlantic. The probability of detection and verifying forecast percentage would suggest that RW in the Atlantic is better forecasted; however, the MAE for RW events in the Atlantic are actually higher for 12–36-h forecast periods despite the fact that landfalling hurricanes are more common and typically are better forecasted. It is speculated that the larger MAE in the Atlantic RW events could be due to uncertainty in the track forecasts and the timing of landfall.

While RI and RW events substantially increase the average MAE, there is considerable year-to-year variability in the number of these events. To address this variability, the correlation between number of RI and RW events and the yearly mean forecast errors are considered. Figure 2.5 shows the Pearson

FIG. 2.6. The yearly intensity forecast bias for only RI and RW events in the Atlantic and the East Pacific. Bias associated with RI and RW are shown for the 12-h (a), 24-h (b), 36-h (c), and 48-h (d) forecast periods using the definitions stated in Section 4.2. Lines with stars indicate that the slope of the bias line is statistically significant from zero at the 90% confidence level using a two-sided T-test. The gray lines indicate the zero bias line.

correlation between number of 24-h RI and RW events and the yearly MAE. The correlation explains ~20% of the variance in the Atlantic and ~30% of the variance in the East Pacific which is statistically significant at the 95% confidence level. The positive correlation indicates that the more tropical storms and hurricanes undergo RI or RW, the larger the MAE for a given year. While attribution of the trends and year-to-year variability is beyond the scope of this study, it is emphasized here that it is important to consider these trends and variability when looking at the progressive improvement of forecast errors. As the forecast period length increases, the correlation is reduced in the Atlantic due to decreasing sample size, while there is little change in the correlation with forecast period length in the East Pacific (not shown).

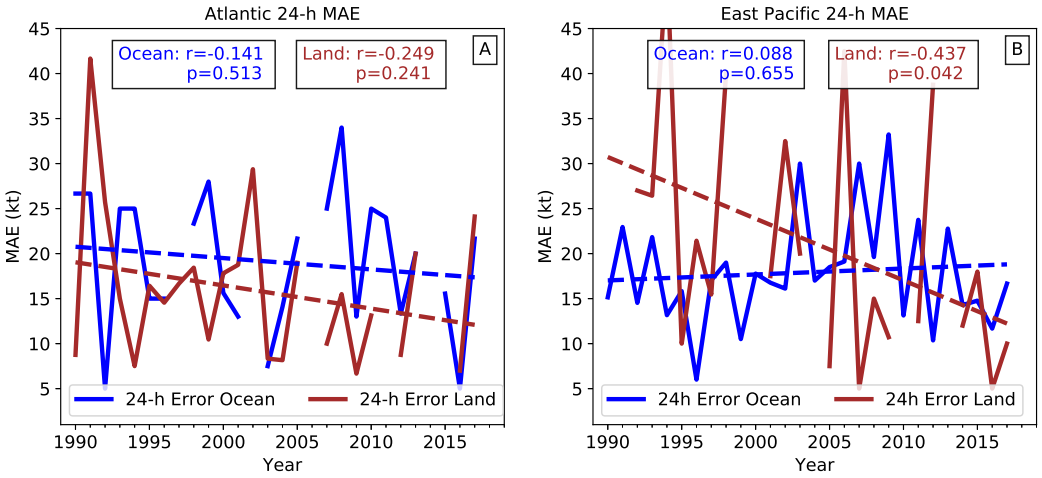

FIG. 2.7. Yearly 24-h MAE for the Atlantic (a) and East Pacific (b) associated with only RW cases with land interactions (brown) and over-ocean RW (blue) events. Data is shown from 1989-2017 where there is overlap between the verification database and SHIPS database. The r-value and p-value are shown for each trend line which is shown in the dashed lines. The p-value is determined from a two-sided T-test testing the NULL hypothesis that the slopes of the lines are zero.

The RI and RW forecasts are analyzed next to determine whether or not forecasts associated with RI and RW have improved over the years. To analyze whether the errors have improved the yearly forecast bias, which is the mean of the error distribution, is calculated for forecasts where RI and RW occurred. Figure 2.6 shows the bias of RI and RW events over time with statistically significant slopes at the 90% confidence level shown with stars. At the 12-h forecast period there is statistically significant improvement in RI forecasts in both basins, although 12-h RW forecasts have shown little improvement. For 24-h RI events, the East Pacific has shown statistically significant improvement but RI in the Atlantic has not improved. The improvement of 24-h RI forecasts in the East Pacific can be partially attributed to improved guidance from SHIPS-RII which has been shown provide better RI probabilities in the East Pacific (Kaplan et al. 2010). 24-h RW cases in the Atlantic have shown statistically significant improvement, but the East Pacific 24-h RW events have not shown improvement. There is clear improvement in 36-h and 48-h RI and RW forecast bias in both basins although not all the improvement is significant. The biases for 36-h RI, 48-h RI, and 48-h RW events have all improved in the East Pacific. The large year-to-year variability in RI and RW events in the Atlantic is a contributing reason to the lack of statistically significant improvement in the 36–48-h RI and RW bias and should be considered when referencing the yearly biases. The improvements in some of the biases suggest that forecasts of rapid intensity changes are improving, although it is not because of an increase in forecasts of RI and

RW. There are no significant trends in the number of yearly RI and RW forecasts in either basin (not shown).

RW in East Pacific hurricanes is more common than in the Atlantic but it is unclear why 24-h RW forecasts in the East Pacific have shown no improvement while significant improvements are found in the Atlantic. One potential reason for the difference in 24-h RW trends between the basins is the contribution of RW errors by landfall events. In order to quantify how landfall events affect the trends in forecast errors associated with RW, the events where RW occurred within 50 km of any land mass are isolated. Figure 2.7 shows the 24-h MAE trends for over-ocean and land interaction RW events separately for the Atlantic and East Pacific. In the Atlantic, the errors associated with over-ocean RW are larger and have not improved as much compared to the errors associated with RW due to land interactions. Both types of Atlantic RW have improved slightly through the decades which both contribute to the significant improvement in 24-h RI bias shown in Fig. 2.6. In the East Pacific, the trend for RW events where land interactions are involved is negative at a statistically significant level. RW due to land interaction cases are not as common in the East Pacific but the MAE associated with those events have been reduced in recent years. The over-ocean RW events in the East Pacific are the main contributor to the lack of improvement in the biases shown in Fig. 2.6. The MAE associated with over-ocean RW events have not improved with time and the trend line is slightly positive. It is speculated that a contributing factor may be the difficulty in forecasting the timing of over-ocean RW events as hurricanes cross SST gradients in the East Pacific versus the timing of landfall events in the Atlantic. Improvements in RW forecasts near land can partially be explained by improving track forecasts, although it is unclear why improved track forecasts do not directly result in lower intensity errors for over-ocean RW in the East Pacific. Cangialosi et al. (2020) noted that track and intensity errors have only a correlation of 0.2 from 2010-2019 in the Atlantic. One potential reason for the lack of improved over-ocean RW forecasts is that even small cross-track errors can result in large SST differences under East Pacific hurricanes along the climatological SST gradients.

Figure 2.8 shows the relationship of official intensity forecast errors for the different forecast periods with maximum wind speeds at the forecast initialization time. In general, the distributions are similar between the East Pacific and Atlantic with the largest concentration of forecasts for tropical cyclones between 30–70 kt. For the 12-h forecasts, the distributions are centered near zero. As the forecast period length grows the distributions widen with larger magnitudes of intensity forecast errors. The distributions grow asymmetrically for increasing forecast period length with more overestimates

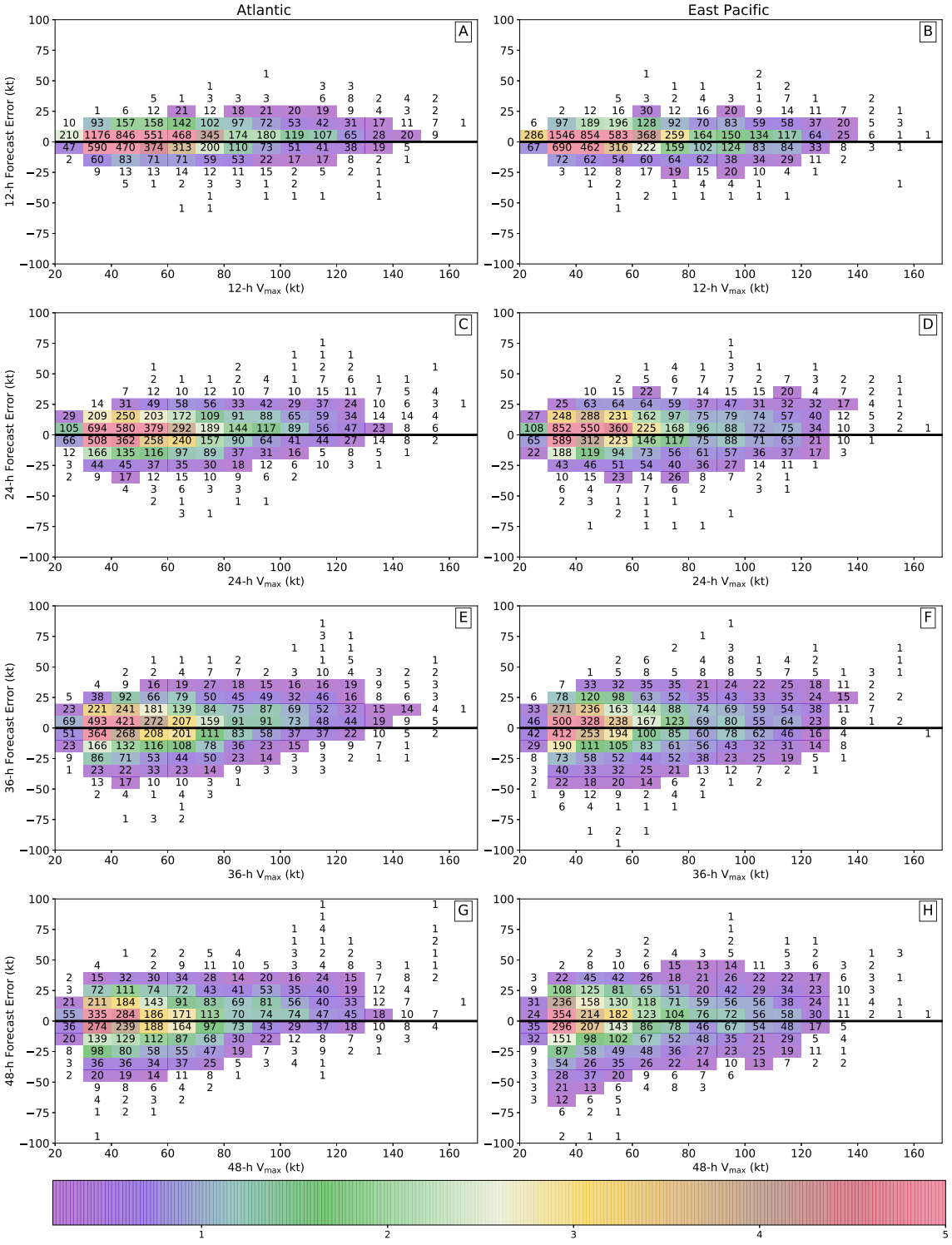

FIG. 2.8. Distribution of forecast errors with maximum wind speeds for the Atlantic (a, c, e, g) and East Pacific (b, d, f, h). Shown are the distributions for 12-h (a, b), 24-h (c, d), 36-h (e, f), and 48-h (g, h) forecast periods. Both the intensity forecast errors and maximum wind speeds are binned at 10 kt intervals. The colored boxes are normalized by the total number of events. Bins that make up <.2% of the total are not shaded. The black line is the zero forecast error line where values above the line are the number of zero error forecasts.

(positive bias) in intensity for stronger hurricanes and more underestimates (negative bias) for weaker hurricanes. Bhatia and Nolan (2013) also found a dependence of forecast errors on initial hurricane intensity with larger intensity biases for stronger storms. There is a larger tendency for overestimates in the Atlantic compared to the East Pacific in the 24-48-h forecast periods which likely is due to more land interactions. The overestimates at larger hurricane intensities may also be due to the difficulty of predicting secondary eyewall formation and eyewall replacement cycles. Kossin and DeMaria (2016) found similar overestimates in SHIPS due to eyewall replacement cycles and created a simple model to reduce the errors. More frequent large underestimates in the East Pacific can be attributed to the larger number of RI events in the basin.

2.4 Environmental Contribution to Forecast Errors

In this section the environmental variables are analyzed that may contribute to the difficulty in forecasting RI and RW. For conciseness, only select environmental variables from SHIPS are shown for the 24-h forecast period. The environmental variables shown correspond to the average atmospheric state between the time when each forecast was made and the verifying time. While the change in environmental variables over the forecast time is also important for intensity change, it adds another layer of complexity that is not considered here but will remain a topic of future work.

Figure 2.9 shows the total error distribution in addition to the distribution for exclusively RI and RW events of forecast errors in the Atlantic with respect to 850–200 hPa vertical wind shear, SST, and 850–700 hPa RH. Other variables such as 200 hPa divergence, 850 hPa vorticity, and maximum potential intensity were also considered but showed similar relationships and are not shown for brevity. The errors for all events with respect to vertical wind shear (Fig. 2.9b) indicate that the magnitude of forecast errors are generally reduced for environments with strong vertical wind shear. For environments with low vertical wind shear, the forecast error distribution widens considerably with both large positive and large negative forecast errors. If only the vertical wind shear of RI and RW events is considered (Fig. 2.9a), it is evident that RW (positive errors >10 kt) events generally occur in environments with slightly larger shear values and that RI (negative errors <-10 kt) events occur in environments with slightly lower shear consistent with past observations (e.g., Kaplan and DeMaria 2003; Hendricks et al. 2010). The widest distribution of forecast errors for both RI and RW occur when shear is low to moderate (5–20 kt) which is climatologically favorable for hurricane intensification.

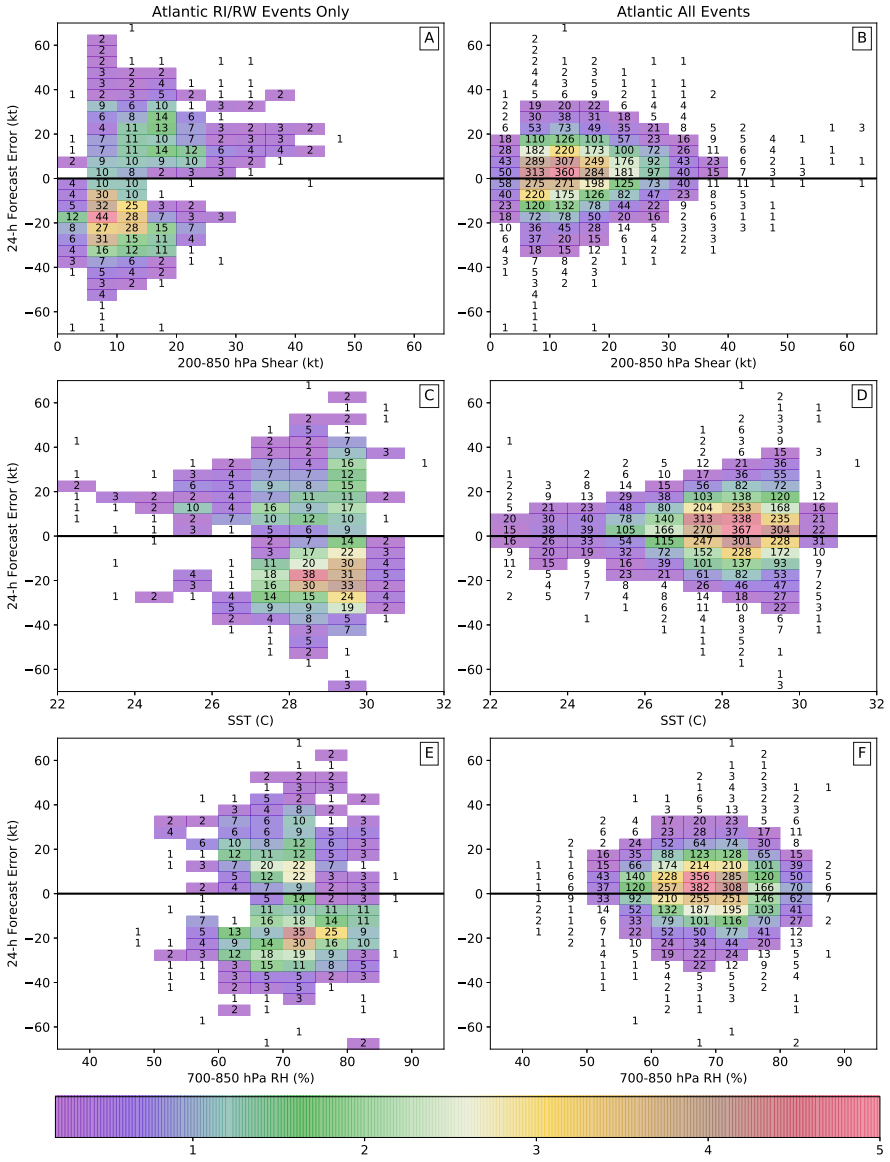

FIG. 2.9. The relationship between 24-h official forecast errors and SHIPS environmental data in the Atlantic from 1989-2017. The total distribution for all events is shown on the right (b, d, f) and the distribution for only RI and RW events is shown on the left (a, c, e) The 850-200 hPa vertical wind shear (a, b), SST (c, d), and 850-700 hPa RH (e, f) are binned at 5 kt, 1 C, and 5% respectively. Intensity forecast errors are binned at 5 kt. The colored boxes are normalized by the total number of events. Bins that make up <.2% of the total are not shaded. The black line is the zero forecast error line where values above the line are the number of zero error forecasts.

The errors with respect to SST show a similar pattern as the vertical wind shear (Figs. 2.9c,d) with more unfavorable conditions (colder SST) resulting in a narrower distribution of intensity forecast errors. As SST increases, the distribution of forecast errors widens and there is an increase in the magnitude of both positive and negative errors. The relationship between SST and forecast errors for RI and

RW events shows a similar distribution as the total but with larger error magnitudes. The total distribution of all intensity forecast errors with 850-700 hPa RH (Figs. 2.9e,f) shows a circular distribution centered at zero errors and 65-70% RH. The error distribution is wider for larger RH values compared to lower RH values. The distribution of forecast errors associated with RI are shifted slightly towards larger RH values compared to RW. Errors associated with RW occur in environments similar to RI with the largest error magnitudes for higher RH. The largest intensity forecast errors occur at low shear values with warm SST suggesting that additional factors and processes need to be considered to forecast RI and RW, such as inner-core dynamics (Van Sang et al. 2008; Aberson et al. 2015; Nystrom and Zhang 2019).

Figure 2.10 shows the relationship of environmental conditions with 24-h official intensity forecast errors in the East Pacific. Here the error distributions associated with 850–200 hPa vertical wind shear, SST, and 850–700 hPa RH are shown. The overall qualitative distribution of environmental conditions in the East Pacific is similar to the Atlantic, but the forecast error distributions are not as symmetric about the zero forecast error line for SST and RH. Figure 2.10c, e shows there are very few large forecast errors for RW over cold SST or drier environments suggesting that when the environment is unfavorable, RW is easier to forecast. As the environment becomes more favorable with reduced vertical wind shear, warmer SST, and higher RH, the width of the distribution of forecast errors increases, which is similar to the Atlantic. Also similar to the Atlantic, the widest forecast error distributions associated with RI and RW typically occur in environments with low shear, warm SST, and moderate RH. This again emphasizes that the inner-core processes are critical for predicting rapid changes in intensity.

To better illustrate the role of the environment on total forecast errors, Fig. 2.11 shows the normalized distribution of all 24-h forecast errors in different environments in the East Pacific from SHIPS. In Figure 2.11a the distributions correspond to vertical wind shear greater than 20 kt, between 10 and 20 kt, and less than 10 kt indicating an unfavorable, moderate, and favorable environment for hurricane intensification respectively. The peak of each distribution is normalized so the key differences in the figures are in the widths and skewness of the distributions. The analysis provides further evidence that intensification is underestimated more frequently when there is favorable environmental shear. When vertical wind shear exceeds 20 kt, there are fewer underestimates of hurricane intensity because RI does not frequently occur and slower intensification rates are therefore forecast well. On the positive side of the forecast error distribution, the largest overestimates of hurricane intensity occur with

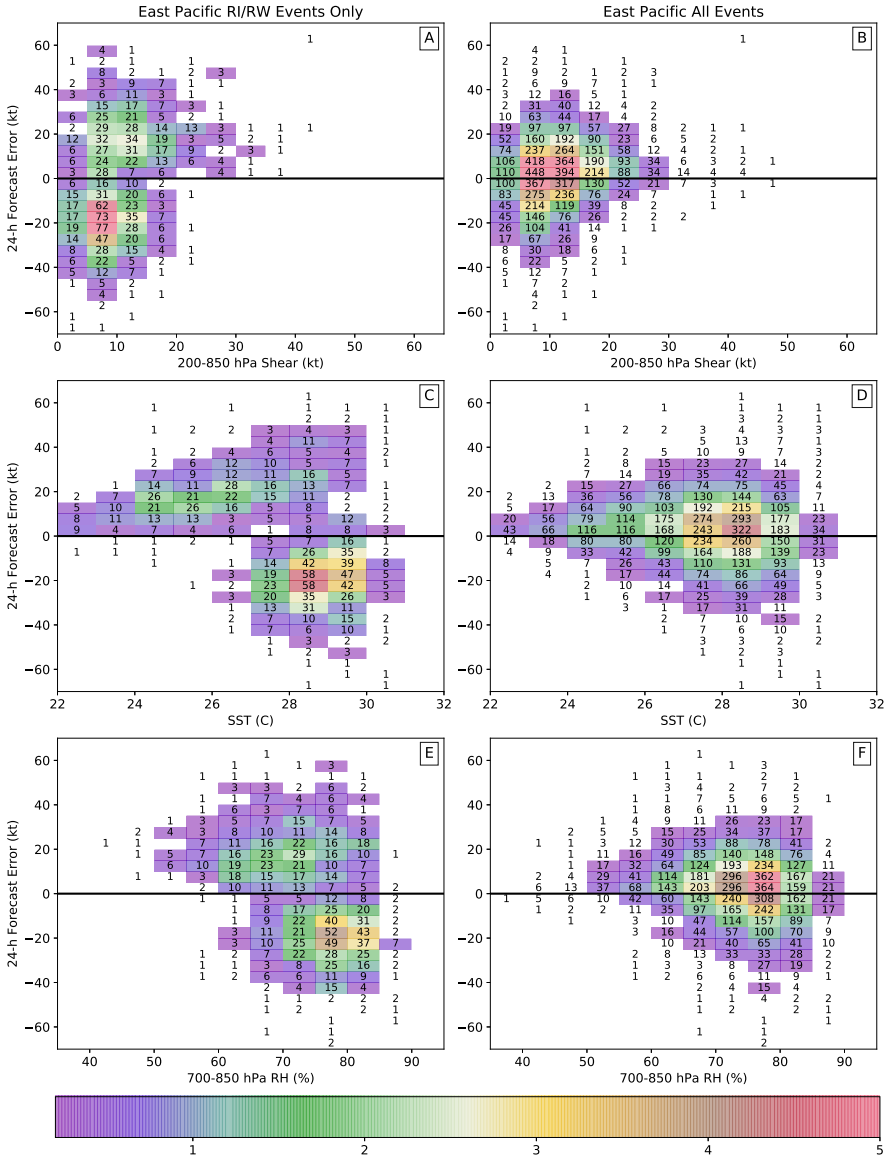

FIG. 2.10. Same as Fig. 2.9 but for the East Pacific.

moderate values of vertical wind shear. This suggests that larger errors associated with RW are in environments with moderate wind shear consistent with other observations (Bhatia and Nolan 2013). The distribution of forecast errors for RH (Fig. 2.11b) and SST (Fig. 2.11c) show similar relationships as vertical wind shear indicating that larger negative forecast errors are associated with more favorable environments. Also similar to vertical wind shear, marginal values of SST and RH seem to have the largest positive forecast errors.

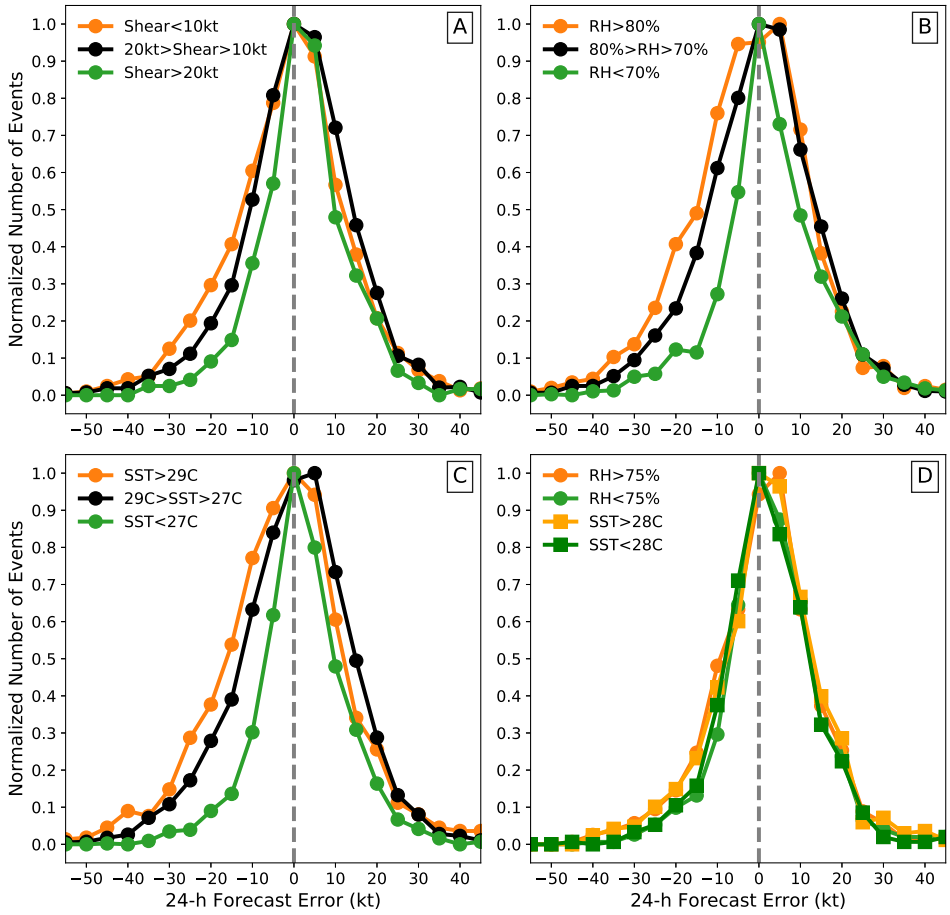

FIG. 2.11. The distribution of 24-h forecast errors in the East Pacific conditioned on the SHIPS 850–200 hPa vertical wind shear (a), 850–700 hPa RH (b), and SST (c). For (a), (b), and (c) the SHIPS environmental variable is conditioned into three groups with the forecast error distribution then normalized by the maximum value. (d) shows the distribution of forecast errors for RH>75% (orange) and RH<75% (green) marked with circles and the SST>28 C (orange) and SST<28 C (green) marked with the squares when the 850–200 hPa vertical wind shear is larger than 15 kt. Forecasts errors are limited to those that occurred greater than 50 km from any major landmass.

For any individual forecast one must consider the vertical wind shear, RH, and SST but sometimes one environmental variable can limit possible ranges of intensity change. Thus far all the environmental variables have been considered independently when analyzing the forecast error distributions; however, all the environmental variables co-vary and play a role in hurricane intensity change. Figure 2.11d shows the distributions of favorable and unfavorable values of RH and SST given that the vertical wind shear is greater than 15 kt. When vertical wind shear is moderate, the distribution of forecast errors still show that warmer SST and higher RH are associated with larger numbers of negative forecast errors, but the differences between favorable and unfavorable SST/RH have been diminished. When SST is warm and RH are high, there is also a shift towards a positive bias in the distribution compared

to a bias centered on zero when all the factors are unfavorable for intensification. The MAE is 12.6 kt in the case where all the variables are favorable (meaning vertical wind shear is less than 15 kt, RH>75%, and SST>28 C), but when the environment is unfavorable by these same thresholds, the MAE is reduced considerably to 7.8 kt. Further research is needed to understand the various combinations of environmental parameters on forecast skill.

2.5 Summary and Conclusions

In this study, the characteristics of intensity forecast error distributions have been evaluated to demonstrates the relative contributions of both rapid intensification (RI) and rapid weakening (RW) events. It has been shown that rapid intensity changes are associated with the tails of the distribution of intensity forecast errors, which has been assumed but never analyzed in detail to the authors' knowledge. Forecast errors associated with both rapid intensification and weakening are nearly always underestimated in magnitude consistent with the analysis by Na et al. (2018). Consistent with DeMaria et al. (2014), there has been a slight improvement in the 24-h intensity forecast error distributions over the years and intensity forecast distributions overall are centered at zero.

RI and RW is associated with large forecast errors on average. Rapid weakening is forecasted more often than RI with a much higher success ratio and probability of detection. Over-ocean RW events cause the reduced probability of detection in the East Pacific compared to the Atlantic despite the larger number of RW events. Rapid intensification occurs more often in the East Pacific compared to the Atlantic which may lead forecasters to predict intensity changes meeting the RI thresholds more often in the East Pacific. The probability of detection for 24-h RI events is 7.5% larger in the East Pacific, although RI is predicted only ∼3% of the time in the Atlantic. Although NHC rarely forecasts RI, when NHC does predict rapid intensification at 24 h, the forecasts verify ∼50% of the time in the Atlantic. Using a probability of detection approach to evaluating RI and RW forecasts has some limitations because a 25 kt intensity change forecast in 24-h would be considered a missed RI forecast despite the fact that the error would be low. However, using only mean absolute error as a metric is also limited by the fact that accurately forecasting RI thresholds produces minimal error improvement.

This study is novel in its examination of intensity forecast error distributions in association with environmental conditions over multiple decades. It has been shown that the largest error distributions associated with RI occur in climatologically favorable environments for intensification. Although RW

has received less attention in the literature, RW events cause a larger distribution of intensity forecast errors than RI. In the Atlantic, the wide distribution is attributed to the difference in over-ocean events and landfalling hurricanes. Over-ocean RW causes larger forecast errors on average because substantial weakening is usually predicted for landfalling hurricanes unless there are substantial track errors associated with the landfall timing. Rapid weakening events that occur in more unfavorable environments, such as with cold SST or stronger vertical wind shear, have lower forecast errors on average suggesting a lower degree of intensity forecast uncertainty. RW events can occur in moderate to favorable thermodynamic and dynamic environments for intensification, suggesting that improved understanding of inner core processes is required for both RW and RI events.

As the forecast period length increases from 12 to 48 hours, the width of the intensity error distributions also increases as both positive and negative errors grow with time. The intensity forecast error distributions show similar widths beyond 48 h. The larger forecast errors for RI and RW events explains roughly 20% of the variance in the yearly mean absolute errors in the Atlantic and 30% of the variance in the East Pacific. A positive correlation between the number of RI and RW events and the yearly mean forecast error has been assumed in previous discussions of forecast errors (Cangialosi and Franklin 2014) and here it has been explicitly shown to be true. In the East Pacific, the intensity bias associated with RI has decreased at a statistically significant level for the 12-h, 24-h, 36-h, and 48-h forecast periods, while significant improvement is found only in 12-h RI forecasts in the Atlantic. Intensity biases associated with RW have decreased at a statistically significant level for the 24-h period in the Atlantic and in the 36-h and 48-h period in the East Pacific. The lack of improvement in East Pacific 24-h RW forecasts can be attributed to large forecast errors for over-ocean RW events.

Understanding the environment is important in determining the potential for a tropical disturbance to intensify, but it is shown here that the largest forecast errors occur due to RI when there is a favorable environment. The largest RW errors also occur in moderate to favorable environments. The effects of convective and mesoscale processes are attributed to the increased spread of short-term intensity forecast errors when the large-scale environment is favorable for intensification. This suggests that when hurricanes are in favorable environments for intensification the intensity forecasts have a higher probability of large errors and thus a larger degree of uncertainty. The analysis presented in this study suggests that improved understanding of the inner-core dynamics of hurricanes in favorable environments is paramount and an important area for future work to improve intensity forecasts and reduce the width of the intensity error distribution.

When RI occurred, the distribution of errors suggests that forecasts were in general too slow to intensify and nearly always underestimated the intensification. These errors in prediction of RI are evaluated without considering forecast-to-forecast continuity or changes in numerical model guidance over time. Although each forecast is treated as being independent in this study, real-time forecasts are correlated from one forecast cycle to the next. The relative contribution to intensity forecast errors from individual factors such as forecast continuity or numerical model guidance remain a topic for future work. The uncertainty of hurricane rapid intensity change forecasts will be dependent on a combination of the uncertainty in track forecasts (particularly near land or gradients in thermodynamic variables), the thermodynamic environment, and the consistency of model guidance to give forecasters the confidence to forecast RI and RW thresholds. New tools for RI and RW prediction are needed at NHC in order to improve intensity forecasts (Cangialosi et al. 2020).

CHAPTER 3

THE SENSITIVITY OF EYEWALL REPLACEMENT CYCLES TO SHORTWAVE RADIATION [1]

3.1 INTRODUCTION

It is now understood that eyewall replacement cycles (ERCs) are a common phenomenon in mature tropical cyclones (TCs). During an ERC, a secondary eyewall will form at a distant radius from the existing primary eyewall of the incipient TC. The strength of tangential winds near the primary eyewall typically decay while tangential winds near the secondary eyewall intensify. The weakening of the primary eyewall reduces the maximum intensity of the TC, while the strengthening secondary eyewall expands the wind field and increases the overall integrated kinetic energy of the system (Sitkowski et al. 2011). Changes in the wind field caused by ERCs are critical to forecast because a broader wind field means that damage could extend over a larger area. The prediction of ERCs remain a challenge for operational forecasters because they are driven by vortex-scale processes that are internally regulated and often short lived (Kossin and DeMaria 2016). Kossin and DeMaria (2016) showed that ERCs introduce substantial intensity forecast errors in the Statistical Hurricane Intensity Prediction Scheme (SHIPS), which is one of the primary intensity guidance models used by the National Oceanic and Atmospheric Administration/National Hurricane Center (NOAA/NHC) (DeMaria et al. 2005). In order to improve intensity forecasts, numerical weather prediction models need to accurately capture the onset and duration of ERCs.

The resolution and physics of numerical weather prediction models are continually improving and many hurricane forecast models are now able to explicitly simulate ERCs. It is unclear; however, how accurate ERC forecasts are and how sensitive ERCs may be to individual radiation or microphysics schemes. Recent work by Tang et al. (2017) showed that the secondary eyewall formation (SEF) in Hurricane Edouard (2014) did not occur when shortwave radiation was removed from the simulation. It was shown that shortwave radiation acts to stabilize the mid-upper troposphere in order to suppress convective development in the moat region over the 48 hours prior to the SEF. Tang et al. (2017), however, only tested the sensitivity of a single SEF to shortwave radiation as a complete ERC did not take place. The sensitivity of ERCs to shortwave radiation has not yet been addressed in the literature which is the goal of the present study. The current study aims to evaluate the sensitivity of ERCs to radiation

[1] The contents of this chapter have been submitted to be published in the Journal of Geophysical Research: Atmospheres by the American Geophysical Union (AGU).

in an idealized framework in order to diagnose the impacts of diurnal radiation on ERC timing and TC intensity.

It is well known that shortwave radiation plays an important role in the diurnal cycle of convective clouds, but how this role impacts TC genesis or intensity is often case dependent. During tropical cyclogenesis, radiation can influence individual cloud clusters and convective cells because a cirrus canopy has not yet developed. Without upper-level clouds the thermodynamic environment can efficiently cool due to longwave radiation which has been shown to increase the relative humidity (RH) and increase rates of subsequent tropical cyclogenesis (Sundqvist 1970; Craig 1996; Melhauser and Zhang 2014; Tang and Zhang 2016; Bell and Montgomery 2019). Other studies have suggested the differential radiative heating between cloudy and cloud-free regions due to radiation could promote stronger low-level convergence into the cloudy region (Gray and Jacobson 1977; Nicholls 2015). Once the cirrus canopy expands over a large area and the TC intensifies, the time scale for strong eyewall convection to be influenced by large-scale destabilization or horizontal differential radiative heating between cloudy and cloud-free regions increases. Bu et al. (2014) found that weak but continuous longwave warming in the cirrus canopy was responsible for strengthening the TC outflow and inducing outer core convection that expands the tangential winds. Fovell et al. (2016) reaffirmed the results of Bu et al. (2014) using several idealized models, showing that the longwave warming within the cirrus canopy was important for expanding the tangential wind fields of TCs through promoting outer core convection and increasing RH. Direct shortwave heating in the mid-upper tropospheric clouds also acts to stabilize the layer and reduce convective precipitation (Xu and Randall 1995). Shortwave heating within the cirrus canopy near the vortex center could also generate anomalous circulations that enhance or reduce the TC secondary circulations and generate propagating inertial buoyancy waves (Dunion et al. 2014; Navarro et al. 2017; Ruppert and O'Neill 2019). Radiation is important to consider on ERCs because of its interactions across both spatial and temporal scales that can modify TC structure and intensity through multiple pathways.

Several mechanisms have been proposed on what causes SEFs and ERCs, although a clear consensus on the primary mechanism has not yet been reached. The axisymmeterization of rainband convection is required for ERCs and the preceding SEF, although recent studies have suggested that stratiform clouds may also be important for initiating SEFs (Didlake et al. 2018; Didlake and Kumjan 2018). Zhu and Zhu (2014) showed that outer rainband diabatic heating from convection induces large positive tangential wind tendencies leading to the formation of secondary wind maximums. Zhu and

Zhu (2014) further used the Eliassen model (Eliassen 1952) to demonstrate that outer rainband convection must reach a certain strength relative to the eyewall convection before it can initiate and drive a secondary wind maximum. It is suggested herein that the radiative effect on ERCs is through a modification of the rainband diabatic heating profile from the microphysics scheme.

Although Tang et al. (2017) found that the suppression of convection in the moat region is important for SEF occurrence, it is proposed that there is another mechanism controlling the timing of ERCs. It is hypothesized that on short time scales the direct shortwave radiative heating in the expansive upper-level cloudy region stabilizes the upper-troposphere and reduces convective available potential energy (CAPE) which diminishes outer core convection. The larger the magnitude of shortwave heating in the outer core, the less favorable the environment for convection, yielding less total condensational heating in the rainbands from convection, a slower expansion of tangential winds, and therefore a delayed eyewall replacement cycle.

The paper is organized as follows. In the following section, the setup of the idealized model and experimental design will be detailed with additional sensitivity tests. Section 3.3 will show the sensitivity of the ERCs to shortwave radiation while Section 3.4 will diagnose the factors controlling changes to TC intensity. Section 3.5 focuses on the effects of shortwave radiation on the bulk properties of convective and stratiform clouds. Section 3.6 will summarize and discuss the conclusions from this work.

3.2 Experiment

To investigate the influences of radiation on SEFs and ERCs, idealized experiments are conducted using the Advanced Research version of the Weather Research and Forecasting (WRF-ARW; version 3.7.1; Skamarock et al. 2008) model. In the full-physics idealized simulations performed by Trabing et al. (2019), TCs developed a secondary eyewall without any added perturbations to the model. In Trabing et al. (2019), ensembles were performed with full radiation, longwave only radiation, and no radiation with three different tropopause temperatures each. From the ensemble members that underwent an ERC, the first ensemble member is selected from the experiment with a tropopause temperature of 199.6 K to be the “Control" for this study. It is noted that when full diurnal radiation was included the intensity variability due to small perturbations in water vapor was small, so the following results are not sensitive to the specific selection of any individual ensemble member.

The experimental setup for the idealized WRF simulations can be found in Trabing et al. (2019) but will be briefly summarized here for completeness. The simulations were conducted with two-way

TABLE 3.1. Description of the experiments and abbreviated names referred to in this study.

Name	Experiment
NoSW48	Restart at the 48 hour mark with no solar radiation
0.5xSW48	Restart at the 48 hour mark with 50% decrease of the solar constant
1.5xSW48	Restart at the 48 hour mark with 50% increase of the solar constant
2xSW48	Restart at the 48 hour mark with the doubling of the solar constant
NoSW	Restart at the 96 hour mark with no solar radiation
0.5xSW	Restart at the 96 hour mark with 50% decrease of the solar constant
1.5xSW	Restart at the 96 hour mark with 50% increase of the solar constant
2xSW	Restart at the 96 hour mark with the doubling of the solar constant

nested, doubly-periodic domains with 18, 6, and 2 km resolution in the horizontal and 30 stretched vertical levels reaching 25 km in altitude. The outer domain of the simulations extends 5400 km in the horizontal and employs the New Tiedtke convective parameterization due to its relatively coarse resolution (Tiedtke 1989). Idealizations are made such that the sea surface temperature (SST) is fixed at 301 K, there is no background flow, and the Coriolis parameter is fixed ($f = 5{*}10^{-5}$ s^{-1}). The simulations were initialized with a weak vortex which is the same as that in Rotunno and Emanuel (1987) and subsequently integrated for eight days beginning at local noon on 3 July. The Thompson aerosol-aware microphysics (Thompson and Eidhammer 2014) and the Yonsei University planetary boundary layer scheme (Hong et al. 2006b) were employed.

The radiation schemes used in this experiment are the Rapid Radiative Transfer Model (RRTM) for longwave radiation (Mlawer et al. 1997) and the Dudhia shortwave radiation scheme (Dudhia 1989). The RRTM and Dudhia radiation packages are the same schemes used in Tang et al. (2017). Both schemes use the plane-parallel assumption in calculating radiative fluxes while the solar zenith angle for shortwave flux calculation is horizontally homogeneous for each time step. To test the sensitivity of ERCs to shortwave radiation, the Control simulation is restarted at two different times prior to the ERC with modifications to the radiation packages. The Control simulation is restarted at the 48 hour mark when the TC is rapidly intensifying and at the 96 hour mark when the TC is near its maximum intensity and would be considered a mature TC. Two different times are examined because the effects of radiation on TC intensity and ERCs may be subjective relative to the developmental stages of the TC and the formation of a cirrus canopy.

From the 48 h and 96 h restarts, the shortwave radiation using the Dudhia scheme is turned off, which means that a scenario has been created where it is only night, and will be referred to as “NoSW48" and “NoSW". To better understand how shortwave radiation influences the ERC, the amount of shortwave heating is varied by changing the “solar constant" in the radiation driver of WRF. The initial solar

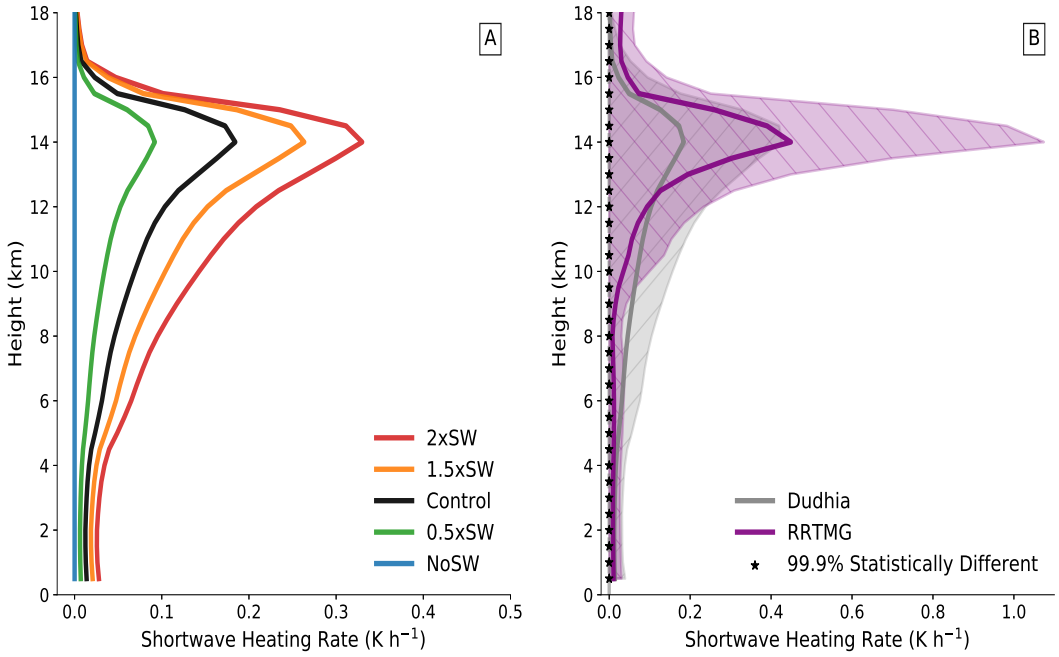

FIG. 3.1. (a) The mean shortwave radiative heating rate profiles averaged over radii greater than 150 km in the inner domain during the first 24 hours of the 96 hour restart experiments. A comparison between the Control experiment using the Dudhia scheme and a sensitivity test using the RRTMG scheme with the same initial conditions, temporal, and spatial time scales is shown in (b). The black stars indicate where the schemes are statistically different at the 99.9% confidence level using a two-sided T-test. The colored shading indicates the standard deviation of the shortwave schemes. Note that the shading of the standard deviation has been eliminated below zero since there are no shortwave cooling values.

constant from the control of 1370 W m^{-2} is halved (685 W m^{-2}), amplified by 50% (2055 W m^{-2}), and doubled (2740 W m^{-2}). These experiments will be referred to as “0.5xSW", “1.5xSW", and “2xSW" by the ratio of modification to the solar constant, respectively. All of the experiments referenced herein are listed in Table 3.1. By changing the solar constant, the experiments directly test the sensitivity of ERCs to the magnitude of shortwave heating but note that the factors changing the solar constant do not directly translate to the same exact factor of heating which will be modified by cloud feedbacks. Figure 3.1a shows average shortwave heating rates for each experiment highlighting that changes to the magnitude of the solar constant do not cause the same change in the heating rate at each altitude due to additional non-linear interactions with clouds.

Additional sensitivity tests were conducted to estimate the effects of the diurnal cycle on the ERC and to the timing of the modification relative to the diurnal cycle. The first sensitivity test is to completely remove the diurnal cycle of shortwave radiation. The diurnal cycle is removed by fixing the solar zenith angle and reducing the solar constant such that the daily integrated solar insolation is the

same as the control. By reducing the solar constant but allowing shortwave heating at all time steps, the effect is essentially a reduction in the average longwave cooling rates. The same methodology was used in Ruppert and O'Neill (2019) for examining the circulation changes in simulated TCs due to the diurnal cycle. This method is used on each of the "0.5xSW", "1.5xSW", and "2xSW" experiments to increase confidence in the simulated results and to reduce possible complications with inertia-buoyancy waves. With amplified heating rates due to a doubled solar constant, an enhanced inertial buoyancy wave response to that heating in the upper-troposphere is expected; however, this interesting feature does not impact the findings of this study. The same response of the ERC to the shortwave radiation was found when the diurnal cycle was removed and solar insolation was fixed (not shown).

A second sensitivity test was conducted by modifying the solar constant near sunset instead of solar noon. This experiment resulted in a slight modification to the timing of the ERC and a reduction in the overall differences between the simulations because there was overall less time for the radiation to modify the environment and cloud distributions. Despite these slight differences, the physical mechanisms remain the same sucg that the conclusions of the study are not sensitive to the diurnal cycle or sub-daily changes in the timing of the simulation restart time.

In the modeling framework used in this study, the sensitivity of the ERC to the microphysics or radiation scheme cannot be directly determined because changes to those schemes from a restart is not possible in WRF. The only feasible comparison is to run additional full simulations with different physics parameterizations. A comparison between the all-sky shortwave heating rates in the experiments using the Dudhia scheme with another simulation using the RRTM for General Circulation Models (RRTMG; Iacono et al. 2008) scheme is shown in Figure 3.1b. The RRTMG scheme for shortwave radiation is a more advanced scheme that accounts for surface reflection that is not incorporated into the Dudhia scheme. Although the simulation with the RRTMG scheme does not have an ERC, periods are compared in the model where the simulated TCs are of similar size and intensity. Overall, the Dudhia scheme underestimates the peak heating rates and allows more shortwave radiation to be transmitted through the clouds compared to the RRTMG scheme. By amplifying the shortwave radiation in the 2xSW experiment, the peak in-cloud heating rates are actually brought closer to RRTMG values but with an increased bias in the amount of radiation transmitted through the upper-level clouds and absorbed in the mid-troposphere. Considering the large amounts of snow which are optically thicker than ice, a more peaked heating rate shown in the RRTMG simulation may be to first order more realistic. Tang et al. (2017) also employed the Dudhia scheme, but based on the differences between the

Dudhia and RRTMG scheme, the upper-level response may be under-estimated and the low-level response may be over-estimated. The focus of the current study is on the physical mechanisms induced by shortwave radiation on the ERC, with the acknowledgement that these mechanisms may be partially dependent on the specific parameterizations used. The sensitivity of convective and stratiform clouds during an ERC to the full parameter space of cloud microphysics schemes, radiation schemes, and boundary layer schemes is beyond the scope of this study but remains an important area for future work. The sensitivity to between select cloud microphysics and shortwave radiation schemes will will be shown in Chapter 5.

3.3 Impact of Shortwave Radiation on ERC

Figure 3.2 shows the evolution of the 10-m maximum winds for each experiment with the black line indicating the Control. To first order, there is little change to the TC intensity evolution in the 48 hour restarts over the subsequent 48 hours. The result suggests that the rapid intensification processes ongoing in the eyewall of the simulation were not affected by different shortwave heating magnitudes despite changes to the outer core thermodynamics at this time. Between the experiments, a consistent relationship between shortwave heating and TC intensity does not manifest until the TCs begin to weaken slightly at the 120 hour mark. Interestingly, the simulations which had more shortwave heating tend to be stronger than simulations without any shortwave heating. There are two possible explanations for this difference. The first explanation is that the shortwave heating in the canopy strengthened the upper-level secondary circulation. Although a stronger secondary circulation at upper-levels is evident in the simulations, consistent with recent literature and will be shown in Section 3.4, these anomalies remain only at the upper-levels and do not manifest themselves in the low-level winds (Navarro et al. 2017; Ruppert and O'Neill 2019). Since the TCs were already weakening with an expanding tangential wind field, another explanation for this difference is that the differences in intensity between hours 120-156 are due to changes in the weakening associated with the ERC. The timing of the ERC is likely to blame for the prior differences in intensity given the spread in re-intensification beyond the 156 hour mark.

The timing of the ERC does not directly relate to the re-intensification of the 10-m maximum winds but the re-intensification does indicate a contraction of the secondary eyewall to smaller radii. The first TCs to re-intensify are the NoSW48 and NoSW96 experiments followed by the 0.5xSW48 and 0.5xSW. These simulations had less shortwave radiation relative to the Control and the ERC occurred earlier.

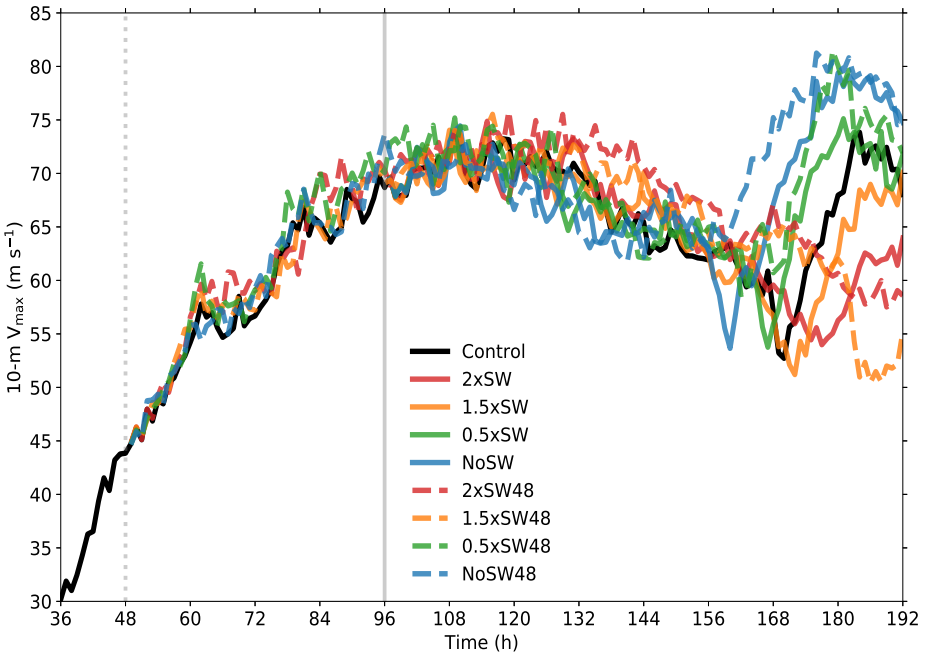

FIG. 3.2. The temporal evolution of the 10-m maximum winds for each experiment. The dashed lines are the experiments with radiation modified 48 hours into the simulation and the solid lines are the experiments with modified radiation after 96 hours. The vertical gray lines indicate the time of radiative modification.

The re-intensification also occurred earlier in the 48 hour experiments relative to the 96 hour experiments indicating that the more time that the radiation has to modify the environment, the larger the effect on both the environment and the timing of the re-intensification due to non-linear feedbacks. In the experiments with more shortwave heating relative to the Control, the 1.5xSW and 2xSW had a delayed re-intensification suggesting that stronger shortwave heating rates over the diurnal cycle had a delaying effect on the ERC. A re-intensification with the ERC did not occur in the 1.5xSW48 and 2xSW48 experiments within the simulation time frame but it is reasonable to assume that re-intensification would have occurred if the simulations were extended. These simulations suggest that both the shortwave heating magnitude over the diurnal cycle and the duration over which this heating occurs has an important effect in modifying the timing of the ERC. Because the re-intensification and ERC did not complete before the end of all of the 48 hour restart simulations, most of the discussion henceforth will be on the 96-hour restarts.

Figure 3.2 also suggests that there could be a relationship between shortwave radiation magnitude and the maximum intensity following the completion of the ERC. The maximum intensity of the NoSW experiment following the ERC is approximately 5 m s^{-1} stronger than the 0.5xSW experiment which is

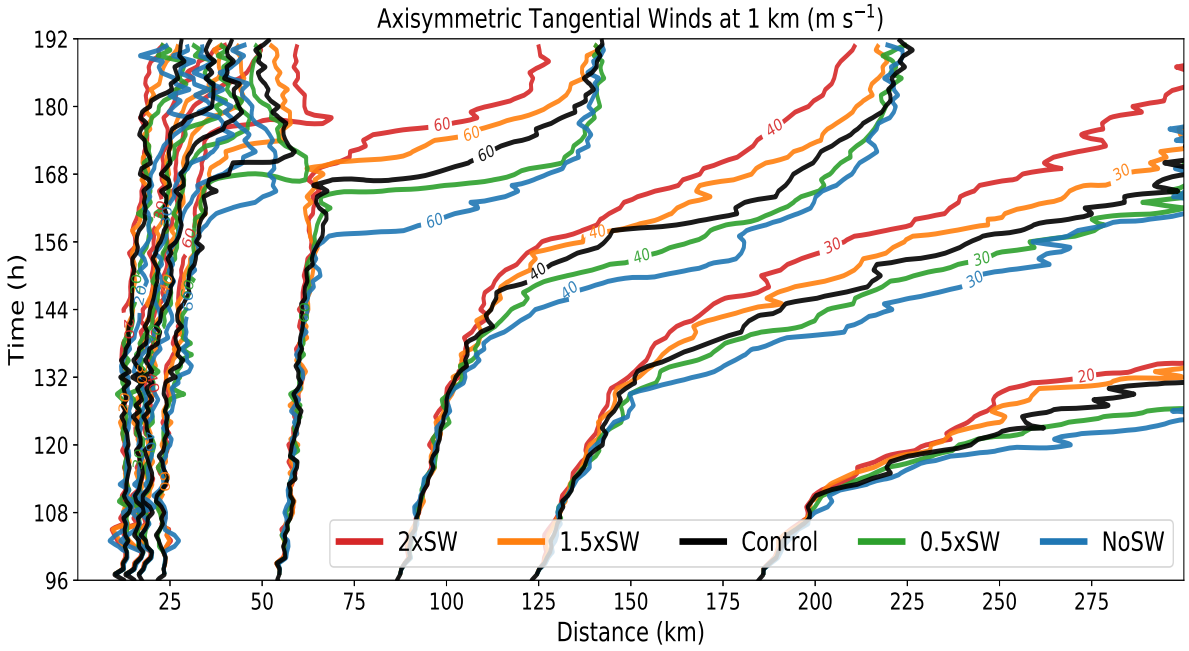

FIG. 3.3. Hovmöller diagram of the 1-km axisymmetric tangential winds colored by each 96 h restart experiment. Contours shown are for the 20, 30, 40, and 60 m s^{-1} tangential wind speeds. Tangential winds below 20 m s^{-1} and above 60 m s^{-1} are removed for clarity.

slightly stronger than the Control. The maximum intensity following the ERC of the 1.5xSW and 2xSW case are 5 m s^{-1} and 10 m s^{-1} weaker compared to the Control respectively. Although this relationship between the magnitude of shortwave heating and the maximum intensity after the ERC is suggested, it is difficult to assess the significance given the changes in the thermodynamic environment and the transition towards a new equilibrium state. The differences in intensity are due to a combination of factors including changes to the environment, surface fluxes, and differences in the radius of maximum winds (RMW). Figure 3.3 shows the evolution of the the axisymmetric tangential wind contours for the 96-hour restart experiments at an altitude of 1 km. The inner 60 m s^{-1} contour for the 2xSW and 1.5xSW is shifted towards larger radii further suggesting that the intensity differences after re-intensification are due to changes in the RMW. Near the end of the simulations, there is a 10 km difference between the RMW of the 1.5xSW and 0.5xSW and an even larger differences between the 2xSW and NoSW experiments. What governs the size of the RMW after the ERC is an open question that is outside the scope of the present study but may relate to the changes in the overall vortex structure and thermodynamic environment (Martinez et al. 2020).

The axisymmetric tangential winds are shown in Figure 3.3, confirming that the tangential winds broaden prior to the eyewall replacement cycle which is consistent with previous observations (Sitkowski

et al. 2011). The 20, 30, and 40 m s^{-1} tangential wind contours expanded earlier in the experiments with less shortwave radiation relative to the Control (i.e. 0.5xSW and NoSW) which also occurs in the 48 hour restart experiments. The expansion of the outer core tangential winds in the experiments occurs less than 36 hours into the restarts simulations. It should be noted that over the initial 48 hours there is no difference in the radius of the 60 m s^{-1} winds indicating that the effects of changes to the shortwave heating magnitude are first influencing the outer core radii beyond 150 km. This suggests that in these 96-hour restarts, the suppression of convection in the moat region by shortwave radiation as discussed in Tang et al. (2017) is not sufficient to explain the differences in low-level tangential wind anomalies in the outer core on short time scales. The overall outward expansion of the tangential winds suggests there is strong rainband diabatic heating outside the eyewall region, while the magnitudes of diabatic heating among the simulations are different.

To understand what governs the initial expansion of the tangential winds, the evolution of the 10-cm wavelength simulated reflectivity and tangential winds is analyzed in Fig. 3.4. The white contours show the radii where maximum shortwave heating is occurring which is always collocated within the near-eyewall anvil cloud where the largest optical depths and shortwave flux convergence occur. Although maximum shortwave heating rates below .5 K h^{-1} are not shown, warming due to to shortwave radiation does occur at all radii during daytime hours with varying magnitudes. Figure 3.4 again shows that the SEF and ERC in the 2xSW experiment occur later than the those in the NoSW experiment in both the tangential winds and simulated mean reflectivity. Between hours 96 and 120, which is the first 24 hours after the restarts, the axisymmetric mean simulated reflectivity beyond 150 km is stronger in the experiments with less shortwave radiation. As time progresses, the mean reflectivity in all the rainbands intensify but the rainbands with more shortwave radiation have overall lower reflectivity values. Collocated with the stronger reflectivity beyond 150 km in the experiments with less shortwave heating is the expansion of the 20 m s^{-1} tangential winds. Figure 3.4 suggests that the impacts of shortwave heating on the outer core rainband convection is the most important factor contributing to differences in the timing of the tangential wind broadening and subsequent ERC.

In this section it has been shown that shortwave radiation may impact the timing of SEFs and ERCs through the modification of outer core rainband convection. Together, these experiments confirm the sensitivity of ERCs to shortwave radiation discussed in Tang et al. (2017) in an idealized experiment, but further suggests that the stronger the magnitude of shortwave radiation and the longer time that radiation takes to impact the system, the larger the effect on the timing of the ERC. The relationship

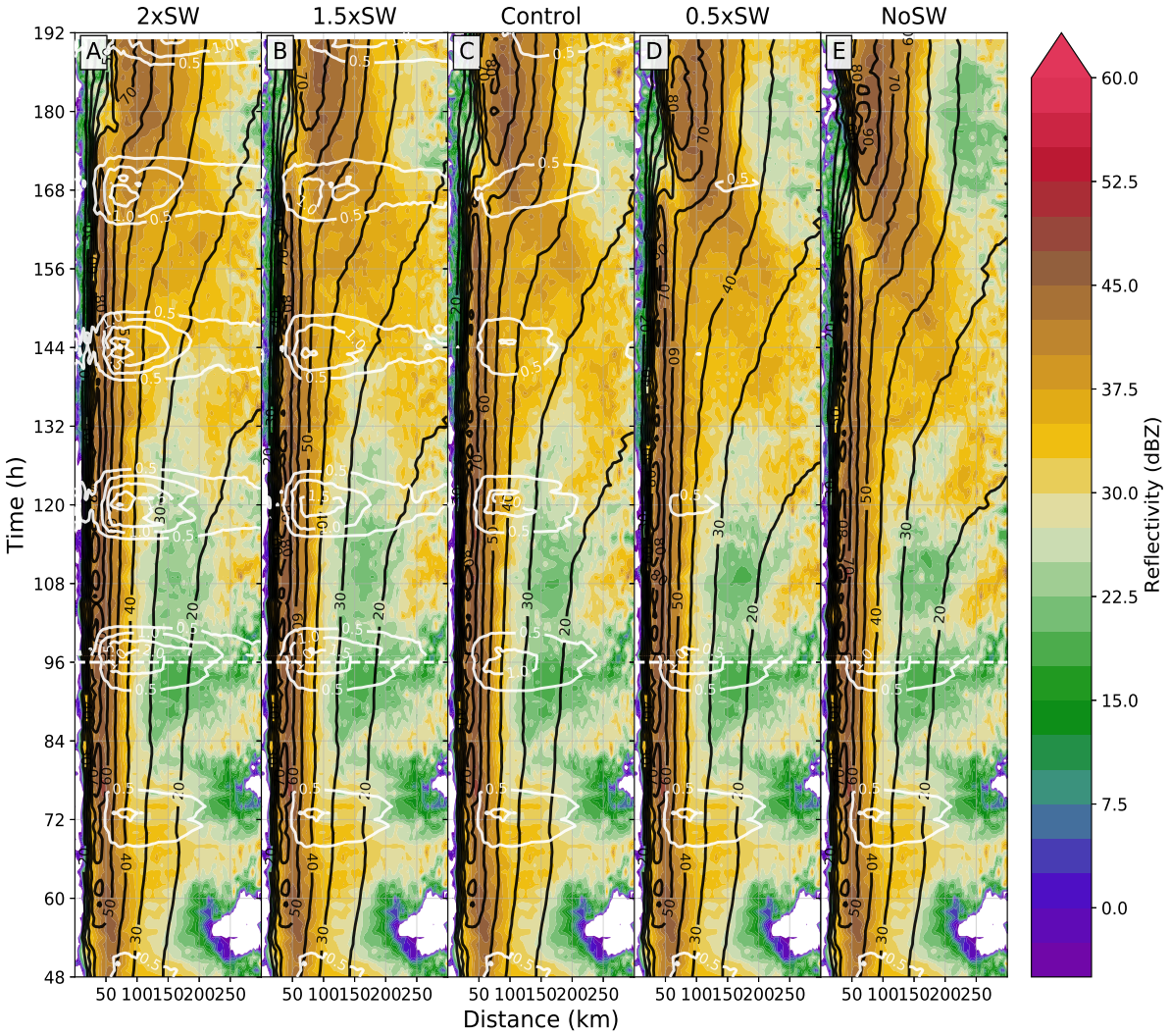

FIG. 3.4. Hovmöller diagram of the 1-km axisymmetric reflectivity (shaded), 1-km tangential winds (black contour), and maximum shortwave heating (white contour) for the 2xSW (a), 1.5xSW (b), Control (c), 0.5xSW (d), and NoSW (e) experiments. Contour intervals are 2.5 dBZ, 10 m s^{-1}, and .5 K h^{-1} for reflectivity, tangential winds, and shortwave heating respectively. Tangential winds below 20 m s^{-1} and shortwave heating rates below .5 K h^{-1} are removed for clarity. The white dashed lines indicate when changes to the radiation where made in the experiments.

between shortwave radiation and TC intensity following the completion of the ERC is complicated by the differences in RMW, but is an interesting avenue for further study. The structure and environment of the simulated TCs are next examined to explore the potential mechanisms by which the shortwave radiation affects the rainband convection to impact the ERC timing.

3.4 The Impact of Shortwave Radiation on TC Environment and Structure

How does shortwave radiation affect the structure of the simulated TCs prior to the ERC? Figure 3.5 shows axisymmetric radius-height profiles of RH and radial winds in the early morning and late afternoon for the Control experiment and corresponding anomalies between experiments. The anomalies are plotted such that Fig. 3.5c-d is the difference between one solar cycle and 3.5e-f is the difference between two solar cycles. In the early morning the RH anomalies are generally less than 3% with some larger RH anomalies corresponding to slight differences in the slope of the eyewall. The larger RH differences occur in the late afternoon and are present in both the anomalies of 1.5xSW from 0.5xSW and 2xSW from NoSW. Here, the important differences are where the anomalies are consistent with sign between Fig. 3.5d and 3.5f. There appears to be an increase in RH in the eyewall region with stronger shortwave radiation particularly at mid-levels which is at the start of the weakening of the primary eyewall as the ERC begins. Figure 3.6 shows the same time period as Fig. 3.5 but highlights the temperature and tangential wind differences between the models. The mean tangential winds in the eyewall decreased by ~ 10 m s^{-1} further supporting that the eyewall RH differences are due to a weakening primary eyewall. There is a noticeable reduction in RH due to stronger shortwave heating below 5 km in the region between 100 to 250 km radius (Fig. 3.5d, 3.5f). The RH differences maximize around 2 km and are reduced closer to the surface and actually reverse above 5 km. The RH differences at low-levels in the 100-175 km range are also evident in the early morning time periods with a weaker magnitude indicating that this effect may not be solely due to shortwave heating, although shortwave heating seems to exacerbate the anomalies.

In Fig. 3.5 there are differences in the radial winds, particularly in the outflow layer due to differences in shortwave heating in the late afternoon. The role of shortwave heating in the cirrus canopy and the influence on the TC outflow in relation to diurnal pulses (Dunion et al. 2014), remains an active area of research. Increases in the shortwave radiative heating in the cirrus canopy do induce changes in the outflow which are consistent with the Eliassen model (Eliassen 1952) with an anomalous outflow above the heating and anomalous inflow below the heating, but there is a small effect on the peak outflow values. In this framework, it appears that the stronger shortwave heating causes an increase in the overall height of the outflow layer. Overall the changes to the radial winds due to changes in shortwave radiation were larger than any changes in the primary circulation shown in Fig. 3.6. In the late afternoon there are stronger temperature anomalies as expected, which tend to maximize at upper levels due to solar absorption by optically thick clouds. Large temperature differences are also found in

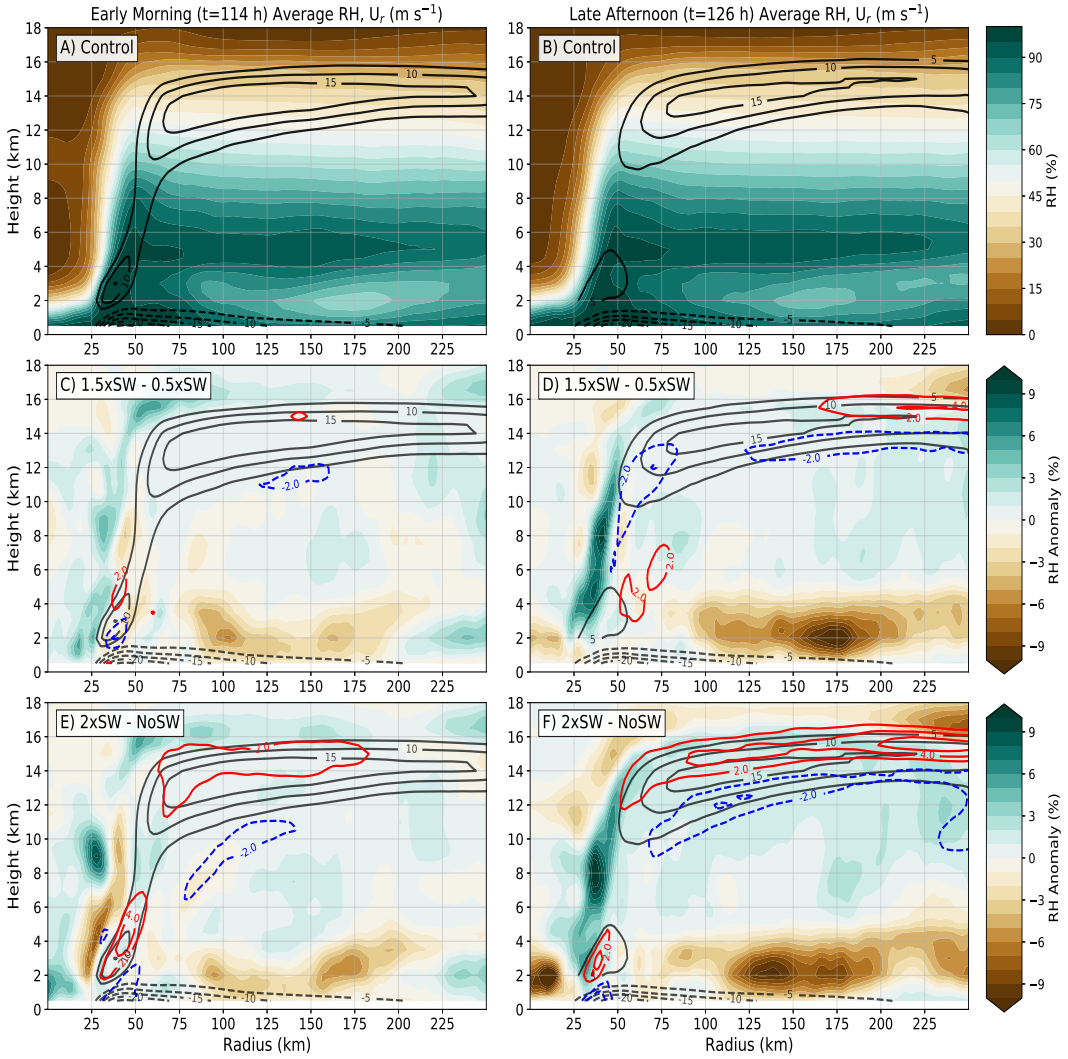

FIG. 3.5. Axisymmeterized cross sections of the RH (shaded) and radial winds (contoured) for the Control experiment during the early morning (a) and late afternoon (b). RH is shaded at 5% intervals while the radial wind is contoured every 5 m s^{-1} with the zero line removed for clarity. The time periods are a three hour average centered at the specified time to help smooth differences due to convection. The RH anomalies of the 1.5xSW experiment from the 0.5xSW experiment are shown for the early morning (c) and late afternoon (d) with the anomalies of the 2xSW experiment from the NoSW experiment shown for the same times in (e) and (f). The RH anomalies are contoured every 1% and the black radial wind contours are copied from the Control experiments for the given time period. The radial wind anomalies are contoured every 2 m s^{-1} with the zero line removed and red and blue colors representing positive and negative anomalies respectively.

the eye of the TCs which at low levels can be attributed to shortwave absorption in the near-infrared by water vapor. The temperature anomaly at the upper-level warm core in Figs 3.6d and 3.6f are attributed to the fact that the TC is already beginning to weaken as evident in the Control, so the strong anomalies in the eye are likely associated with an overall stronger storm in the 2xSW case relative to the NoSW as

the NoSW case is weakening during the ERC. The differences in the warm core temperature are indeed exacerbated by intensity differences in the storms as the tangential winds are stronger throughout the eyewall region while the outer-core tangential winds are weaker for the 2xSW case.

Overall, Figs. 3.5 - 3.6 are highlighted to show that there are few differences in the dynamics of the TC caused on short time scales by the stronger shortwave heating imparted on the storms. Similar to what has been shown by Navarro et al. (2017) and Ruppert and O'Neill (2019), the differences in circulation are primarily in the outflow layer due to shortwave heating anomalies, which do not induce a tangential wind response at low-levels that effects TC intensity. There are however, significant thermodynamic differences between the models due to the changes in shortwave heating magnitudes at both upper-levels and low-levels. The low-level reduction in RH in the simulations with larger shortwave heating is a product of the differences in convection and stratiform precipitation distribution and the associated microphysics which feedbacks onto the timing of the ERC, but is not the mechanism controlling the differences in ERC timing.

Previous studies including Melhauser and Zhang (2014) have shown that shortwave radiation has a negative impact on the thermodynamic environment of TCs which inhibits tropical cyclogenesis. The changes to the thermodynamic environment play a role in the 48 hour restarts; however, unlike Melhauser and Zhang (2014) the experiments shown here already have a well established TC with a cirrus canopy overhead in the 96-hour restart, so clear-sky changes to the thermodynamic environment do not apply over a large region. The clear-sky thermodynamic modification mechanism may still be important at longer simulation times and at larger radii but not over the first 48 hours. Another mechanism that has been proposed to explain the diurnal cycle of precipitation in the tropics is by Gray and Jacobson (1977) in which differential cooling between cloudy and clear skies results in a pressure driven inflow that enhances the cloud scale circulation. Within each experiment, changes to the inflow on a diurnal basis are not found, although some recent observational evidence using dropsonde measurements does suggest a diurnally varying inflow (Zhang et al. 2020). In the current study though the mechanisms described by Melhauser and Zhang (2014) and Gray and Jacobson (1977) appear to be of secondary importance. It should also be mentioned that there were no systematic differences in the longwave warming across experiments such that changes in the outflow layer could not be driven by the mechanism explained in Bu et al. (2014).

The temperature differences due to the changes in shortwave heating rates are important at the upper-levels for changing the static stability, while the temperature differences at low-levels can modify

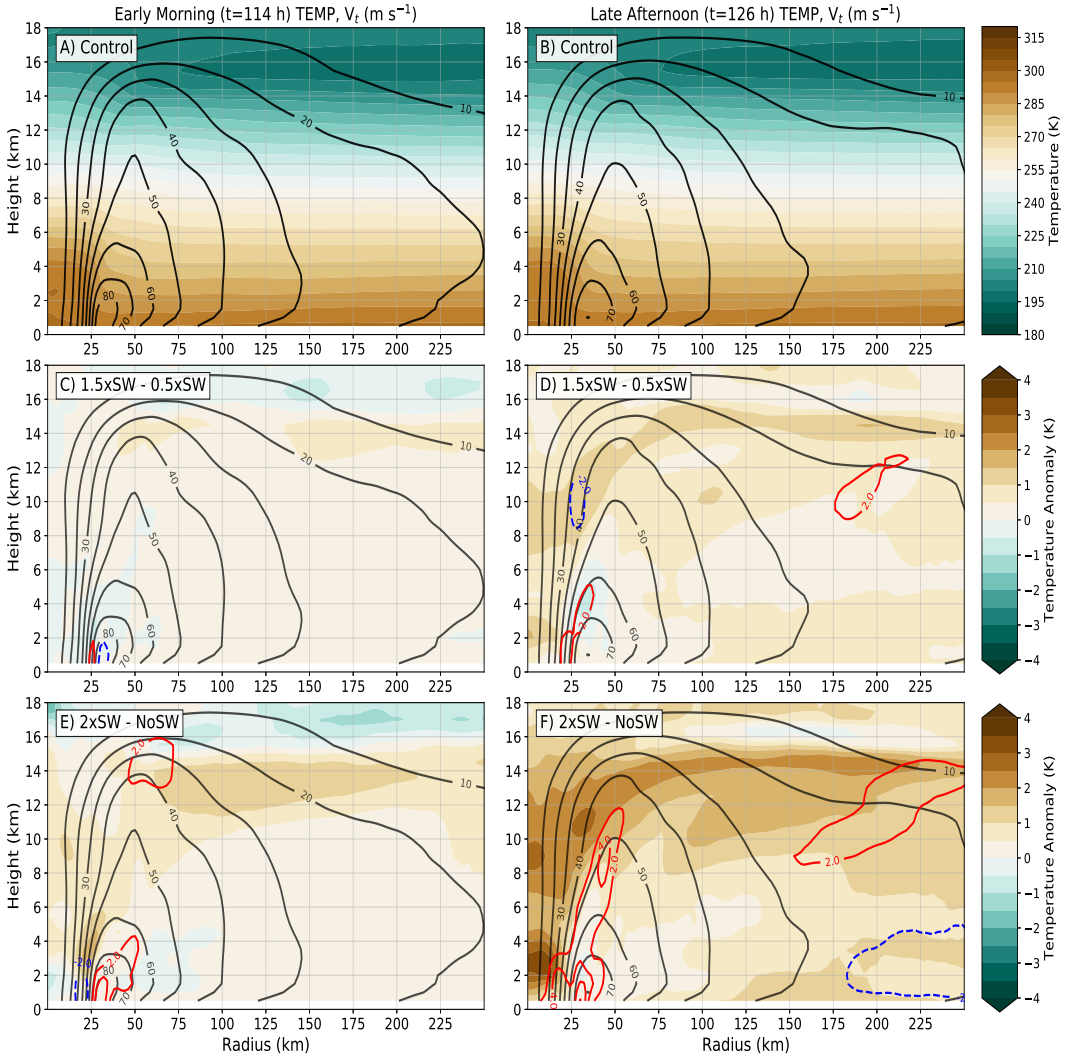

FIG. 3.6. Same as Fig. 3.5 but for temperature shaded every 5 K and tangential wind contoured every 10 m s^{-1} in the Control experiment. Temperature anomalies are contoured at .5 K intervals with tangential wind anomalies every 2 m s^{-1} with the zero line removed.

the air-sea disequilibrium. Both the modifications to the surface enthalpy fluxes and the changes to to the upper-level static stability are important in controlling the strength of convection in the rainbands which has been shown to be important for the generation of secondary wind maximums and SEF (Zhu and Zhu 2014). Figure 3.7 shows a box-and-whisker plot of the wind normalized sensible and latent heat fluxes for each experiment which all have statistically significant means that are different from the Control at the 99.9% confidence level. The simulations with more shortwave heating yield weaker wind normalized sensible and latent heat fluxes which can be attributed to a weaker equivalent potential temperature disequilibrium across the air-sea interface. The relationship between wind normalized enthalpy fluxes and shortwave heating is to be expected and will amplify after every diurnal cycle due

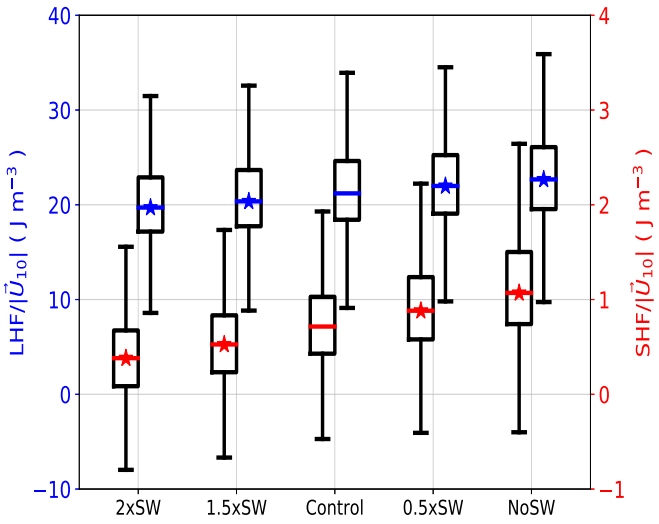

FIG. 3.7. Box-and-whisker plot of latent heat fluxes and sensible heat fluxes normalized by the magnitude of the 10-m winds for each of the 96-hour restart experiments over the first 36 hours of the simulations. The red and blue lines indicate the median of the normalized sensible and latent heat fluxes using the right and left ordinate respectively. The lower and upper quartile ranges are shown by the box while the whiskers extend 1.5 times the width of the box. Outliers beyond 1.5 times the width of the box are removed for clarity. The stars indicate that the mean of the sample is statistically significant from the Control at the 99.9% confidence level using a two-sided T-test.

to the radiation energy imbalance. It is important to note that one of the idealizations of this work is that the sea surface temperature is fixed, therefore excessive shortwave heating reaching the ocean surface and not being reflected cannot increase SST. If the surface enthalpy fluxes are not normalized by wind speeds, the differences in the domain integrated amount of surface fluxes would be considerably larger for the NoSW and 0.5xSW experiments relative to the control and reduced in the 1.5xSW and 2xSW experiments (not shown). Cheng and Wu (2018) found that a reduction in the surface fluxes similarly caused a delay in the timing of their idealized ERCs; however, the differences in fluxes between the experiments in this study are not as dramatic and primarily confined to the outer core region and not in the primary eyewall. The non-linear relationship between fluxes, convective generation and the increase in wind speeds is considered to be important for the changes in ERC timing as the TCs wind fields expand at different times but may not be responsible for the initial differences in tangential wind expansion.

Studies such as Xu and Wang (2010) and Cheng and Wu (2018) have suggested that surface sensible and latent heat fluxes are important for generating surface based CAPE which is then consumed by convection resulting in increased diabatic heating and subsequent changes to the tangential winds (Wang 2009). Figure 3.8 shows the evolution of the distribution of surface based CAPE values for the Control

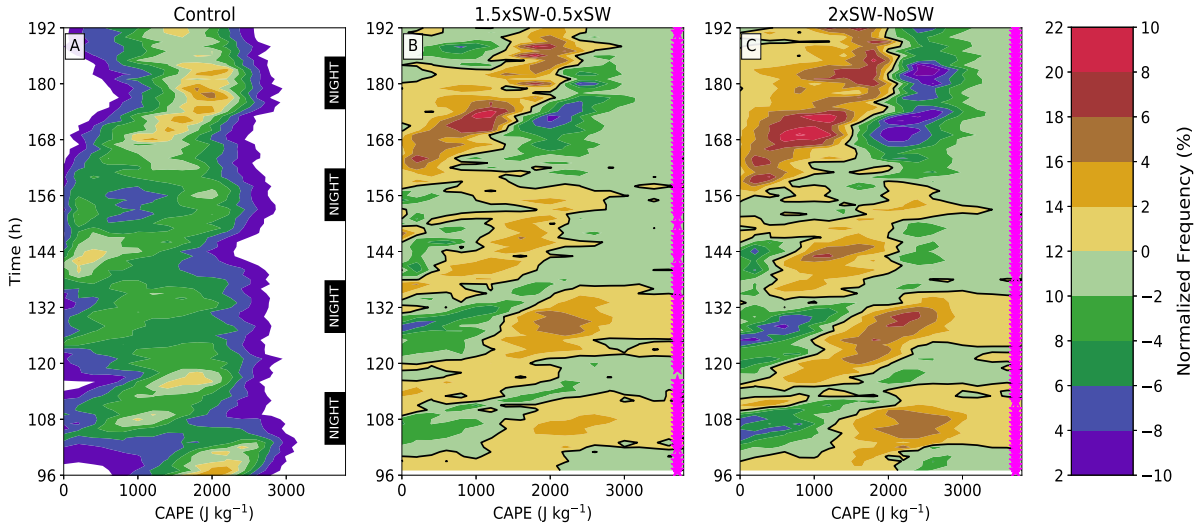

FIG. 3.8. Temporal evolution of the distribution of CAPE binned over 100 J kg^{-1} intervals at radii greater than 150 km in the innermost domain. The distribution of CAPE is normalized by the sum of all values over each hour with values that make up less than 2% removed in the Control shown in (a). The anomalies of the 1.5xSW from the 0.5xSW experiment is shown in (b) and the the 2xSW anomalies from the NoSW experiment is shown in (c). The black line highlights the zero anomaly line. The left side of the colorbar is representative of the temporal evolution of CAPE in the Control experiment while the right side of the colorbar is representative for the anomalies. The black rectangles highlight the times without shortwave radiation. The pink stars on the right-hand side of (b-c) indicate the times where the means of the CAPE distributions are statistically different at the 99% confidence level using a two-sided T-test.

and the anomalies for the experiments with the the modified shortwave heating rates. The distribution of CAPE is preferentially shown instead of the average values which can be misleading because CAPE is lowered once it is consumed by convection. It should also be noted that in this experiment, the surface enthalpy fluxes are not the only factor affecting the distribution of CAPE as any heating at the surface or cooling of the tropospheric temperature profile from radiation could increase CAPE. In the Control experiment, there is a large distribution of CAPE values between 1000 to 3000 J kg^{-1} which increases in the following six hours before shifting towards lower CAPE values as the instability is consumed by convection. The distribution of CAPE then increases again with continuous surface fluxes before once again being consumed leading to cyclic changes between convective development/invigoration and CAPE.

In Fig. 3.8b-c the anomalies of the 1.5xSW from the 0.5xSW experiment and 2xSW from the NoSW experiment are shown. In both subplots there is a slight shift in the distribution of CAPE over the first 6 hours with the 2xSW and 1.5xSW having distributions shifted towards lower values of CAPE. The differences over the first 6 hours can be attributed to differences in shortwave heating at upper-levels as this

corresponds to the time when shortwave heating is still ongoing with heating profiles similar to that shown in Fig. 3.1a. In the following 8 hours (102-110 h) there is a reversal in the distribution of CAPE with the NoSW and 0.5xSW having much lower CAPE values compared to the 1.5xSW and 2xSW experiment because the CAPE is being consumed by convection in the simulations with reduced shortwave heating. The consumption of more CAPE in the NoSW and 0.5xSW occurs at night even though there are no consistent or significant differences in the longwave radiative cooling and warming. The experiments with larger shortwave heating rates have larger CAPE values at this time, but that instability is not being consumed at the same rate due to increased stability. Consistent with the Control there is then a cycling of the anomalies which seems to show that CAPE is consumed in the NoSW and 0.5xSW at a faster rate than the 2xSW and 1.5xSW experiments through the end of the simulation. The distribution of CAPE values in the 2xSW and 1.5xSW is continually shifting towards lower values through the simulations which is expected because the overall temperature profile is warming due to an imbalance between shortwave heating and longwave cooling, which then directly reduces CAPE and also reduces the surface enthalpy fluxes.

It has been shown that the dynamics of the primary and secondary circulation of the inner core of the TCs in each experiment vary little in the short term due to the changes in shortwave radiative forcing, but there are important changes to the thermodynamic environment of the rainbands. Shortwave heating stabilized the mid-upper levels having a negative impact on the distribution of CAPE. Subsequent modifications to the surface sensible and latent heat fluxes grow with time over each diurnal cycle as the winds expand earlier and amplify the fluxes sooner. In addition, there are RH anomalies at low levels in the outer core which have yet to be thoroughly explained because the magnitudes exceed what is expected by increasing temperature alone. The RH differences are likely due to interactions between shortwave radiation and the microphysics scheme which will be highlighted in the next section. The following section will explore the relationship between shortwave radiation and the strength and distribution of convective and stratiform clouds in the outer core region prior to the ERCs.

3.5 Assessing the Changes to Convective and Stratiform Cloud Distributions

Up until now, how the shortwave radiation will effect the frequency or strength of convection in the outer core even has not been considered, though it can be inferred through the analysis of CAPE. To determine how shortwave radiation directly or indirectly affected convective and stratiform clouds, a partitioning algorithm is employed. The convective-stratiform partition utilizes horizontal reflectivity

gradients at an altitude of 2 km with thresholds based on Yuter and Houze (1997) and Steiner et al. (1995). This classification technique was compared with an updated version of the algorithm from Powell et al. (2016), which generates qualitatively similar results. The older algorithm is used because it employs fewer raintype classifications that are more stable for shorter timescales to allow for consistent time series.

The convective-stratiform partition was implemented only on the high resolution inner domain of the experiments and subcategorized based on radii from the TC centers. It is important to note a few limitations of the partitioning algorithm. Since the scheme is implemented at the 2-km level, the most homogeneous part of the reflectivity profiles will be at 2-km and will become more heterogeneous at altitudes above and below this layer. Because the algorithm is based on the reflectivity at one altitude, it must be assumed that the classification is valid for all the grid cells in that column and as such highly tilted convection may not be well resolved. However, convection in the model does not exhibit significant tilt and the partition assumes a convective radius such that multiple grid cells around a resolved convective core will be classified as convective. The same scheme is used on all of the experiments and normalized by the number of events in each experiment.

The temporal evolution of the frequency of both convective and stratiform classified echoes relative to the Control for the 96-hour restart experiments is shown in Fig. 3.9. The frequency of the echoes are integrated over the radii greater than 150 km in the inner domain and are smoothed using 10 iterations of a 1-2-1 filter with weights of .25, .5, and .25 respectively to improve figure readability. Over the first 6 hours where shortwave heating differences are ongoing in the model, there is an immediate change in the frequency of convection. The 0.5xSW and NoSW experiment both have a net increase in the number of convectively classified points while the 1.5xSW and 2xSW have a net reduction in the amount of convective classified points. Once the sun goes down and all the simulations have the same longwave cooling, the number of convective grid points in the region of interest become similar. The sun rises in the simulations around hour 114 and the convective area relative to the Control again decreases in the experiments with the stronger shortwave radiation. At times beyond hour 158 indicated by the vertical line, the secondary eyewall has formed in the NoSW and 0.5xSW simulations resulting in a decrease in the amount of convection at radii beyond 150 km, which makes comparing the TCs in this framework difficult. The overall change in convective frequency between the experiments prior to the ERC suggests a negative relationship between the magnitude of shortwave radiation and convective

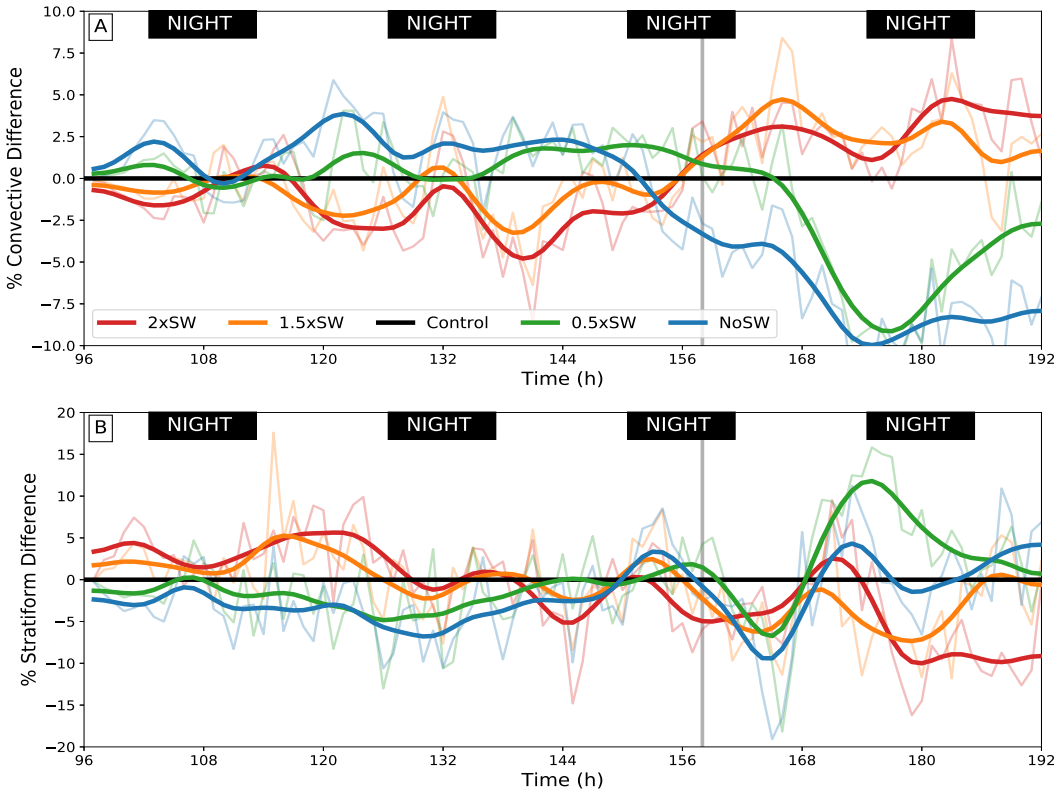

FIG. 3.9. Temporal evolution of the areal frequency anomaly of convectively (a) identified radar echoes and stratiform (b) identified echoes from radii greater than 150 km in the 96-hour restart experiments. The bold lines are filtered with 10 iterations of a 1-2-1 filter for clarity with the unfiltered data shown with the true data shown in the thinner and more transparent lines in the background. The gray vertical lines indicate a rough estimate of the timing of the ERC in the NoSW experiment. The black rectangles highlight the times where shortwave radiation is not present.

cloud amount due to changes in the mid-upper level static stability that was also suggested by the distribution changes of CAPE.

In Fig. 3.9b, the response of stratiform clouds to shortwave radiation is opposite to that of convective clouds. The simulations with more shortwave radiation had a larger fraction of stratiform clouds during the day compared to the 0.5xSW and NoSW experiments. To first order the differences can be explained by the decay of convective clouds into stratiform clouds as the shortwave heating stabilizes the upper levels. The stratiform clouds also ended to persist longer in the 2xSW and 1.5xSW experiments which is due to direct solar heating in the clouds amplifying the stratiform heating profile and vertical velocities in the upper-levels. Although stratiform heating may be important for ERCs, the magnitude of condensational heating by convection dominates the ERC timing in this experiment.

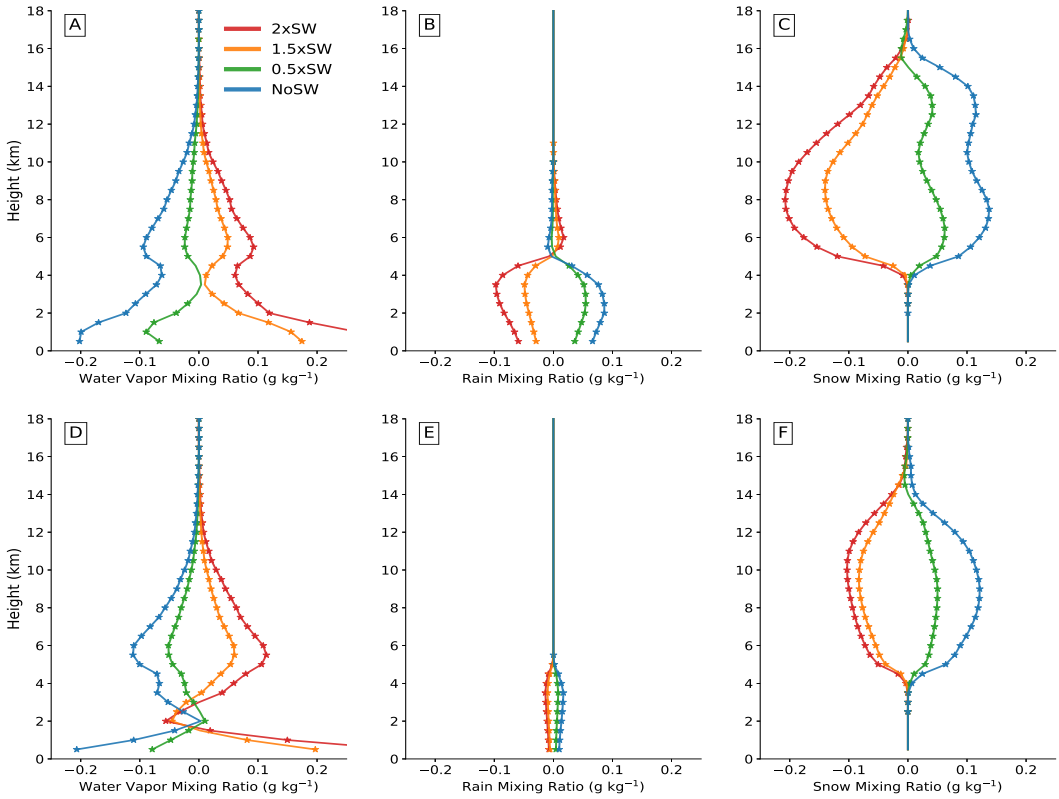

FIG. 3.10. Vertical profiles of the mean water vapor (a), rain (b), and snow (c) mixing ratio anomalies from the Control experiment for convectively defined areas. The anomalies are computed for only convective areas at radii greater than 150 km in the innermost domain over the first 48 hours of the 96-hour restarts. The vertical profiles for water vapor, rain, and snow mixing ratio anomalies are shown for stratiform classified regions in (d), (e), and (f) respectively. The circles indicate where the mean mixing ratio is statistically different from the Control experiment at the 99% confidence level using a two sided T-test.

In addition to effecting the area of convective and stratiform precipitation, shortwave radiation also affected the cloud microphysics. Figure 3.10 shows the vertical profiles of water vapor, rain, and snow mixing ratio anomalies for convective and stratiform identified clouds. The 2xSW and 1.5xSW simulations have reduced snow and rain mixing ratios while the experiments with less shortwave radiation have increased snow and rain mixing ratios in both convective and stratiform clouds. For convective clouds, associated with this reduction of snow and rain is an increase in the overall amount of water vapor with increased shortwave radiation. This suggests that solar absorption within the clouds is contributing to sublimation, melting and/or evaporation of snow at mid-upper levels and explains the higher RH found at those levels in Fig. 3.5. The overall convective heating profile from the microphysics is therefore reduced in the simulations with more shortwave radiation as shown by Fig. 3.11b. Conversely, when the shortwave radiation is reduced in the 0.5xSW and NoSW simulations there is an

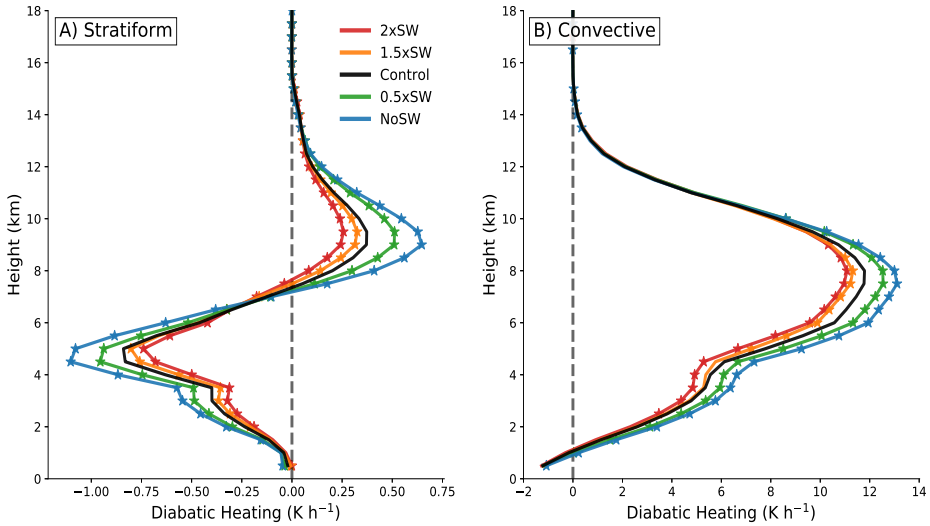

FIG. 3.11. Vertical profiles of the diabatic heating rate from the Control in areas classified as stratiform (a) and convective (b). The heating profiles are computed for only areas at radii greater than 150 km in the innermost domain over the first 48 hours of the 96-hour restarts. The stars indicate where the mean diabatic heating rate is statistically different from the mean of the Control experiment at the 99% confidence level using a two sided T-test.

increase in the amount of condensational heating associated with the increase in snow and rain mixing ratios. This further suggests that with decreased solar radiation, the increase in diabatic heating from the microphysics in deep convective clouds is responsible for the faster generation of a secondary wind maximum and ERC.

The stratiform cloud profiles show a similar response to the shortwave radiation as the convective clouds but smaller in magnitude with reduced rain and snow mixing ratios associated with more shortwave radiation. The reduction in snow generation is associated with a reduction in the condensate heating shown in Fig. 3.11a at upper levels. The reduction in rain mixing ratios below 5 km means that there is less rainfall that is able to evaporate contributing to a reduction in the evaporative cooling below the melting level. Overall there is a consistent relationship with stronger evaporative cooling in the NoSW and 0.5xSW experiment compared to the 1.5xSW and 2xSW experiment. Stronger cooling in the NoSW and 0.5xSW experiments means that stronger downdrafts can penetrate into the subcloud layer and enhance the surface sensible and latent heat fluxes. The opposite occurs in the 2xSW and 1.5xSW simulations where weaker downdrafts may not penetrate into the subcloud layer and contributes to the differences in fluxes shown in Fig. 3.7. The differences in water vapor of stratiform clouds near 2 km is also evident in the low RH anomalies found in Fig. 3.5, which can partially be explained by the transition between convective and stratiform precipitation. The weaker evaporation rates cause less

water vapor in this region. It is unlikely that the water vapor anomalies at 2 km are an artifact of the convective-stratiform partition which is run at that level, although it is uncertain how the effectiveness of the partition algorithm works in an evolving environment due to the imbalance between shortwave and longwave radiation. Rios-Berrios (2020) also found that the radiation-microphysics interactions, particularly in reference to rain evaporation, are a major source of uncertainty in numerical models and should be the focus of future work.

3.6 Conclusions

Recent work has shown that both shortwave and longwave radiation has important impacts on tropical cyclone structure, intensity, and track (Fovell et al. 2016). This study uses idealized WRF simulations to test the sensitivity of secondary eyewall formations and eyewall replacement cycles to diurnal shortwave radiation. This study has shown that shortwave radiation modifies the timing and TC intensity following the completion of eyewall replacement cycles through its direct influence on convection in the rainbands. Although the stabilization of the moat region by shortwave heating in Tang et al. (2017) may be important for SEFs prior to moat formation, it does not appear to explain the differences in timing of the ERCs within the idealized simulations presented here. The different results between the experiments shown here and the experiment in Tang et al. (2017) could be because this study has more intense TCs with the moat region already established and maintained by dynamically induced subsidence. The differences between studies could also be attributed to differences in the thermodynamic environment, for example the real case of Hurricane Edouard included the presence of moderate vertical wind shear (Tang et al. (2017) Fig. 2). It is hypothesized that both the differences in timing and differences in intensity of the ERC are due to the effects of shortwave radiation on rainband convection. The primary effect is not due to the direct radiative heating addition to diabatic heating in the rainbands but instead through the indirect modification of the microphysical heating rates through changes to the stability and large-scale thermodynamic environment.

On short time scales of less than 48 hours, shortwave radiation modified the timing of the ERC first through a modification of the stability at upper-levels of the preexisting convective and stratiform clouds. The stronger the shortwave heating, the stronger the stabilizing affect within both the convective and stratiform clouds which caused a reduction in the cloud scale heating profiles in the simulations with more shortwave heating compared to those without any. The upper-level shortwave

heating resulted in a reduction of convective area and an increase in the area of stratiform precipitation. The reduction in convective diabatic heating in the 2xSW and 1.5xSW experiments results in the generation of a weaker secondary wind maximum, which takes longer to grow given similar inertial stability profiles of the vortex similar to that shown in Zhu and Zhu (2014). Over time, the secondary wind maximum differences are amplified by surface sensible and latent heat fluxes and the generation of CAPE (Cheng and Wu 2018). At longer time scales (beyond 48 hours) where the radiation has more time to modify the large-scale thermodynamic environment, the differences in ERCs are also delayed due to non-linear feedbacks and multiple radiative-convective interaction mechanisms.

This work suggests that regardless of the TC intensity, the diurnal cycle of radiation plays a role in the convective and stratiform nature of the rainbands and can then affect the TC intensity through ERCs. Although this study is based on a set of experiments with a single set of cloud microphysics and radiation schemes, the results suggest that the interactions between radiation schemes and microphysics schemes employed by operational models could lead to differences in ERCs that are explicitly simulated. The changes to the convective-stratiform distribution and associated heating profiles could then lead to errors in forecast estimates of wind radii and to TC intensity. Subsequent work is needed to test the additional sensitivities of radiation and cloud microphysics to the boundary layer scheme and ocean coupling. A complete sensitivity analysis between radiation schemes and the important interactions with the microphysics schemes will be the focus of future work.

In the framework of this study, where the experiments are constrained by the initial condition at the time of the simulation restart, the sensitivity to stochastic changes in convection has not been assessed. Assessing the sensitivity to stochastic changes in convection is difficult because small perturbations would have a limited impact on the already established vortex and convective rainbands. Small perturbations to the system might therefore overestimate the confidence in small magnitude differences between the experiments. Given that there was little to no change in the intensity of the simulated tropical cyclones for almost 48 hours despite large differences in shortwave radiation, larger perturbations to the model to create an ensemble would likely overwhelm the radiative signal which aggregates over multiple diurnal cycles. Although the results of this study are based on single model runs, given the ensemble variability due to stochastic perturbations in boundary layer moisture at model initialization of the system shown in Trabing et al. (2019), the differences in the timing of the ERCs are robust. Further research should be considered on the role that radiation plays in ensemble variability, particularly for the purpose of gauging statistical significance.

CHAPTER 4

OBSERVATIONS OF DIURNAL VARIABILITY UNDER THE CIRRUS CANOPY OF TYPHOON KONG-REY (2018) [1]

4.1 INTRODUCTION

Modeling experiments have shown that radiation plays an important role in the evolution of tropical cyclones (TCs) and their forecasts (Sundqvist 1970; Craig 1996; Nicholls 2015; Fovell et al. 2016; Navarro et al. 2017; Trabing et al. 2019; Ruppert and O'Neill 2019). Including radiation in models often leads to increases in rates of tropical cyclogenesis and mitigates the negative effects of vertical wind shear allowing intensification to occur sooner (Melhauser and Zhang 2014; Nicholls 2015; Rios-Berrios 2020; Smith et al. 2020). The interactions between the microphysics and radiation schemes can lead to forecast errors in the tracks of TCs and differences in storm size that would affect wind radii forecasts (Fovell et al. 2010; Bu et al. 2014; Fovell et al. 2016). Improvements in TC forecasting may require improved understanding and representation of cloud-radiative processes in forecast models through observational analysis and verification (Fovell et al. 2016). The current study aims to improve the understanding of these processes through analysis of field observations of the diurnal cycle of convection in rainbands under the cirrus canopy of an intensifying tropical cyclone.

Modeling studies of idealized tropical cyclones have shown that solar radiation affects the distribution of rainband convection. Zhou et al. (2016) found that solar radiation impacts rainband convection by modulating the strength of cold pools. Tang et al. (2017) found that solar heating at upper-levels is important for stabilizing the moat region of Hurricane Edouard (2014) simulations, which causes convection outside of the eyewall to develop at larger radii. The location of primary rainbands was critical for the accurate formation of secondary eyewall in the simulated Hurricane Edouard. Chapter 3 found that shortwave heating in the upper levels of rainband convection is responsible for weakening convective clouds during the day and can modify the timing of eyewall replacement cycles. Kossin and DeMaria (2016) showed that large intensity forecast errors can sometimes be attributed to the lack of accurate eyewall replacement cycle prediction. However, it has also been noted that a cycle of convection on a diurnal timescale in simulated tropical cyclones does not require shortwave radiation. Li and Wang (2012) showed a 22-26 hour cycle of inner-core rainbands associated with the boundary layer recovery timing of convective downdrafts and consumption of convective available potential

[1] The contents of this chapter have been submitted to be published in Monthly Weather Review by the American Meteorological Society (AMS).

energy (CAPE). Observations of the the diurnal cycle of convective rainbands associated with tropical cyclones are lacking, but are needed to verify the analyses of idealized numerical model studies.

It is well established that the diurnal cycle of precipitation over the ocean in the tropics reaches a peak in the early morning hours (e.g. Gray and Jacobson 1977; Steranka et al. 1977). The cirrus canopy is formed when deep convection penetrates the stable outflow layer and should therefore lag the diurnal cycle of convection (Merritt and Wexler 1967; Duran and Molinari 2016; Houze 2010). Cirrus clouds above TCs are thought to be generated by the strong inner-core convection and advected outward, but it is unclear how much rainband convection contributes to the volume of ice in the cirrus canopy. Studies have shown that the areal extent of the cirrus canopy is minimized in the early morning and maximized in the afternoon, which supports the lagged response from the diurnal cycle of inner-core convection (Muramatsu 1983; Steranka et al. 1977; Wu and Ruan 2016). Cirrus clouds have been shown to modify the diurnal cycle of deep convective clouds in addition to their own diurnal cycle. Using observations from both microwave and infrared satellites, Hong et al. (2006a) found a two hour delay in the diurnal cycle of convection due to cirrus clouds and an enhancement of the diurnal variations in the 210 K deep convective clouds. One mechanism by which the cirrus canopy can modulate the the diurnal cycle of convection is through modification of the location and magnitude of shortwave and longwave radiative tendencies in the atmosphere. A thin cirrus canopy would result in more reflection of shortwave radiation, while a thicker canopy would result in absorption within the cloud, and both would reduce the magnitude of shortwave radiation available to warm the ocean surface. In addition to physical impacts, diurnal oscillations in the areal extent of cold upper-level clouds over tropical cyclones can cause forecast impacts by causing variations in the Dvorak pattern-recognition technique for objectively estimating intensity (Muramatsu 1983; Dunion et al. 2014).

The diurnal cycle of tropical cyclone rainband convection, and any impacts from the cirrus canopy, may be complicated by the existence of outward propagating rings of cold infrared (IR) brightness temperatures. A growing body of work has documented these propagating cold rings within the outflow layers of mature tropical cyclones, referred to hereafter as diurnal pulses or cooling pulses (Dunion et al. 2014). Although diurnal pulses were initially discovered in strong tropical cyclones, Ditchek et al. (2019a) found that diurnal pulses occur in 80% of major hurricane days, 64% of minor hurricane days, and 46% of tropical storm days in the Atlantic. Their study also shows variability in the pulses based on the thermodynamic environment and documents the occurrence of warming pulses. Knaff et al. (2019) examined all northern hemisphere storms from 2005-2015 and found reduced percentages of

storms with diurnal oscillations compared to Ditchek et al. (2019a), with 61%, 54%, and 45% of major hurricanes, hurricanes, and tropical storms having a moderate-strong diurnal signal, respectively. Knaff et al. (2019) suggests that the prevalence of diurnal oscillations in the brightness temperatures of tropical cyclones is affected by factors controlling the azimuthal symmetry, such as the vertical wind shear, intensity, and storm motion. The importance of a favorable environment for convection, particularly the upper-level relative humidity, has been suggested by multiple recent studies to be also important for diurnal pulses (Ditchek et al. 2019a; Knaff et al. 2019; Ditchek et al. 2019b). It is unclear, however, what factors contribute to variations in the time of initiation of diurnal pulses and why weak tropical cyclones may exhibit diurnal pulses with a weaker secondary circulation.

The underlying mechanisms that govern the initiation and propagation of diurnal pulses are an active area of research. Dunion et al. (2014) noted several initiation mechanisms that could be at play including convective coupled gravity waves, cloudy-clear sky radiative disequilibrium (Gray and Jacobson 1977), direct radiative-convective interactions (Xu and Randall 1995), radiatively reduced outflow resistance (Mecikalski and Tripoli 1998), and/or a seeder-feeder mechanism from falling ice crystals (Houze et al. 1981). It is unclear whether all diurnal pulses are coupled with convection or if the features are driven by processes solely in the outflow layer. Ditchek et al. (2019b) used ground-based lightning observations to show that diurnal pulses are electrically active ∼61% of the time. The correlation of cooling pulses with lightning suggests a coupling with deep convection strong enough to generate enough charge to produce lightning. The recent modeling study by Dunion et al. (2019) suggests that diurnal pulses can be characterized by outwardly moving squall lines with associated gust fronts. Dunion et al. (2019) showed that the outward moving squall lines tend to decrease in height with increasing radius because of increased static stability due to shortwave warming during the day. One hypothesis suggested by O'Neill et al. (2017) is that the diurnal pulses are linked to gravity waves that may be initiated by an enhancement of convection in the inner core that becomes coupled with convection as it moves radially outward. The mechanisms controlling how cooling pulses become coupled to outward propagating squall lines or why they are consistently tied to the diurnal cycle are still open questions.

Diurnal pulses have been examined primarily using satellites and numerical models, but multi-dimensional observations of diurnal pulses are lacking. Observations of diurnal pulses from below the cloud layer in a marine environment have not been previously examined to the author's knowledge. During the Propagation of Intraseasonal Tropical Oscillations (PISTON) field campaign, diurnal

pulses in the infrared brightness temperatures were evident during Typhoon Kong-rey's (2018) rapid intensification. The thermodynamic and kinematic properties of the environment of Typhoon Kong-rey were sampled during PISTON over multiple days with ship-borne observing systems, which will be discussed in Section 4.2. These observations provide a novel look at convective and stratiform cloud properties of the TC rainbands and environment under a cirrus canopy in which multiple diurnal oscillations in the brightness temperatures are found. Using a suite of observations, this study seeks to understand the diurnal variability of convective and stratiform precipitation under a broad cirrus canopy and explore the characteristics of diurnal pulses from a new perspective. This study provides new insight into the complex interactions between radiation and tropical cyclone rainbands that can be used to validate future modeling studies and improve forecasts. The observations from PISTON will help us address the following questions:

- How does the diurnal cycle of convective and stratiform precipitation vary under the cirrus canopy of Typhoon Kong-rey?
- What role does the thermodynamic environment play in the variability of outer-core rainband convection?
- Are the diurnal pulses in Typhoon Kong-rey convectively coupled and consistent with previous modeling studies?

In order to answer the questions posed above, the study is organized as follows. Section 4.2 will detail the observations collected during PISTON that will be used in this study. Section 4.3 will show how convective and stratiform clouds varied while under the cirrus canopy of Typhoon Kong-rey and with the diurnal cycle. The observations of the outward propagating cold rings which will be herein referred to as "cooling pulses" will be shown in Section 4.4. The results of this chapter will be discussed in Section 4.5.

4.2 Data and Methods

To investigate the diurnal cycle of convection of tropical cyclone rainbands in detail, novel observations collected during the PISTON field campaign in the summer of 2018 are used. As part of PISTON, observations from two cruises of the R/V *Thomas G. Thompson* were collected in the western North Pacific from mid-August to mid-October. Although the original goal of the experiment was intended to observe the ocean and atmospheric response to the Boreal Summer Intraseasonal Oscillation (BSISO), persistent typhoon activity near the area of operations comprised most of the variability

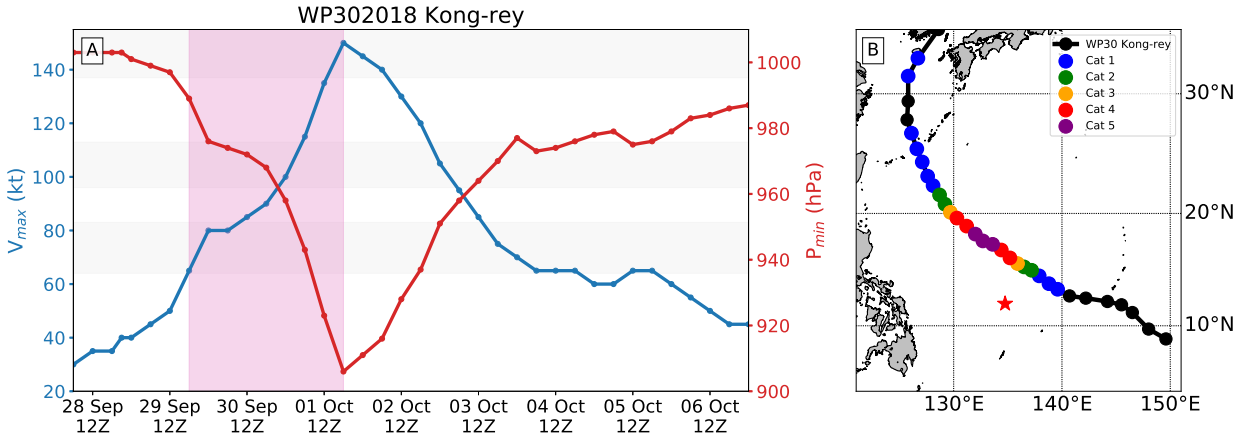

FIG. 4.1. (a) The intensity evolution of Typhoon Kong-rey in regard to 1-minute sustained maximum wind speeds and minimum central pressure. The red shading indicates the times where the R/V *Thomas G. Thompson* was within 500 km of the tropical cyclone center. (b) The track of the Typhoon Kong-rey's center with the red star indicating the general position of the R/V *Thompson* over the time frame of interest. Colors represent the corresponding Saffir-Simpson category based off maximum surface wind speeds.

in the observed ocean and atmosphere states during the project period. The focus of this study will be on Typhoon Kong-rey (WP302018) which was a well-observed typhoon during the experiment. Typhoon Kong-rey slowly tracked near the R/V *Thomas G. Thompson*, allowing detailed observations of the convective rainbands to be collected under a broad cirrus canopy. Space-based and ship-borne observations are leveraged in this detailed case study of Typhoon Kong-rey.

The track and intensity of Typhoon Kong-rey in this study are taken from the best track database produced by the Joint Typhoon Warning Center (JTWC). The track and intensity evolution of Typhoon Kong-rey from the JTWC are shown in Fig. 4.1. The colored shading highlights the two-day period that the R/V *Thomas G. Thompson* was within ~500 km of the center of Kong-rey during rapid intensification (RI) from a tropical storm to a Category 5 on the Saffir-Simpson wind speed scale (Schott et al. 2012). It should be noted that observations outside the shaded region are still being collected but are at further storm relative radii and are to some degree less constrained by TC dynamics. Kong-rey tracked to the northeast of the ship, which was at a relatively fixed location over the entire time period of interest. After reaching peak intensity, Kong-rey began to weaken due to the effects of cold water which was upwelled after Super Typhoon Trami stalled days earlier. Overall, observations of Typhoon Kong-rey's rainbands under anvil-like cirrus clouds were collected over a period of three and a half days.

Over the entire PISTON field campaign, the thermodynamic environment was sampled every three hours with 375 soundings released in total. The large number of radiosondes over the course of the field

campaign allows for a good comparison between the observations surrounding Typhoon Kong-rey and the PISTON mean environment. During the passage of Typhoon Kong-rey, 17 consecutive radiosondes were launched within 500 km of the 6-hourly TC center. A total of 33 radiosondes were launched between 06 UTC Sep 29 and 00 UTC 3 October while a broad distribution of upper-level clouds were prevalent overhead. Radiosondes were both objectively and subjectively quality controlled following the procedures of Ciesielski et al. (2011). In addition to the soundings, observations are incorporated from a radiometer measuring downward solar fluxes and a high spectral resolution lidar (HSRL) which is used to estimate cloud base height. The HSRL backscatter is used at 10 minute temporal and 60 m vertical intervals. Together, these instruments are able to provide insights into the diurnal changes in the thermodynamics.

An important tool for this analysis is the new Sea-Going Polarimetric (SEA-POL) radar. SEA-POL is the first polarimetric C-band weather radar designed to deploy on research ships for the U.S. research community (Rutledge et al. 2019). SEA-POL allows us to examine the variability of precipitating cloud distributions during PISTON. The radar has a range of 120 km and completed full volume scans every 12 minutes with scanning levels modified based on the proximity of high dBZ echoes to the radar. SEA-POL has a limited 240° field of view relative to the ship direction because its position on the forward “02" deck. Since the radar does not have a complete 360° field of view, changes in the ship direction can lead to changes in the observed distribution of clouds. Despite the limited field of view, SEA-POL provides a large enough sample size for good comparisons of convective characteristics in different environments. Quality control procedures for SEA-POL data includes a correction for ship motion, beam attenuation, and the removal of non-meteorological clutter (Rutledge et al. 2019).

The key SEA-POL radar moments that will be evaluated in this study are the reflectivity and the differential reflectivity (ZDR). Reflectivity is the backscattered power in units of dBZ which provides information on the size and number concentration of particles. ZDR is the difference between the horizontally and vertically polarized reflectivity factors in units of dB, which provides information on the shape of the particles. SEA-POL data is regridded to a Cartesian grid using the tools in the Lidar Radar Open Software Environment (LROSE; Bell 2019). A convective-stratiform partition algorithm is employed on the gridded reflectivity data to objectively identify areas of convective precipitation, stratiform precipitation, and clouds with weak echoes. The convective-stratiform partition developed by Steiner et al. (1995) and upgraded by Yuter and Houze (1997) is used, which identifies regions based on reflectivity thresholds and the horizontal reflectivity gradient at 2 km. Sensitivity tests indicate the

Yuter and Houze (1997) algorithm provides similar results compared to Powell et al. (2016), with less rain-type categories but a more coherent time series. The focus of this work will be on both the convective and stratiform components of the tropical cyclone outer-core rainbands, which have been shown to be important in affecting tropical cyclone intensity change (Wang and Tan 2020).

The observations near the surface from the R/V *Thomas G. Thompson* were supplemented by the global observing system. Cloud top temperatures in the infrared (IR) from the Himawari-8 Advanced Himawari Imager are explored to identify the presence of cold upper level clouds within the cirrus canopy and variations therein associated with diurnal pulses. Infrared bands at 10.4, 11.2, and 12.3 μm were analyzed, but here the focus is primarily on the 10.4 μm infrared band. At cold temperatures, the difference between the infrared bands is small and the results shown are not sensitive to the band chosen. Passive satellite imagery from the Tropical Cyclone Precipitation, Infrared, Microwave, and Environmental Dataset (TC PRIMED; Razin et al. 2019) are used to observe cloud structure below the cirrus clouds when available. The 89-91.6 GHz channels from SSMIS and GMI satellites identify deep convective clouds associated with Typhoon Kong-rey's rainbands which generated large distributions of ice species. The microwave imagery provides only snapshots at irregular time intervals and will be used to evaluate convective organization near Typhoon Kong-rey's center where ship-borne observations are impossible.

4.3 Rainbands Under the Cirrus Canopy

The distribution of cloud top IR brightness temperatures is first documented to provide context of the cirrus canopy in the PISTON domain. Figure 4.2a shows the evolution of the distribution of brightness temperatures in a 120 km x 120 km area centered on the location of the R/V *Thompson* during the time period surrounding Typhoon Kong-rey. The passage of upper-level cirrus clouds over the ship first occurs around 12 UTC Sep 29 when the distribution of brightness temperatures shifts from warm IR temperatures between 280 – 300 K to mostly cold clouds between 210 – 230 K. From 12 UTC Sep 29 to 18 UTC 2 October the distribution of cloud top temperatures are predominantly between 210 – 230 K suggesting the presence of clouds reaching altitudes of 10-14 km over the entirety of ∼3.5 days. The present study focuses on this time frame with the continuous presence of a cirrus canopy and anvil cirrus. The upper-level cloud distribution shown is a combination of cirrus emanating from Typhoon Kong-rey's inner-core convection with a smaller contribution from the convective rainbands.

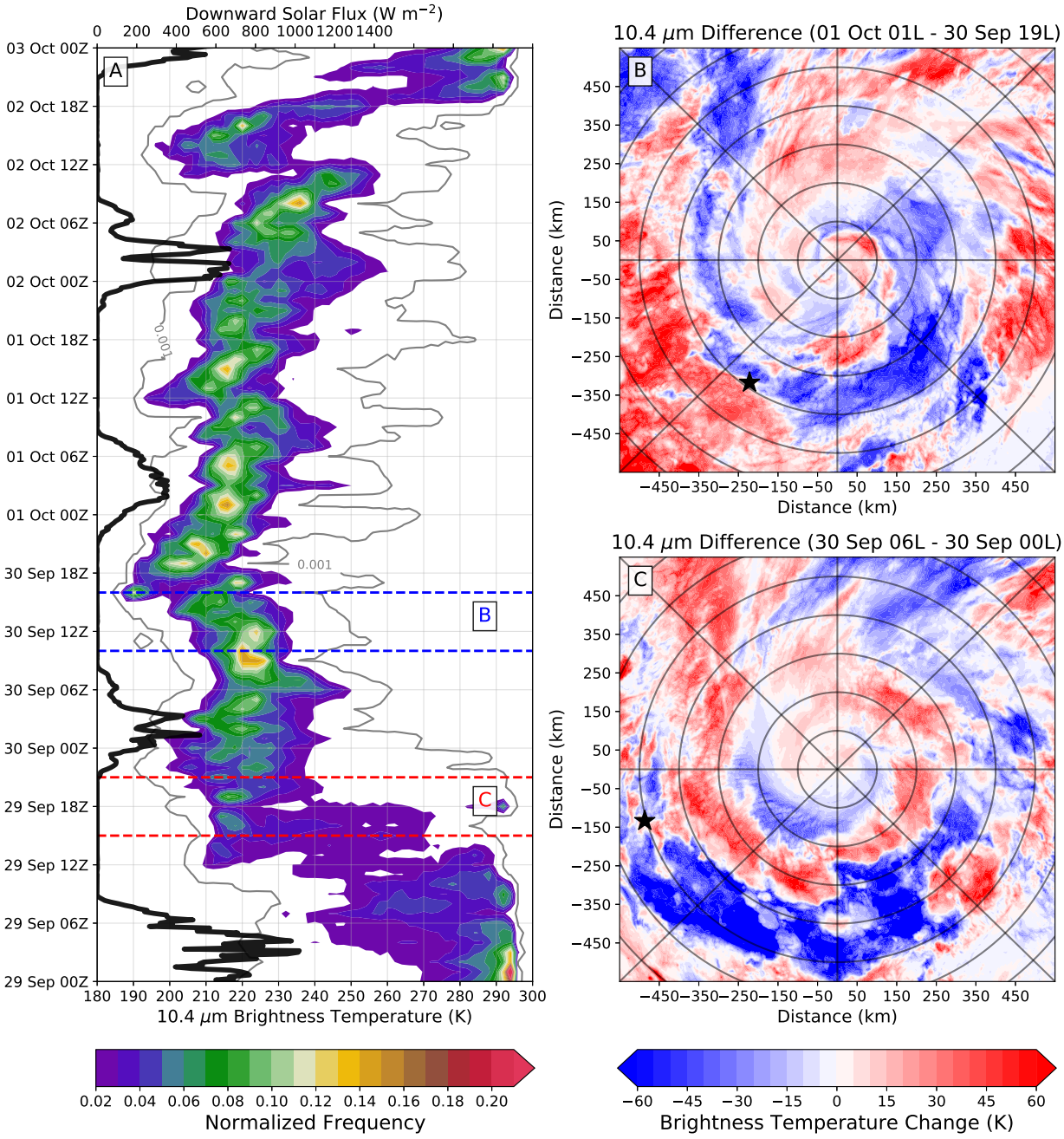

FIG. 4.2. (a) The temporal evolution of the distribution of 10.4 μm brightness temperatures from Himawari-8 over a 120 km by 120 km box centered over the R/V *Thomas G. Thompson*. Brightness temperatures are binned at 1 K increments and normalized by the number of pixels in the box. The gray line is the .001 frequency contour. The black line is the downward solar flux observed on the R/V *Thompson* during the time period using the top abscissa. The blue and red dashed lines are the time periods of brightness temperature differencing corresponding to the TC centered imagery in (b) and (c) respectively. Range rings are every 100 km and the black star is the mean location of the R/V *Thompson* over the 6 hours.

In addition to the continuous presence of upper-level clouds during the Kong-rey time period, there is considerable variability in the distribution of brightness temperatures. For coordination with the diurnal cycle, the black line in Fig. 4.2a shows the measured solar downward flux from the ship-based radiometer. The downward solar flux is reduced compared to clear sky days due to the absorption and reflection by the clouds above. The measured downward solar flux over the three cloudy days never exceeded 700 W m^{-2} with peak measured fluxes on 1 October reaching only 400 W m^{-2}. The peak downward solar fluxes during clear skies reached around 1200 W m^{-2} during PISTON, suggesting that the clouds and atmospheric gases scattered and absorbed between 40–70% of the incoming solar energy. The coldest brightness temperatures ($\leq$200 K) are primarily found at night or in the early morning times, likely associated with deep convection and is consistent with past studies. During the daytime, UTC times from ~21 UTC–09 UTC (~06L-18L), there is a noticeable shift in the peak of the brightness temperature distributions to warmer temperatures. The presence of warmer brightness temperatures in the afternoon away from the storm center are consistent with previous studies such as Steranka et al. (1977) and Wu and Ruan (2016). Although the colder brightness temperatures at night and warmer brightness temperatures during the day are consistent with the diurnal cycle of convection in the oceanic tropics, the TC circulation complicates the interpretation. It is unclear if the changes in brightness temperatures are a response to ice generated by deep convection in the inner core of the TC that is ejected radially outward in the outflow layer, or due to the diurnal cycle of convection in the rainbands. It is noted here that there were two periods where outward propagating diurnal pulses were observed at the ship, denoted by the blue and red dashed lines, which both occurred at night. These diurnal pulses will be analyzed in more detail in the next section.

To analyze differences in the clouds under Kong-rey's cirrus canopy, contoured frequency by altitude diagrams (CFADs) of the reflectivity and differential reflectivity measured by SEA-POL are analyzed. Using the convective-stratiform partition, the reflectivity of convective and stratiform precipitation features associated with Typhoon Kong-rey is compared to the full distribution of convective and stratiform clouds during the PISTON field campaign in Fig. 4.3. Due to the differences in sample size, the CFADs are normalized by the total number of samples observed to allow for better comparisons between the time periods. To first order, the overall CFADs of the full PISTON distribution and the time period of interest under the cirrus and widespread clouds in the convective (Fig. 4.3a-b) and stratiform (Fig. 4.3d-e) profiles look quite similar. The CFADs for ZDR shown in Fig. 4.4 also show few first order differences.

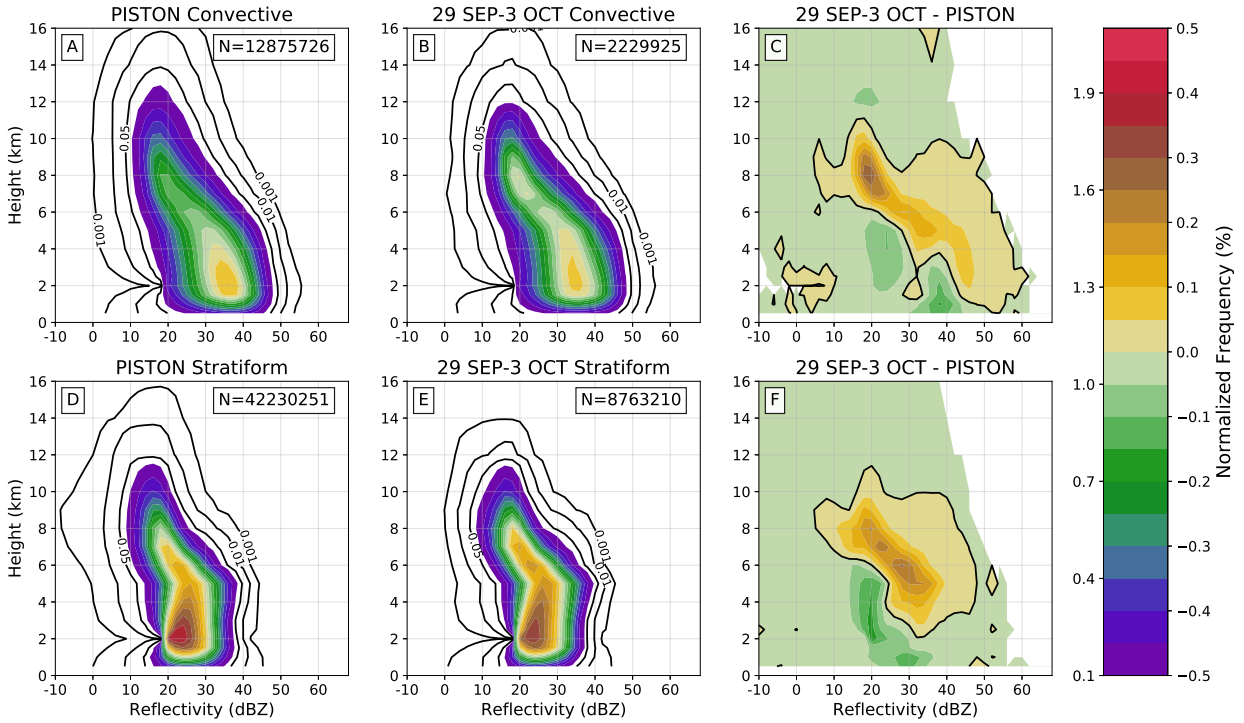

FIG. 4.3. CFADs for all points defined as convective within the range of SEA-POL during the PISTON field campaign (a) and over just the time period of interest from 29 Sep to 3 Oct (b). CFADs for stratiform defined echoes over PISTON (d) and the time period of interest (e). The CFADs are normalized by the total number of echoes observed in each category, which is shown by N, to limit differences due to sampling. The differences between the time period of interest and all of PISTON for convective echoes (c) and stratiform echoes (f). The zero line is highlighted with the black line and bins with no echoes are whited out. CFADs are binned every 1 km at 2 dBZ intervals. Total distributions use the left side of the colorbar with differences using the right side.

The distributions suggest broad similarity between the convection observed near the TC and typical convection observed during PISTON, but some differences are apparent when the subtracting the normalized CFADs as shown in Figs. 4.3-4.4c and 4.3-4.4f. In both cases, the peak height of convective and stratiform clouds are reduced with fewer reflectivity echoes reaching altitudes above 14 km. There are two potential reasons for this difference. One explanation is that the upper levels have been stabilized through radiative cooling above the cloud and radiative warming within the cloud (Duran and Molinari 2019). It is also possible that an upper-level constraint can be attributed to the dynamics of the TC, as cloud heights are constrained vertically by the layer of strong outflow from the primary TC eyewall (Houze 2010). Given that the convective profiles are observed in a range of radii from 200-700 km from Kong-rey, there is likely a combination of the two constraints at play. Even though the peak altitudes are reduced, there is an overall increase in the frequency of convective and stratiform clouds reaching 8-10 km with 20 dBZ reflectivity echoes. Corresponding to the increase in reflectivity, there is

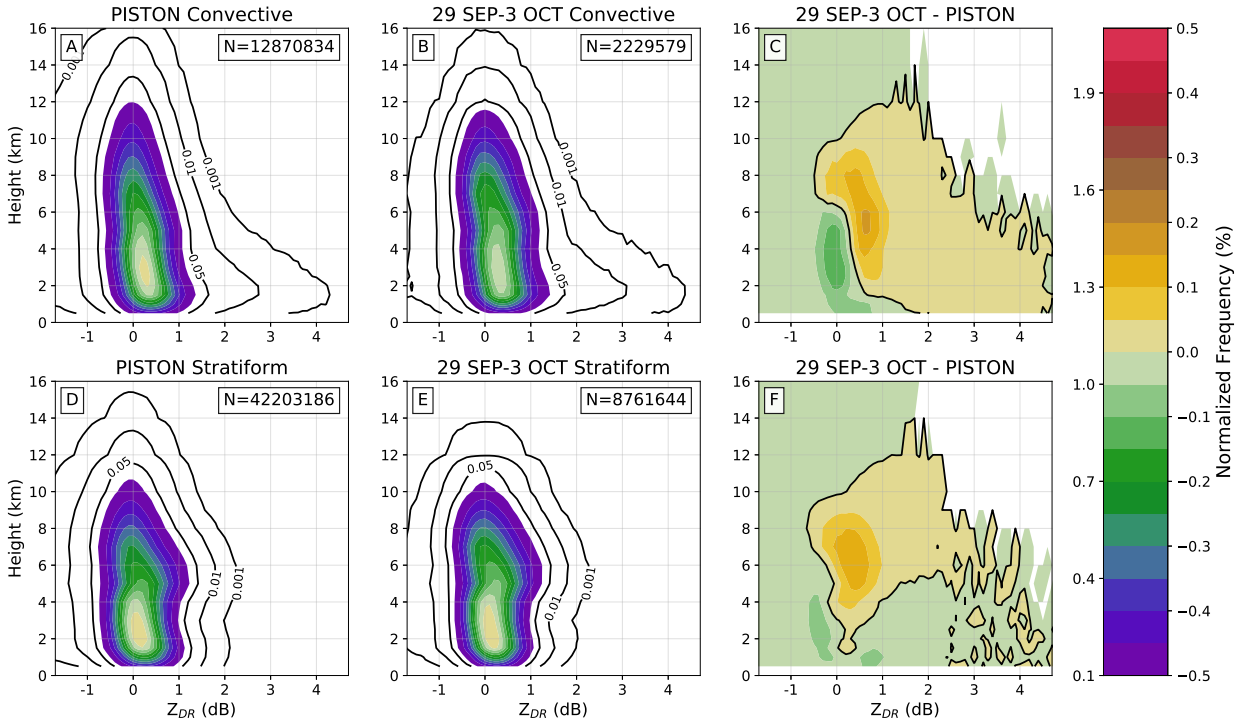

FIG. 4.4. Same as Fig. 4.3 but for ZDR.

also an increase in the ZDR values from 0.5-1.0 dB, suggesting a slight increase in the median size of the hydrometeors (Fig.4.4). There appears to be a shift in the distribution of reflectivity echoes towards larger values under the cirrus canopy around, and below, the melting level (5 km). The shift in the distribution suggests that convection was able to more consistently grow to greater heights and produce both larger, as suggested by the greater ZDR, and higher concentrations of water droplets and ice/snow crystals. The differences in strength of convection are likely not tied directly to the cirrus canopy, but suggests a more favorable environment for convection when the cirrus canopy is present.

To investigate the diurnal cycle of convection in the outer core convection, CFADs of outer rainband precipitation are analyzed in a similar manner as Fig. 4.3 but with profiles separated into day and night categories. For brevity, only the changes to the CFADs for reflectivity in convectively identified radar echoes are shown in Fig. 4.5. Consistent with Figs. 4.3-4.4, there are no major differences between the overall patterns of the normalized CFADs in Fig. 4.5 but there are some quantitative differences in the distributions. The PISTON-wide diurnal difference in convection (Fig. 4.5c) shows weak contrast overall, suggesting only a small effect of radiation on the intensity of convection. Fig. 4.5c indicates that convection during the daytime hours has a more peaked distribution at upper-levels with slightly higher reflectivity values. Interestingly, the PISTON wide day-night difference does not suggest that

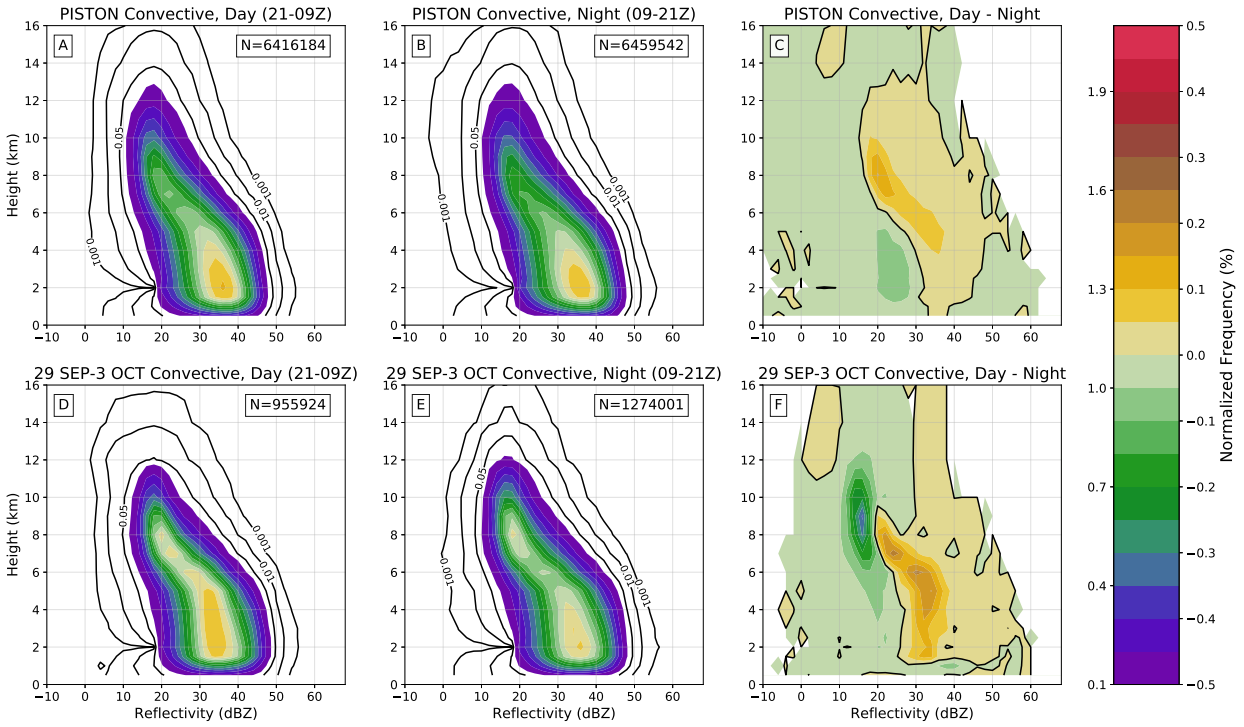

FIG. 4.5. CFADs broken up into Day (21-09 UTC) and Night (09-21 UTC) for convectively defined points only similar to Fig. 4.3. The PISTON CFAD during the Day (a), Night (b), and the difference between them are shown in (c). The CFADs for the time of interest are shown during the Day (d), at Night (e), with the difference highlighted in (f).

nocturnal convection is stronger, despite the higher relative humidity from longwave cooling normally found at night (Melhauser and Zhang 2014). Instead a slight daytime enhancement of reflectivities may suggest that the presence of diurnal warm layers, which are prevalent in clear sky low-wind regimes, may have played a larger role in enhancing convection (Bellenger et al. 2010).

During the time period of interest where the cirrus canopy of Typhoon Kong-rey is present, the differences between nighttime and daytime convection are more pronounced (Fig. 4.5f). The stronger differences in reflectivity suggests that the diurnal cycle of convection was modified in the TC environment, potentially by the cirrus canopy and upper-level clouds of various optical depths. The data is normalized by the total number of events; however, the possibility that the smaller sample size is artificially enhancing the differences cannot be completely ruled out. While the cirrus canopy is present, convection at night tended to more frequently reach altitudes of 8-12 km. During the day, convection tended to be shallower with more intense reflectivity at low-mid level altitudes between 2-6 km. This day-night difference in convection suggests that shortwave radiative heating during the day may contribute to stabilizing the upper-levels and reducing the height of the convection.

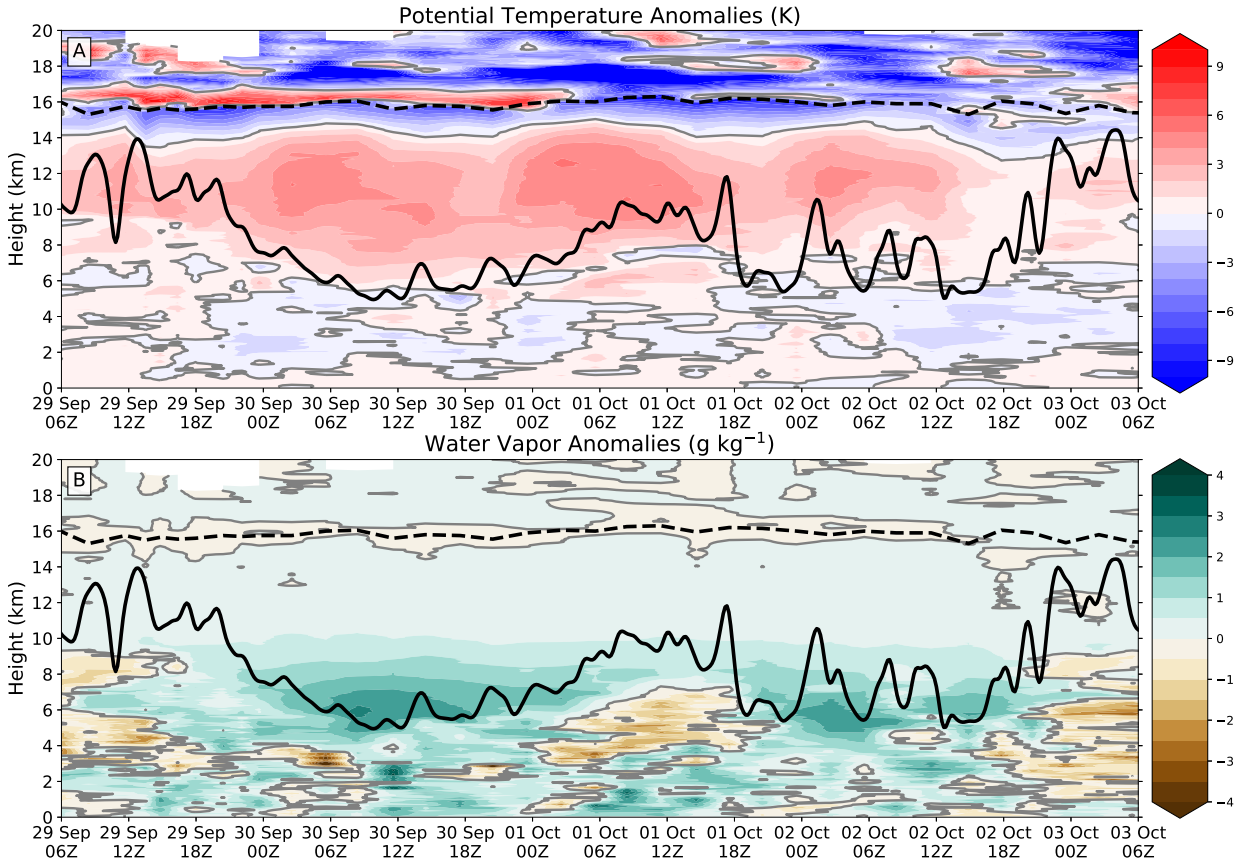

FIG. 4.6. Temporal evolution of potential temperature anomalies (a) and water vapor mixing ratio anomalies (b) from the PISTON mean profile. Missing data is whited out. The zero anomaly line is highlighted with the gray line. The black dashed line is the World Meteorological Organization (WMO) defined lapse rate defined tropopause (WMO 1957). The solid black line is a crude cloud base estimate from the maximum backscatter of HSRL that has been filtered 10 times using a 1-2-1 filter.

Next the soundings launched every three hours are analyzed to investigate the role that the thermodynamic environment may play in controlling the differences in the distribution of convective clouds. Figure 4.6 shows the evolution of the potential temperature and water vapor mixing ratio anomalies from the PISTON mean during the passage of Kong-rey. An estimate of cloud-base height from the HSRL and the derived tropopause height are provided for reference. On each day from 21 UTC-03 UTC (06L-12L) there is a pronounced warming of the upper-levels which is mostly between 8-14 km associated with direct solar heating within the cloud layers. A persistent cold anomaly remains just above the warm anomaly and just below the tropopause, which is likely due to longwave cooling at the cloud top from the strong vertical gradient in optical depth and associated flux divergence. It should be noted

that Rivoire et al. (2020) showed that cooler temperature near and above the tropopause are only partially explained by radiative cooling, concluding that other processes such as convectively generated gravity waves or a dynamic response to the vortex are playing a modest role. From 06 UTC Sep 29 to 03 UTC 1 Oct, there is a warm anomaly along the estimated tropopause height which could indicate the presence of thin cirrus clouds which causes persistent longwave warming. During the time period of interest there is enhanced water vapor shown in Fig. 4.6b which suggests a favorable environment for convection. A favorable environment for convection has been suggested to be important for outward propagating diurnal pulses in the outflow (Ditchek et al. 2019a; Knaff et al. 2019). The largest water vapor anomalies at the mid-levels around 4-8 km on 30 September corresponds to the time where the R/V *Thompson* was closest to the typhoon center. The positive water vapor mixing ratio anomalies could suggest that water vapor may have contributed to the mid-upper level temperature anomalies through absorption of shortwave radiation. The water vapor absorption of solar radiation is not strong enough to account for a majority of the potential temperature anomalies though, which are believed to be due primarily to the shortwave absorption by hydrometeors.

The absorption of solar radiation by upper-level (8-15 km) clouds results in an increase in the potential temperature measured by the soundings. Increasing the vertical gradient in potential temperature stabilizes the upper-level cloud layer during the day, which can explain the reduction in height of the convective clouds observed in the CFADs in Fig. 4.5d-f. The strong TC outflow is primarily contained within the 2-3 km below the tropopause which suggests that the differences in reflectivity between 8-12 km can be largely attributed to radiative stabilization. In addition to stabilizing the upper-levels, heating of the upper levels can affect the convective available potential energy (CAPE) of the environment. The warming increases the vertical gradient of potential temperature which stabilizes the upper-levels. Figure 4.7 shows the distributions of CAPE, the convective inhibition (CIN), and the equilibrium level where parcels become neutrally buoyant. The CAPE and CIN are calculated by assuming irreversible pseudoadiabatic ascent of parcels with the mean thermodynamic conditions of the lowest 50 hPa of the atmosphere. Relative to the distributions during the entire PISTON campaign, there are no statistically significant differences in any of the variables during the time period of interest. The cumulative distribution function (CDF) of the normalized events suggests slightly larger CAPE values and lower CIN, but the equilibrium level was consistently on the low end of the pressure level. The distribution of CAPE is quite variable over the period, with on average lower CAPE values around 2070 J kg^{-1} during the day compared to an average of 2210 J kg^{-1} at night (Fig. 4.7d). Local

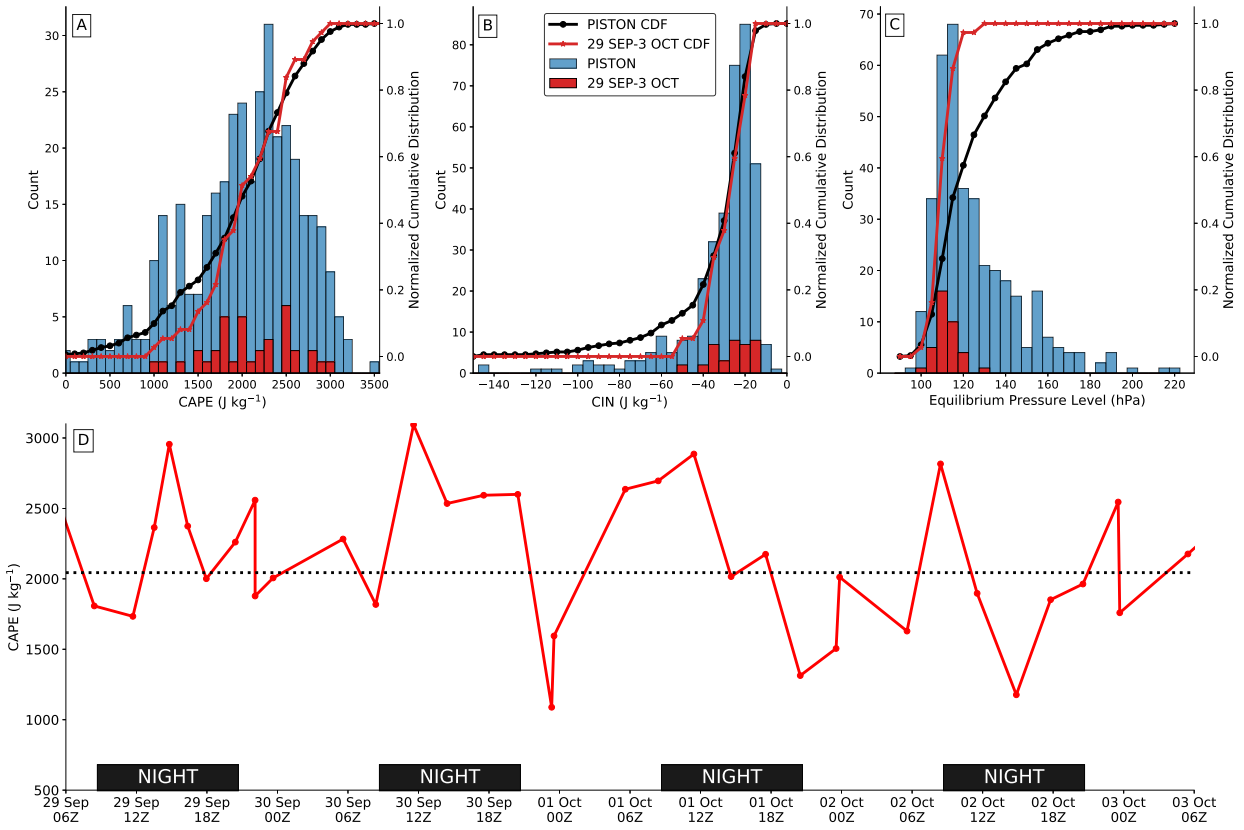

FIG. 4.7. The distributions of convective available potential energy (a), convective inhibition (b), and equilibrium pressure level (c) with bins of 100 J kg^{-1}, 5 J kg^{-1}, and 5 hPa respectively. The distributions are shown for the entire PISTON field campaign (blue) and for the time period of interest during Typhoon Kong-rey (red). The black and red lines are the cumulative distribution functions (CDF) for each of the variables for the whole PISTON distribution and the distribution during the time frame of interest. The temporal evolution of CAPE is shown in (d) with nighttime noted. The black dashed line is the mean CAPE from PISTON.

increases in CAPE at night were also found in Tang and Zhang (2016). The largest values of CAPE were observed at night over each 24 hour period up to 3000 J kg^{-1}. The variability due to radiation is smaller compared to that of the rapid consumption of CAPE by convection and subsequent regeneration. The nocturnal decline in CAPE due to consumption by convection is evident at 09 UTC-15 UTC 2 October where there is a shift in the peak of the distribution of brightness temperatures from 245 K to 215 K (4.2a). The observations suggest that the overall thermodynamics of the environment were not drastically different with the presence of the cirrus canopy or upper-level cloud layers but the environment was overall more favorable for convection.

To summarize, this section has documented a cirrus canopy extending over the ship for multiple days with a variety of observations being collected underneath the upper-level cloud layers. In the rainbands of Typhoon Kong-rey, the convective and stratiform cloud distributions were different compared to the total distributions during PISTON, with higher frequencies of ice phase clouds but overall shallower echo tops. The diurnal cycle of convection was more pronounced due to the strong shortwave absorption and stabilization of the clouds, which caused daytime convection to be shallower. It should be noted that in comparing the areal observations from SEA-POL and the semi-Lagrangian soundings, the assumption is made that the soundings provide a representative thermodynamic profile for the given area. The validity of this assumption is difficult to address because although the R/V *Thomas G. Thompson* is not moving, the center of Typhoon Kong-rey is continuously changing which causes the observations to vary in both storm relative quadrants and radii with time. The impact of the cirrus canopy and upper-level clouds on the vertical structure of convection during the diurnal cycle cannot be quantified directly in the observations or through radiative transfer as the depth and thickness of the cirrus layer is unknown.

4.4 Diurnal Pulses in the Cirrus Canopy

In the previous section the evolution of convective and stratiform clouds under the cirrus canopy is documented, including their diurnal variability. The area of the cirrus canopy itself has also been shown to have a diurnal cycle (Wu and Ruan 2016). Dunion et al. (2014) found that outward propagating cold rings in the brightness temperatures are a consistent feature in mature TCs in the Atlantic and a climatology of Atlantic TCs by Ditchek et al. (2019a) further demonstrated the commonality of these diurnal pulses in addition to documenting the presence of outward propagating warm rings. The diurnal cycle of rainband convection therefore may be complicated by the tropical cyclone secondary circulation and the presence of diurnal pulses in the outflow layer (Dunion et al. 2014, 2019). Fig 4.2b-c shows 6 hour differences in the IR brightness temperatures centered on Typhoon Kong-rey on two separate days corresponding to the red and blue horizontal lines in Fig. 4.2a. At those two instances, there appears to be an outward propagating ring of cold brightness temperatures similar to those shown in Dunion et al. (2014) for major hurricanes in the Atlantic basin. Radially inward there is a region of warming brightness temperatures. These two “cold rings" that appear in Typhoon Kong-rey are not on the proposed “Dunion Clock" as they occur $\sim$ 6 hours prior to the earliest expected time given in Dunion et al. (2014). The “cold rings" in Typhoon Kong-rey appear to be more asymmetric than those

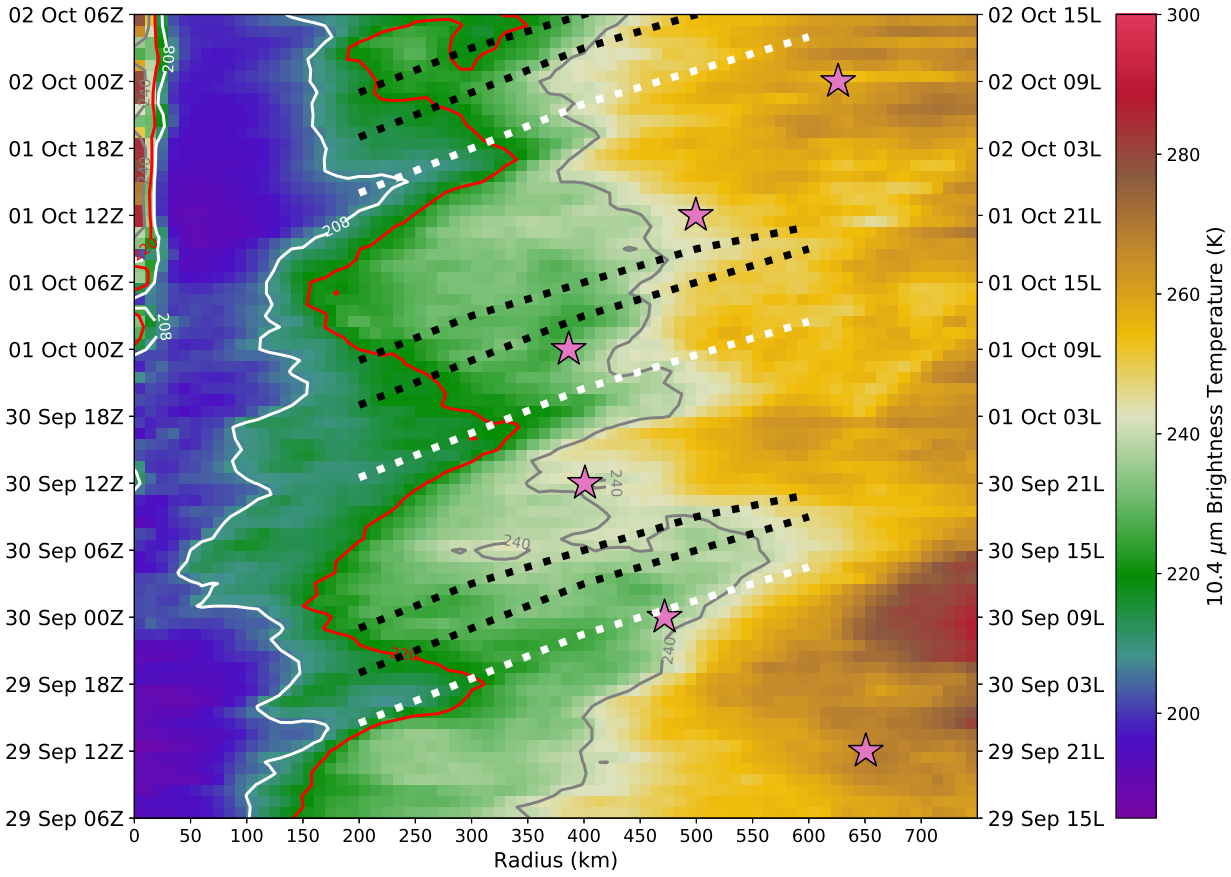

FIG. 4.8. Evolution of TC centered axisymmetric mean infrared brightness temperatures from Himawari-8 averaged over 10 km bins every hour. Stars indicate the location of the R/V *Thompson* at 12 hour intervals. The black dotted lines are the estimated time and radius of the diurnal pulses from Dunion et al. (2014). The white dotted lines highlight the observed diurnal pulses. The thin white and gray lines are the 208 K and 240 K brightness temperatures contours for comparison with Wu and Ruan (2016). The 220 K brightness temperature contour is shown in red. Data is shown hourly using linearly interpolated TC track data from JTWC. The right ordinate is in local time with the left ordinate being in UTC.

documented in previous studies, which is likely due to the presence of moderate northeasterly deep layer shear. The deep layer shear was low in all of the cases examined in Ditchek et al. (2019a) and is believed to be a requirement for robust diurnal oscillations (Knaff et al. 2019). Despite some differences in timing and structure of the cold rings in Typhoon Kong-rey compared to those previously reported, the overall appearance in satellite imagery is similar to past cases and suggests that the physical mechanisms that produce them may also be similar.

Although the 6-hour differencing in brightness temperature provides a quick way to visualize the spatial structure of the cooling pulses in the outflow layer, a time-radius evolution of mean brightness

temperatures is able to show the consistency and propagation of the pulses. Figure 4.8 shows the evolution of axisymmetric mean brightness temperatures from Himawari-8 centered on Typhoon Kong-rey with black lines indicating the expected timing and position based on the “Dunion Clock". The white and gray lines highlight the 208 K and 240 K mean brightness temperature which was shown to have a pronounced diurnal cycle in the blended IR imagery in Wu and Ruan (2016). In Fig. 4.8, the presence of cold clouds <208 K is consistently found near the TC center, and as Kong-rey rapidly intensifies, the coldest clouds (<208 K) shift radially outward with the eye becoming well established after 00 UTC 1 October. The radial extent of the cirrus canopy conversely contracts with time as Typhoon Kong-rey rapidly intensifies, in agreement with past studies showing the inverse relationship between areal extent of the cirrus canopy and TC intensity (Browner et al. 1977; Kossin 2002). The areal extent of the cirrus canopy using the 240 K contour did not show a consistent diurnal cycle and did not exhibit the expected late afternoon maximum in contrast to previous studies (Steranka et al. 1977; Browner et al. 1977; Kossin 2002; Wu and Ruan 2016). Over the three days shown, there are three distinct times where regions of cold brightness temperatures propagate radially outwards from the TC center as evident by the 215 K shaded contour. The relative location of the R/V *Thomas G. Thompson* relative to the typhoon is shown to highlight that the observations collected from the ship sampled, at different storm relative radii, at most two outward propagating cold rings.

In Fig. 4.8, the three distinct times where clouds colder than 220 K expand radially outward all occur roughly 24 hours apart, which suggests that the diurnal cycle of radiation may be important. The 220 K brightness temperature contour in the azimuthal mean best highlights the diurnal oscillations in the upper-level clouds but is quantitatively not a significant value because of the tropical cyclone asymmetries. Although the cooling pulses all occur on a diurnal cycle, the representation in the axisymmetric brightness temperatures are slightly different. The first and last diurnal pulses appear to start in the inner core of Typhoon Kong-rey around 21L and propagate outwards at colder brightness temperatures <210 K which slowly warms with time as the leading cloud edge subsides. The second pulse on 30 September does not appear initially to be coupled with the <210 K brightness temperatures in the inner core region but instead appears as a continuous outward expansion of cold clouds. The different representation of the pulses in the axisymmetric imagery is to some degree a byproduct of asymmetry smoothing due to vertical wind shear and structural changes as Kong-rey rapidly intensified. It will be shown later that the primary rainband and convective bands were all located downshear during the second outward propagating cold ring.

The three cold rings in Fig. 4.8 vary in how far they propagate and their estimated propagation speeds. The propagation speed, estimated by comparing the expansion of the 220 K contour, of the first pulse is qualitatively slower than the third pulse but both are within the estimated propagation speed of those presented in Dunion et al. (2014). The propagation speeds range between 5-7 m s^{-1} which is on the slower side compared to the 5-10 m s^{-1} noted by Dunion et al. (2014) and the 8-14 m s^{-1} shown in Ditchek et al. (2019a). The different propagation speeds between the cooling pulses of Typhoon Kong-rey may be explained by the different intensities of the storm at the two times. More intense tropical cyclones have a stronger secondary circulation that would support faster transport of ice away from the storm center in the outflow layer (Pendergrass and Willoughby 2009). The third cold ring also propagated further away from the center at colder brightness temperatures compared to the first, which similarly could be explained by the strength of the outflow given a similar dissipation rate. The upper-level moisture could also play a role in modifying the pulses, although the environment shown in Fig. 4.6 did not show considerable variability from the ship's position (Knaff et al. 2019). The second cold ring has a harder to define propagation speed and propagation distance which is sensitive to the chosen brightness temperature thresholds. At the 220 K contour, the second pulse reaches the furthest radius and passes directly overhead of the R/V *Thompson*.

It is uncertain as to how much of the brightness temperature signal of the cooling pulses are driven by ice being advected by inner core convection or ice produced by deep convective clouds in the outer core. Wu and Ruan (2016) discussed the possibility that diurnal pulses correspond to expansion and contraction of the cirrus canopy. The 220 K brightness temperature contour in Fig. 4.8 shows a clear radial minima during the time of peak solar heating around local noon which expands radially in the afternoon and into the overnight hours. The local minima further suggest that convective cloud heights observed by SEA-POL were reduced due to shortwave heating. The 208 K contour, which corresponds to deep convective clouds in Wu and Ruan (2016), does show a peak in area from 21-03 L which corresponds to the outward propagating cold rings. This suggests that deep convection in the eyewall region of Typhoon Kong-rey is peaking in the late evening to early morning time period consistent with previous observations (e.g. Gray and Jacobson 1977). The 240 K contour, which could be used to identify the radial extent of cold clouds, expanded with the pulse like features but was not directly connected to the cooling pulses and contracted to smaller radii with time as Kong-rey intensifies. The difference between the area of 208 K to 240 K brightness temperature did not exhibit any strong diurnal variation.

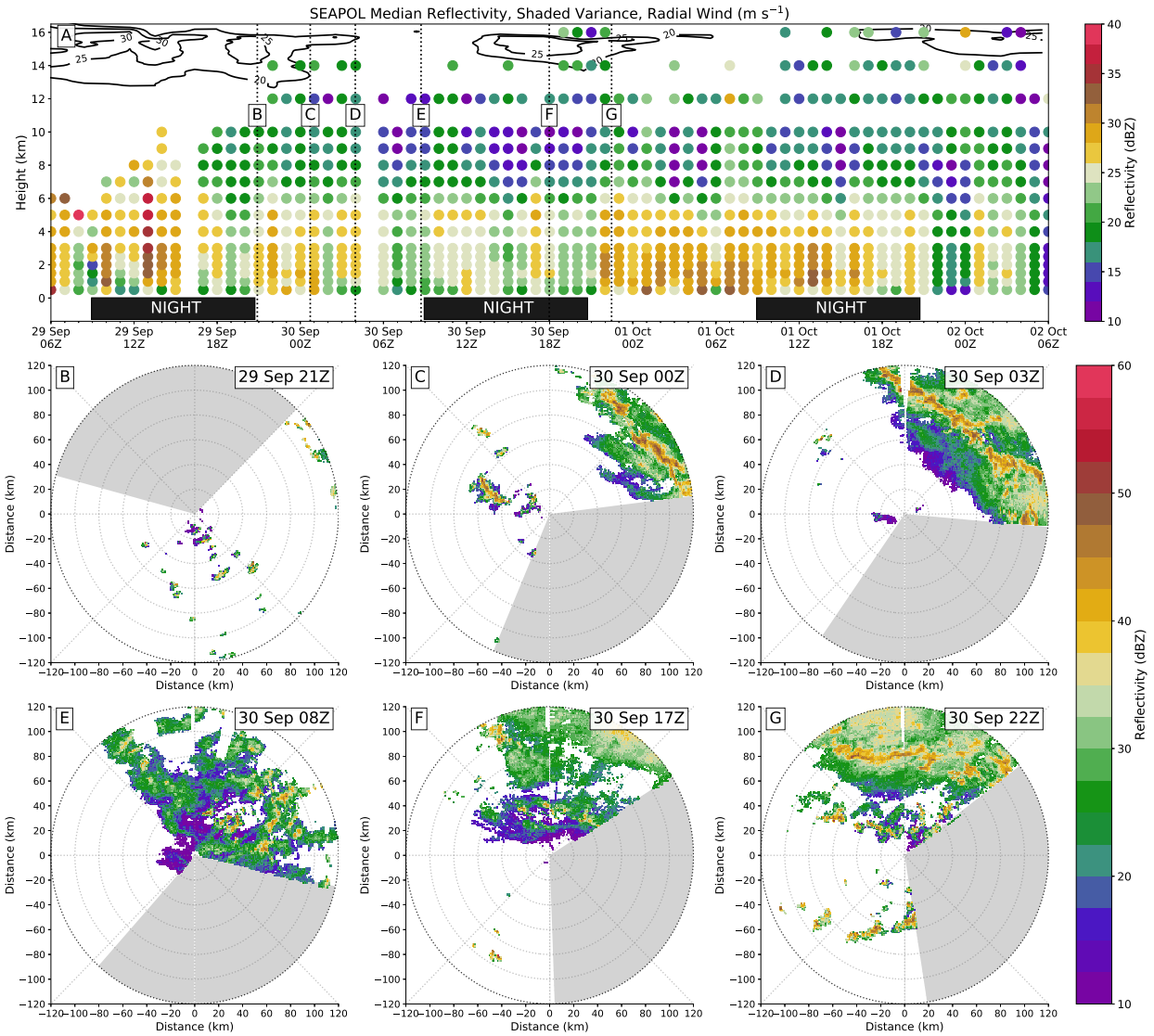

FIG. 4.9. Colored circles in (a) are the evolution of the hourly median reflectivity profile from gridded SEA-POL data. Contoured in black is the tropical cyclone relative radial winds derived from the thermodynamic profiles exceeding 20 m s^{-1}. Vertical dotted lines indicate the times of the corresponding 2-km altitude horizontal cross sections shown in (b)-(h). The gray shaded region is where SEA-POL was not transmitting and collecting observations which changes with ship heading. Times where no solar radiation is affecting the cloud distributions is denoted for reference. Note that the evolution of the median reflectivity and the cross sections use slightly different colorbars.

To better understand the structure of these propagating diurnal pulses, the observations underneath the cirrus canopy from the R/V *Thomas G. Thompson* are utilized. Figure 4.9 shows the evolution of the median reflectivity profile every hour measured by SEA-POL with individual volume scans gridded to 2 km in altitude at specific times shown. In addition, the radial wind relative to the typhoon center is plotted exceeding 20 m s^{-1} derived from the soundings. There are two outward propagating

cold rings observed from satellite that approach the location of the ship but at different storm relative distances. The edge of the first cooling pulse reaches the ship around 20-22 UTC Sep 29 with the coldest clouds overhead being around 03 UTC 30 September (Fig. 4.8). During the time of the first pulse there was an increase in the outflow near 15 km that is associated with the outward propagating cold ring. It should be noted that the strong outflow from 06-12 UTC Sep 29 can be attributed to the background easterlies and not from the circulation of Typhoon Kong-rey. Associated with the first propagating ring there is an increase in the height of precipitating clouds as rainbands moved into range of SEA-POL (Fig. 4.9b-d). Following the first pulse and associated outflow jet, there was a lull in the radial outflow and both a decrease in height and median reflectivity of the observed clouds. The decrease in convection was associated with an increase in stratiform precipitation as shown by the 2-km horizontal cross section at 08 UTC on 30 September in Fig. 4.9e. Although Dunion et al. (2019) showed that convection associated with diurnal pulses decreases in height as it moves radially outward, the height changes with radius using SEA-POL cannot be reliably evaluated.

The leading edge of the second propagating cold ring reaches the ship between 16-17 UTC 30 September with the coldest cloud tops overhead the ship around 19 UTC 30 September (Fig. 4.8). Similar to the first pulse, Fig. 4.9a shows that there is another outflow jet measured by the soundings followed by an increase in the height of clouds with observed reflectivity. The heights of the measured reflectivity reaches the level of strong radial outflow which suggests that the convection is strong enough to penetrate the stable layer and likely contributes to the maintenance of the cold ring signature from satellites. There is also an increase in the median reflectivity values throughout the column corresponding to the times seen in the IR imagery with a small time lag. The median reflectivity at low levels increases after the elevated echo tops because of the moderate extent of stratiform precipitation in the SEA-POL domain (Fig 4.9f). Following the increased outflow and rainband storm heights, there is a reduction of both the height and outflow magnitude in the hours following the second cooling pulse, which is similar to the previous cold ring and evident in the cross sections at 2-km at 22 UTC (Fig 4.9g. After the second propagating cold ring there is a continuous period of median reflectivity values between 25-30 dBZ observed at lower levels due in part to a change in the number of observed convective cells by SEA-POL.

Figure 4.9a shows that the outward propagating cold rings are coupled with an outflow jet and are followed by an increase in the height of precipitating clouds and an increase in the median reflectivity

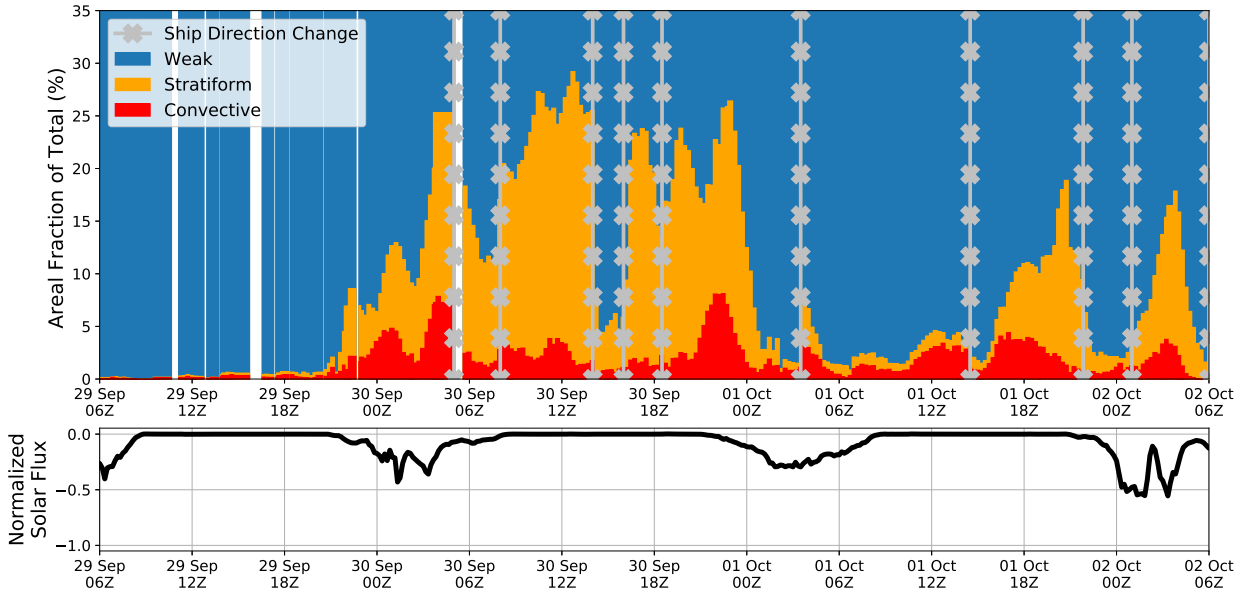

FIG. 4.10. Temporal evolution of the areal coverage of convective and stratiform precipitation during the time period of interest observed by SEA-POL. Gray vertical lines indicate substantial turns in the motion of the R/V *Thompson* where previously observed radar echoes were obscured. The downward solar flux is shown normalized by the peak observed flux value during PISTON.

as convective squalls moved into range of SEA-POL. This would suggest that the diurnal pulses observed here are convectively coupled. To further demonstrate the coupling, the evolution of the areal fraction of convective and stratiform classified points is shown in Fig 4.10. Changes in ship motion, that have been subjectively defined, are labeled to explain discontinuities from one time to the next. The downward solar flux normalized by the maximum observed during PISTON is shown to help orient the reader to the solar cycle. The first diurnal pulse that moves over the ship around 20-22 UTC Sep 29 corresponds to an increase in the observed areal extent of convection, lagged by several hours, which reaches a relative peaks in coverage around 05 UTC 30 September. The amount of stratiform clouds also grew in areal extent following the pulses, suggesting a weakening of the convective band which is consistent with IR satellite imagery. Chapter 3 showed in an idealized model that there is an amplification of the heating/cooling profile of stratiform precipitation during the nighttime without strong shortwave radiation. The second pulse, which reached the ship between 16-17 UTC 30 September, is followed by an increase in the areal extent of observed convection ~6 hours later, similar to the first diurnal pulse. Around 8 hours after the second pulse, SEA-POL observed fewer organized convective cells that were more scattered as Kong-rey moved away from the R/V *Thomas G.Thompson.* Following the second pulse between 06-18 UTC 1 October is when dry air was observed in the soundings shown

in Fig. 4.6, which might help to explain the shallower echo tops and reduced convective area. Observations from SEA-POL support the idea that cold rings seen in IR imagery that propagate radially outwards are tied to convection but offset as winds in the outflow exceed the propagation of convective storms.

Fortunately, the second diurnal pulse was sampled multiple times by passive microwave sensors, allowing for a complementary analysis to the infrared and radar observations. The first and third diurnal pulses did not have enough microwave passes for a complete analysis. Figure 4.11 shows five passes with good spatial coverage centered on Typhoon Kong-rey's position on 30 September. The times shown are not evenly spaced and the satellites do not all have the same spatial resolution. On 06 UTC 30 September (Fig. 4.11a), there is a primary rainband wrapping into the center of the typhoon with a smaller area of deep convection at the center. The band is primarily located within 100 km of the storm center and has cold 91.6 GhZ brightness temperatures, suggesting a large amount of scattering by ice and snow. By 09 UTC, the primary rainband has widened and become more symmetric around the center, and has even colder brightness temperatures. At 09 UTC the primary rainband has moved radially outward and is now located just outside 100 km from the storm center. The next overpass by AMSR2 occurs 7 hours later at 16 UTC, providing a more detailed look at Kong-rey because of its higher spatial resolution (Fig. 4.11c). Typhoon Kong-rey at 16 UTC has continued to intensify with convective ice signatures forming an eyewall within 100 km. The primary rainband has continued to move radially outward to >200 km away from the center. The structure of the rainband has become more disorganized at the next overpass at 19 UTC with discontinuous areas of deep convective ice signatures (Fig. 4.11d). The edge of the convective portion of the rainband has become harder to identify as it moves radially outwards to ∼250 km. At this time there also appears to be a new line of thunderstorms forming around 150 km away from the center as a new primary rainband begins to form. The last overpass by SSMIS shown at 22 UTC, shows that the radially outward propagating convective signature has been reduced in the azimuthal direction. After the convection associated with the primary rainband showed signs of weakening, it is unclear if there was a reorganization of the band or if it began to propagate azimuthally outside of the satellite's field of view. The collocation of the microwave imagery with the infrared imagery suggests that the outward propagating cold rings were convectively coupled and originated from the primary rainband which moved radially outwards.

This section has shown that within the cirrus canopy of Typhoon Kong-rey there were multiple outward propagating cold rings occurring on a diurnal timeline. Multiple perspectives were analyzed

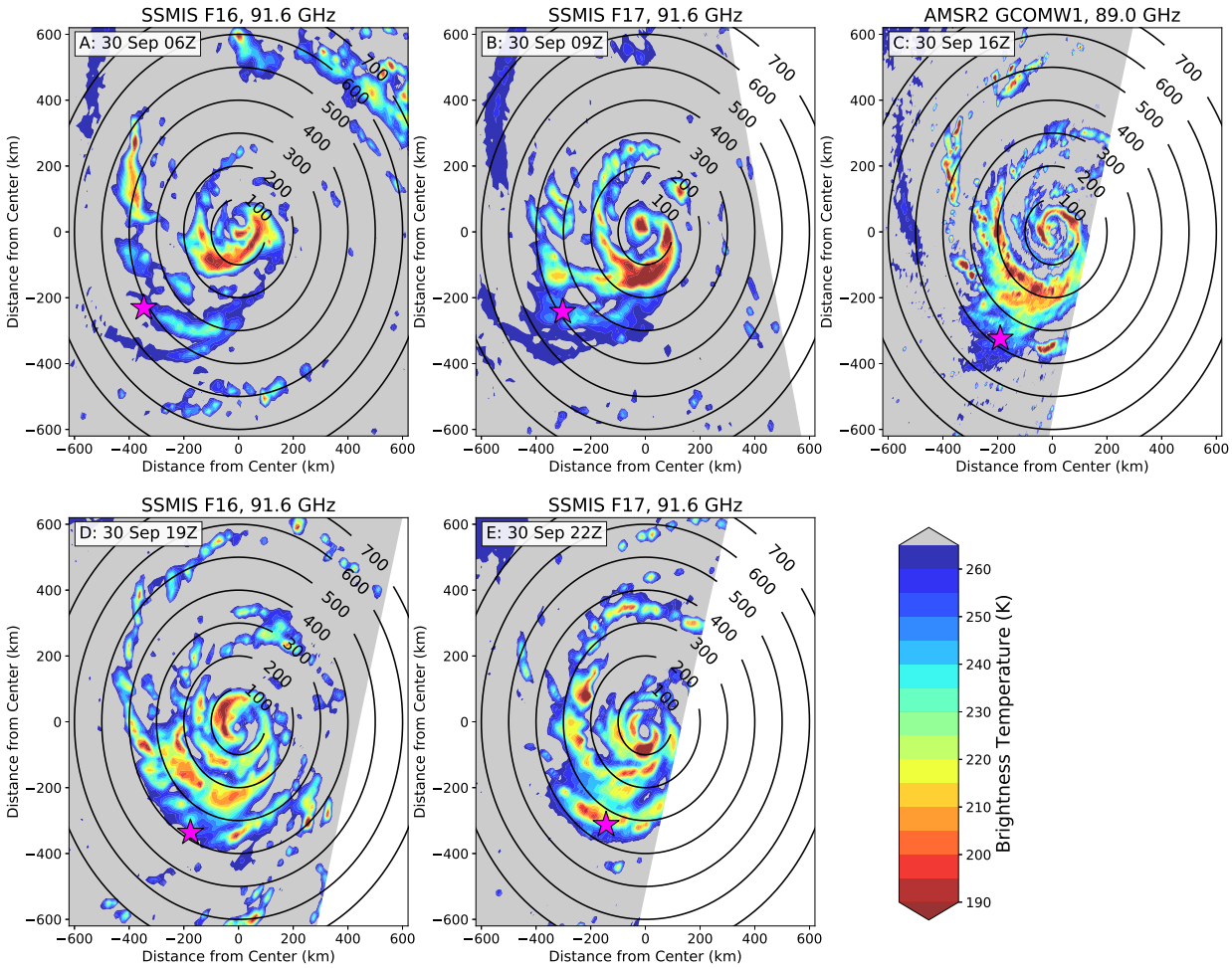

FIG. 4.11. Sequence of passive microwave overpasses during the second diurnal pulse from SSMIS and AMSR2 centered over Typhoon Kong-rey. The times shown are all on 30 Sep at 06 (a), 09 (b), 16 (c), 19 (d), and 22 UTC (e). The SSMIS imagery shown corresponds to the 91.655 GHz band while the AMSR2 imagery is from the 89.0 GHz band. Brightness temperatures warmer than 265 K are gray and locations outside of the field of view are white. The pink stars indicate the general location of the R/V *Thompson* during the time of the overpass. Range rings are plotted every 100 km extending out to 700 km.

using satellites and ship based instruments to provide an in depth look at the cold rings. The cold rings were evident in the IR imagery but were manifested in the typhoon dynamics as an outflow jet observed by upper-air soundings. Associated with the cold IR clouds, there was an increase in convection observed from the R/V *Thomas G. Thompson* with a lag time of roughly six hours suggesting that these features are in fact convectively coupled. Convective heights sometimes penetrated the outflow layer suggesting that rainbands may continually contribute to the diurnal pulse signatures in the IR. Although these cold rings did not occur at the typical times proposed by Dunion et al. (2014), the characterizing features are similar to what was proposed in the modeling study of Dunion et al. (2019).

Whether these diurnal pulses are the same phenomena just modulated by Kong-rey's structure and environment, or they are representative of a different physical mechanism is unclear from the limited observations available.

4.5 Summary and Conclusions

In this chapter, novel observations from the Propagation of Intraseasonal Tropical Oscillations field campaign have explored the diurnal variability of convection under a distribution of cold upper-level clouds. Observations over a three day span were collected under the cirrus canopy of Typhoon Kong-rey (2018) and compared to the two months of observations from PISTON. Satellite observations show evidence of diurnal oscillations in the brightness temperature of upper-level clouds. The case study of Typhoon Kong-rey has provided unique observations of the diurnal variability of rainband convection and diurnal oscillations in the outflow layer for future comparison with and improvement of numerical weather prediction models.

Observations from PISTON provide evidence that the convective and stratiform clouds under the cirrus canopy of Typhoon Kong-rey were stronger compared to the overall distribution from PISTON. The peak altitude of convective and stratiform clouds, however, was reduced in the near TC environment and believed to be due to the increased stability from the outflow layer (Houze 2010). The elevated moisture in the environment of Typhoon Kong-rey may be responsible for the increased median size of snow and ice found at upper levels in both convective and stratiform precipitating clouds. On diurnal timescales, a temperature response to shortwave heating was observed in the thermodynamic soundings and in rainband convection with reduced concentrations of ice species aloft. These observations suggest that the stabilizing effect of shortwave radiation in the moat region and in upper-levels of the rainbands shown in the modeling studies of Tang et al. (2017) and in Chapter 3 may be at work. The Gray and Jacobson (1977) mechanism for explaining the diurnal cycle of oceanic convection cannot be assessed due to the continuous changes in boundary layer winds associated with nearby convective rainbands and the increasing radial winds during Kong-rey's intensification.

Observations of Typhoon Kong-rey have revealed diurnal oscillations in the brightness temperature that have characteristics similar to previously reported diurnal pulses (Dunion et al. 2019; Ditchek et al. 2019a; Knaff et al. 2019). The cooling pulses in Typhoon Kong-rey were not on the "Dunion" clock, similar to the one noted by Ditchek et al. (2019b) but three such oscillations occurred in the outflow of Typhoon Kong-rey suggesting that the feature is diurnally driven and recurrent. The R/V *Thomas*

G. Thompson was in range to observe the convective evolution of rainbands associated with two of the diurnal pulses found in Typhoon Kong-Rey during its rapid intensification. The cooling pulses were associated with strong outflow jets consistent with the model shown in Dunion et al. (2019) and increased convection afterwards suggesting a lagged coupling with rainband convection. Observations from SEA-POL and the thermodynamic soundings showed convective reflectivity echoes penetrating the outflow layer suggesting that the cooling pulses at upper levels are coupled with, and likely maintained by, rainband convection and are not driven solely by inner-core convective processes of Typhoon Kong-rey. The maintenance of the cooling pulses by strong rainband convection is further suggested by the favorable environment for deep convection shown by previous studies (Dunion et al. 2019; Knaff et al. 2019; Ditchek et al. 2019a).

One proposed mechanism for the cooling pulses in mature TCs is through the excitation and coupling of gravity waves to convection in the outer core (Dunion et al. 2019; Ditchek et al. 2019a). The gravity waves have been tied to the diurnal cycle of convection which has been shown to peak in the early morning; however, if this peak in convection was modified through asymmetric tropical cyclone dynamics or the presence of a cirrus canopy, the timing of cooling pulses could also be modified (Hong et al. 2006a). It is unclear why the propagating cold rings in the brightness temperatures of Typhoon Kong-rey did not occur on the “Dunion" clock, although the diurnal cycle of convection in oceanic tropical environments can be variable. Variations in diurnal TC convective activity have been shown to have basin differences, for example lightning associated with deep convection in the TC inner core showed a broader diurnal peak in the East Pacific (23-08 LST) compared to the Atlantic (23-02 LST) (Stevenson et al. 2016). It is therefore speculated that similar, if not the same, mechanisms are controlling the diurnal oscillations seen in Kong-Rey to those seen in the Atlantic, but further research is required to confirm this hypothesis.

The diurnal oscillations in the brightness temperature imagery of Typhoon Kong-rey occurred while the tropical cyclone was rapidly intensifying suggesting that these oscillations can occur at all stages of development consistent with past studies (Knaff et al. 2019; Ditchek et al. 2019a). The upper-level oscillations show variability in propagation speed which could be directly tied to the strength of the secondary circulation. The microwave imagery suggests that the convective evolution of these rings can be asymmetric, aligning with the vertical wind shear vector, which when azimuthally averaged could explain variations in the intensity of cooling pulses. A radial contraction of the secondary circulation with increased subsidence closer to the center, could also lead to changes in the propagation

and magnitude of IR temperatures which has been thought to explain the inverse relationship between cirrus canopy extent and tropical cyclone intensity (Browner et al. 1977). Understanding the variability of these diurnal oscillations both spatially and temporally due to factors such as vertical wind shear and storm motion will be necessary to improve short term quantitative precipitation forecasts and will be a topic for future work.

The observations analyzed herein were collected in a continuously evolving environment and have some observational biases from the position of the R/V *Thompson*. Relative to Typhoon Kong-rey, the observations were collected at different storm relative locations which is important for considering diurnal pulses, which are expected at different storm relative radii at specific times. The changing storm relative position is one complication to this work. Despite some expected slight inconsistencies between the different instrumentation and limited areal coverage from SEA-POL, the Lagrangian balloon-borne thermodynamic profiles, and the ship-based fluxes, the collected data provides a coherent narrative. These are the first known surface-based oceanic observations of diurnal oscillations in the upper-level clouds of a tropical cyclone, providing further evidence that radiation affects the distribution of convective and stratiform clouds in the rainbands during intensification. Further case studies and observations are warranted to improve and expand upon the results of this study.

CHAPTER 5

SIMULATING THE DIURNAL VARIABILITY OF TYPHOON KONG-REY'S (2018) RAINBANDS

5.1 INTRODUCTION

It is only within the last decade that dynamical hurricane forecast models have improved to the point where they have influence on intensity forecasts from the National Hurricane Center (NHC) and Joint Typhoon Warning Center (JTWC) (DeMaria et al. 2014; Cangialosi et al. 2020). Dynamic forecast models such as the Hurricane Weather Research and Forecasting Model (HWRF) have shown improvement in forecasting intensity change. HWRF has been the most skillful model over the last 5 years at 48 hour intensity forecasts, which is the critical watch issuance lead time (Cangialosi et al. 2020). Models such as HWRF are able to explicitly model convection in the hurricane and the mesoscale processes that lead to intensification. It is critical to forecasters that these models are able to simulate not just the track and intensity, but also the rainband structure which can affect both the size and intensity of the tropical cyclones (TCs).

The inner-core rainbands of a tropical cyclone plays a critical role in both the intensity and radial extent of the winds. Wang (2009) used idealized simulations of hurricanes to determine how spiral rainbands affect the the structure and intensity of the storms. It was shown that when diabatic heating was added outside the moat region to approximate the rainbands, hydrostatic adjustment occurred which reduced the radial gradient in surface pressure and therefore the tangential wind maximums. Wang (2009) shows that convective heating leads to a broader tangential wind field but weaker wind speed maximums, while cooling in the rainband region leads to a stronger and more compact primary circulation. Overall, the bulk amount of convective heating in the rainbands is largely lost to gravity wave radiation away from the storm center, but can have a larger impact on the circulation where the inertial stability is high. Factors controlling the magnitude and extent of diabatic heating in the rainbands, such as the thermodynamic environment, cloud microphysics, and radiation, are all important to consider when forecasting TC size and intensity. Fovell et al. (2016) showed that the interactions between various cloud microphysics and radiation schemes alone had a large impact on the size, intensity, structure, anvil clouds, and storm motion which motivates more work into complex radiation-microphysics interactions. It should be noted that Fovell et al. (2016) largely discussed the longwave cloud radiative effects leaving the shortwave radiative effects a topic for future work.

The existence of diurnal oscillations in the brightness temperatures and enhanced diurnal variability associated with the rainband convection of Typhoon Kong-rey has been documented in Chapter 4. The diurnal pulses in the outflow layer had similar characteristics to those described in previous studies but were out of phase (Dunion et al. 2014, 2019). The unique set of observations collected during PISTON allows for a novel look at the diurnal variability of TC rainbands in a tropical oceanic atmosphere. The examination of Typhoon Kong-rey is further motivated because intensity forecasts from JTWC had large errors on average throughout the storm's lifecycle. Figure 5.1 shows the average intensity forecast errors from JTWC for each West Pacific TC in 2018. Kong-rey had the largest intensity errors over the first 36 hours of any storm in 2018 and large errors overall because the rapid intensification (RI) of the storm was under predicted. In order to improve forecasts of tropical cyclone intensity change, numerical weather prediction models and the physical schemes therein need to be improved. Because radiation is fundamental to the diurnal cycle and has been shown to influence hurricane structure in idealized models (Bu et al. 2014; Fovell et al. 2016; Trabing et al. 2019), it is important to understand how well forecast models capture radiative impacts on hurricanes and the sensitivity that the microphysics may play in changing the vortex.

The goal of this chapter is to provide insight into how sensitive forecasts of Typhoon Kong-rey are to the microphysics and radiation schemes that have been utilized by previous studies. It is unclear how well radiation and microphysics schemes simulate diurnal variability within tropical cyclone rainbands and whether they are capable of resolving diurnal pulses. By comparing high-resolution simulations of Typhoon Kong-rey with detailed observations from the PISTON field campaign, understanding of the interactions between tropical cyclones, clouds, and radiation may be enhanced in the hopes that it will lead to improved forecasts of both tropical cyclone size and intensity. The sensitivities to the microphysics and radiation schemes will also provide important guidance for future modeling studies and provide context for past experiments.

5.2 Experimental Design

5.2.1 Typhoon Kong-rey Simulations

The Weather Research and Forecasting (WRF; Skamarock et al. 2008) model version 3.9 is employed to simulate Typhoon Kong-rey in four experiments. The initial conditions of each experiment is the same using observations from the Global Data Assimilation System (GDAS) at .25° by .25° global resolution. GDAS is used to initialize the experiments here and constrain the boundaries of the outermost

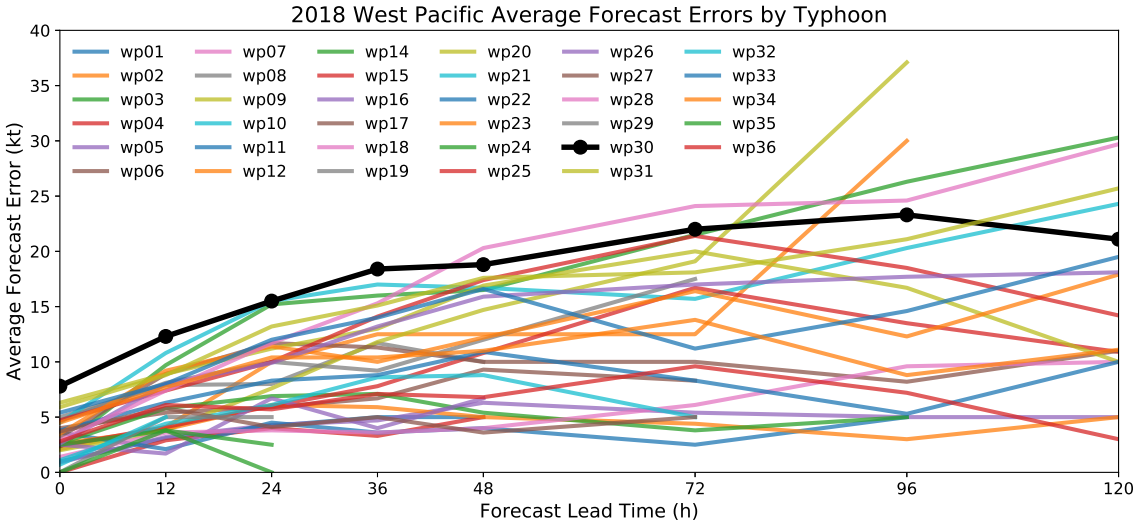

FIG. 5.1. The average intensity forecast errors for each West Pacific tropical cyclone by JTWC in 2018. Typhoon Kong-rey is highlighted with the black line which has the storm identifier of wp30.

domain. GDAS includes observations from soundings, aircraft, satellites, and radars to provide the best possible estimate of the state of the atmosphere with buoys, ship, and satellite data also providing estimates of sea surface temperature (SST).

To best compare the observations to the discretized model fields, high resolution near the location of the R/V *Thomas G. Thompson* is required. The model is set up with one nested domain centered on Typhoon Kong-rey with 2-km resolution and 801 x 701 grid points. The large area of the inner domain allows for the relative position of the ship to be evaluated at all times at 2 km resolution. The moving vortex-following nest is embedded in a larger parent domain extending 5000 km x 4000 km at 10 km resolution. The new Tiedtke convective parameterization is used to parameterize convection on the larger parent domain (Tiedtke 1989). To accurately simulate the interactions between radiation and clouds, 50 vertical eta levels is used extending up to an altitude of 20 km which are stretched to finer resolution in the boundary layer and near the tropopause. Prior to analysis, variables are linearly interpolated to fixed vertical height coordinates. The model is initialized at 00 UTC 29 Sep and integrated for three days with output every 30 minutes. The first three hours are not analyzed while the model develops and organizes convection in the tropical cyclone.

The sensitivity of Typhoon Kong-rey's intensity and rainband structure to microphysics-radiation schemes is investigated in four experiments. The experiments consist of combinations of the Thompson aerosol-aware microphysics scheme (Thompson and Eidhammer 2014) and WRF single moment 6-class microphysics (WSM6; Hong and Lim 2006) scheme with two shortwave radiation schemes:

Dudhia (Dudhia 1989) and the Rapid Radiative Transfer Model for General Circulation Models (RRTMG; Iacono et al. 2008). In total, four simulations are conducted that provides comparisons with the same schemes implemented in previous modeling studies. Tang and Zhang (2016) used the WSM6 and Dudhia combination in their simulations of Hurricane Edouard. Dunion et al. (2019) characterized diurnal pulse structure in a nature run using the WSM6 and RRTMG schemes. The combination of WSM6 and RRTMG is also important to include and compare because of its grouping in the “tropical" suite of schemes which is defaulted to in new versions of WRF. The coordination of the Thompson and Dudhia schemes were analyzed in Trabing et al. (2019) and Chapter 3. Thompson-Dudhia was also found to perform well in simulating the fidelity of both radar observations and the intensity of Hurricane Arthur (Brown et al. 2016). The Thompson-RRTMG scheme was also analyzed in Trabing et al. (2019) and are part of the analysis shown by Bu et al. (2014). The boundary layer and surface schemes defined in the “tropical" suite which includes the YSU boundary layer scheme (Hong et al. 2006b) and the MM5 surface layer physics (Jiménez et al. 2012) are employed in the experiments.

5.2.2 Single Domain Sensitivity Experiments

The simulations of Typhoon Kong-rey discussed in the previous section are computationally expensive, which limits the number of sensitivity tests to individual radiation and microphysics schemes. Further tests are warranted to test the sensitivities of convection to shortwave radiation and microphysics in an environment that is not complicated by a tropical cyclone circulation. To better address sensitivities to the radiation and microphysics schemes, additional tests in a single idealized domain using WRF are performed.

The setup for the single domain experiments are all the same except for the varying cloud microphysics and shortwave radiation schemes employed. The experiments are initialized using the average temperature and moisture profile from the PISTON field campaign. The domain is 250 by 250 grid points at 1.5 km resolution in the horizontal with 37 vertical levels. The simulations are not perturbed in any way and convection spontaneously develops forced by radiative tendencies over the diurnal cycle. This setup is similar to a radiative-convective equilibrium experiment, but the model is integrated for 5 days and the last four days are analyzed. Because of the differences in heating/cooling rates in the simulations, the environments in each simulation changes as it moves to a new equilibrium. The 4 days of analyses allows for a robust sample of vertical profiles to compare the schemes against while limiting the changes to the environment that would be more pronounced at longer time scales. Although a number of combinations of radiation and cloud microphysics schemes are tested, here only

the Thompson microphysics will be shown with the CAM (Collins et al. 2006), Goddard (Chou and Suarez 1994), New Goddard (Chou and Suarez 1999), GFDL (Fels and Schwarzkopf 1981), Dudhia, and RRTMG in this framework.

5.2.3 Observations from PISTON

The observations that will be compared to the WRF experiments will be from the PISTON field campaign. Comparisons will be conducted using observations from several instruments, including the Advanced Himawari Imager (AHI), a dual-polarimetric Sea-faring C-Band radar (SEA-POL), and thermodynamic soundings launched every three hours. A more detailed description of the observations can be found in Chapter 4.

During the PISTON field campaign, observations were collected while Typhoon Kong-rey approached the location of the R/V *Thomas G. Thompson*. The ship position did not change during this time, so the observations from the ship largely represent a Eulerian perspective. In storm relative coordinates, the ship was within 500 km of the storm center for approximately two days from 18 UTC 29 Sep to 18 UTC 1 Oct. The ship was within 400 km of the center of Typhoon Kong-rey for ∼12 hours. Because of the likely differences in the track of the simulated TCs, the storms will be analyzed using the storm relative radii and azimuth from the ship instead of the physical location in space and time. Using the storm relative location of the ship eliminates any inconsistencies in the simulations due to differences in track. The differences that are identified between the model experiments and observations are therefore tied to the simulated rainband structure. The change in radial position with time of the ship allows for a better comparison with observations; however, it adds an additional complication to the system. To allow for a better interpretation of the effects of shortwave radiation and microphysics on the storm structure and intensity, a range of fixed radii based on the ship location is used in the comparisons. Although comparisons of the observations and experiments are motiving this chapter, the goal is to evaluate the expected diurnal variability associated with diurnal pulses and the diurnal cycle and not a position based verification.

5.3 Evolution of the Simulated Structure and Intensity

In order to diagnose how well the experiments capture tropical cyclone rainbands, the accuracy of the intensity and track forecasts of Typhoon Kong-rey need to be considered. Figure 5.2 shows the intensity and track evolution of Typhoon Kong-rey in each of the experiments and the best-track from JTWC. All four models had a left of track bias that brought the center of Typhoon Kong-rey closer to

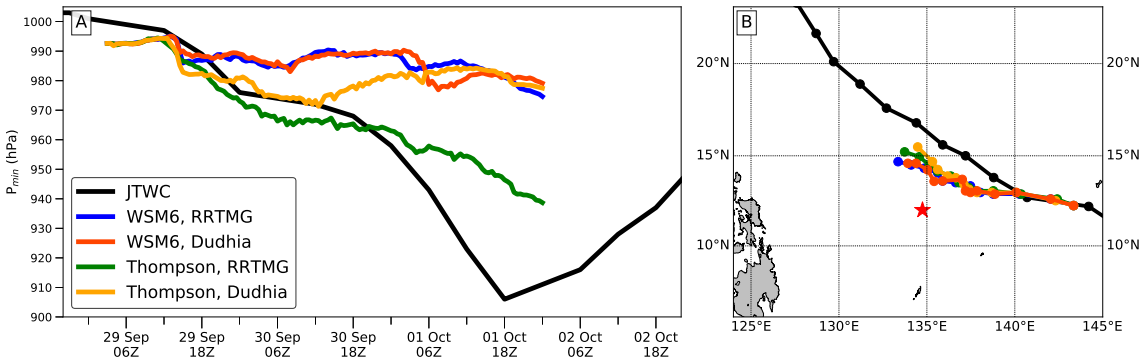

FIG. 5.2. The evolution with time of the minimum central pressure at the surface (a) and center position (b) of the four experiments. Times shown begin at 03 UTC to allow for the simulations to initialize convection and the tropical cyclone circulation. The black line is the official best track estimates from JTWC. The track forecasts are shown every six hours for better comparisons between the models. The red star is the location of the R/V *Thomas G. Thompson* during the time period of interest.

the position where observations were collected. The variations in the track between the experiments is overall small and does not explain any differences in the intensity because SST is spatially uniform in the region. The intensity of the Typhoon Kong-rey, shown as the minimum central pressure at the surface, shows more variability than the track. From 00 UTC to 09 UTC 29 Sep the intensity of the tropical cyclones are all similar which is to be expected given that the thermodynamic environments and synoptic scale forcing is all the same. The intensities begin to diverge beyond 18 UTC 29 Sep with the Thompson simulations suggesting a deepening of the low while the WSM6 simulations suggest a more steady state intensity around 990 hPa. Thompson-RRTMG intensifies the vortex the most and overestimates the intensity, while the Thompson-Dudhia well captures the intensity from 06-12 UTC 30 Sep. Beyond 12 UTC 30 Sep, the Thompson-Dudhia experiment weakens the storm bringing the intensity in line with the WSM6 experiments. From 06 UTC 1 Oct through the end of the simulation, the WSM6 experiments and Thompson-Dudhia all have similar intensities with a slow intensification to around 980 hPa by 00 UTC 2 Oct. Of the four models, only Thompson-RRTMG intensifies Typhoon Kong-rey into a strong typhoon comparable to reality, although the intensity is still weaker relative to observations. The strong sensitivity of Typhoon Kong-rey's intensity to the microphysics and radiation schemes may be due to changes to the diabatic heating rates from inner-core convection and the underlying structure of the tropical cyclone.

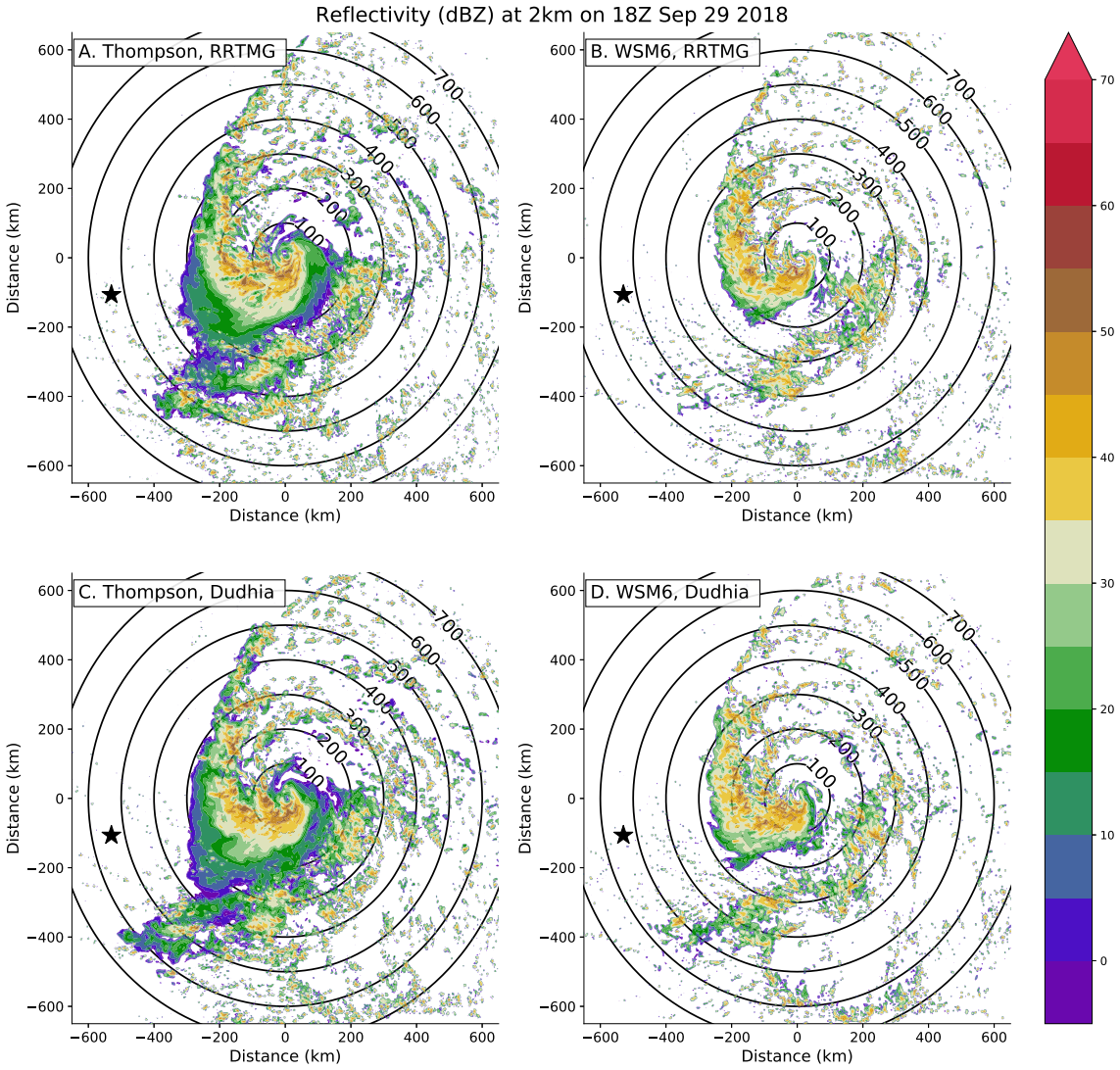

FIG. 5.3. Horizontal cross sections of simulated reflectivity at 2 km altitude at 18 UTC 29 Sep for each experiment. Reflectivity is contoured every 5 dBZ with values below -5 dBZ removed. Range rings every 100 km are shown with the black star being the storm relative position of the R/V *Thomas G. Thompson* to Typhoon Kong-rey at the time.

Next the microphysics and radiation effects on the structure of Typhoon Kong-rey is examined. In order to determine whether the structure of Typhoon Kong-rey was accurately simulated, the horizontal cross sections of the 2-km simulated radar reflectivity on 18 UTC 29 Sep is compared in Fig. 5.3. To first order, the experiments all show similar overall large-scale structure with a north-south oriented primary rainband wrapping into the center of Typhoon Kong-rey. At this time the model has been integrated for 12 hours and large differences in the structure are not expected given the same initial conditions. The largest differences at this time between the Thompson and WSM6 experiments occur in

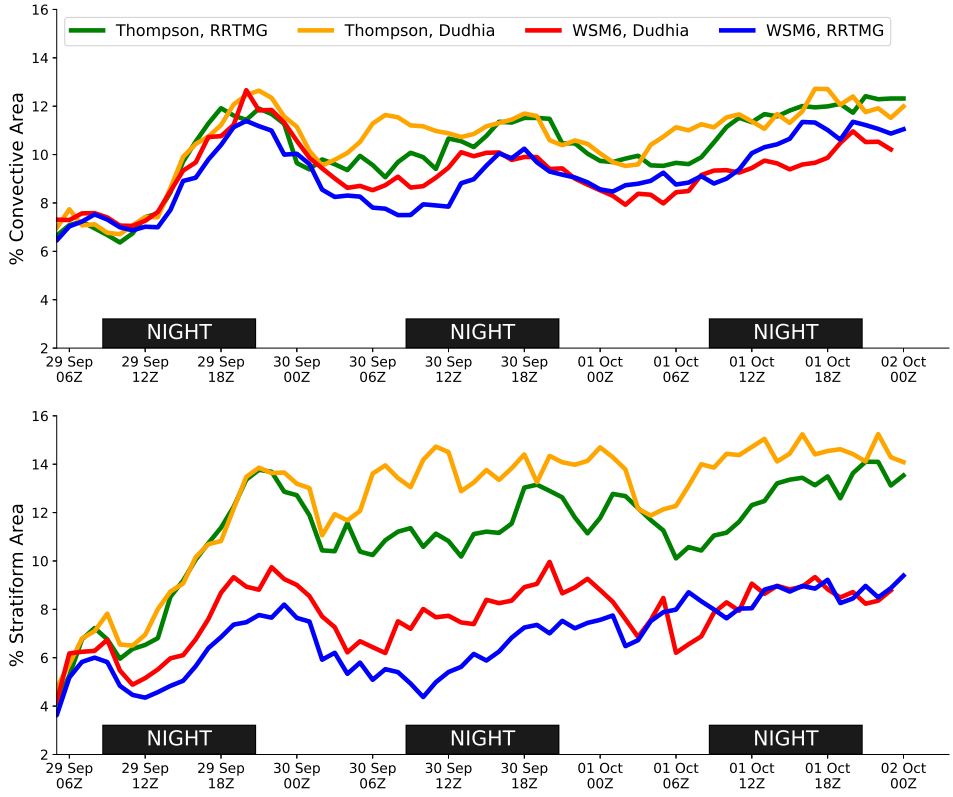

FIG. 5.4. The evolution of the areal extent within 500 km of the tropical cyclone center of convective defined clouds (a) and stratiform (b) clouds for each experiment. Nighttime periods are denoted with the black text boxes for reference with the solar cycle.

the weak echo regions. The Thompson scheme has a large area of 10-20 dBZ echo values downstream of the primary rainband. The WSM6 experiments show more discrete echo regions with smaller areas of stratiform precipitation. The differences in stratiform precipitation are tied to the microphysics scheme which is dominating the differences over the first 12 hours.

The apparent change in stratiform precipitation between the microphysics schemes in Fig. 5.3 can be better quantified using a convective-stratiform partition. The same convective-stratiform partitioning algorithm used in the previous chapters developed by Yuter and Houze (1997) is employed on the experiments. Figure 5.4 shows the evolution of the convective and stratiform fraction within 500 km of the storm center. To first order, the Thompson microphysics create a 2-4% larger area of stratiform precipitation throughout time. The importance of stratiform precipitation in generating stronger mid-level vorticity to support tropical cyclogenesis has been noted by Bell and Montgomery (2019) and could help explain the faster genesis and intensification of the Thompson experiments. In addition, there was a ∼1% increase in the convective area in the Thompson compared to WSM6 schemes. The

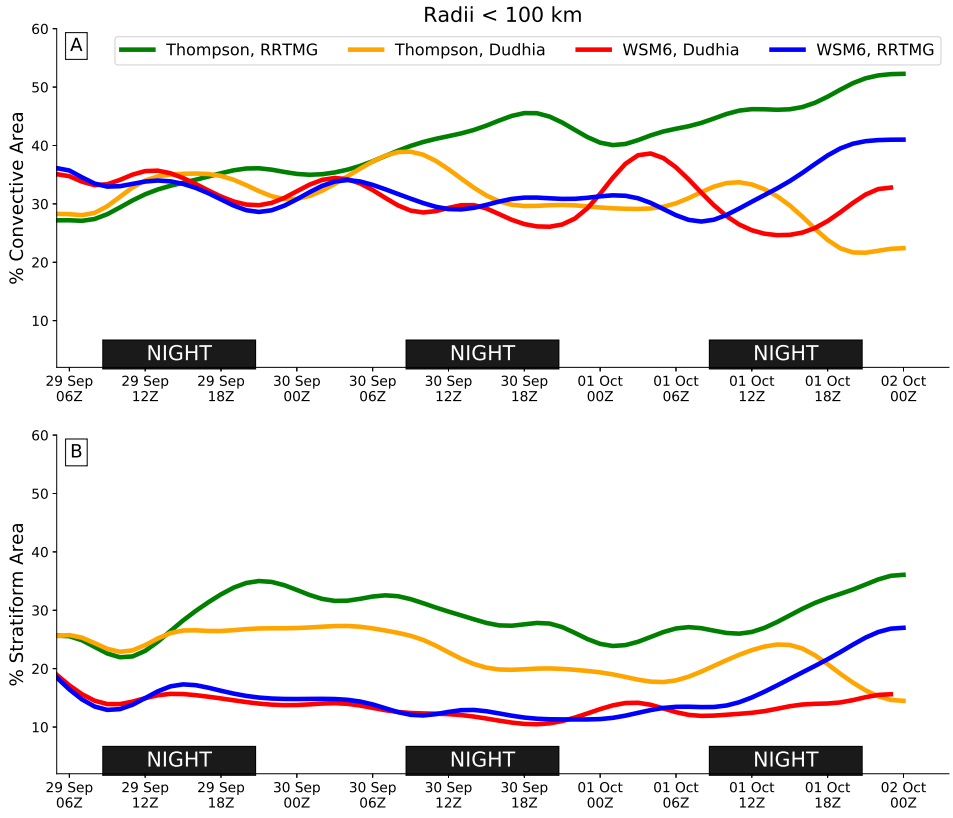

FIG. 5.5. Same as Fig 5.4 but for convective and stratiform echoes within 100 km of the storm centers. Lines are smoothed using a gaussian filter to improve figure readability.

increased convective area would also supports a faster genesis and intensification of the low-level vortex in the Thompson experiments. The shortwave radiation scheme also plays a role in the amount of stratiform precipitation primarily during the daytime. The experiments with Dudhia shortwave radiation tended to have more stratiform precipitation within 500 km and more convection in the late afternoon to evening hours. This would suggest direct effects of shortwave radiation through stabilizing the upper-troposphere similar to what was shown in Chapter 2. If the relative area within 100 km of the TC center shown in Fig. 5.5 is considered, the percentage of stratiform area increases in the Thompson experiments and are directly correlated with the intensities of each experiment in Fig. 5.2. The area of convection through the first 24 hours within 100 km is similar in all the experiments, which suggests that differences in stratiform precipitation caused by the microphysics schemes are driving the short term intensity differences.

By the end of the simulations, the structure of the TCs between experiments shows larger differences due to the shortwave schemes and the interactions with the microphysics schemes that accumulate with time. Figure 5.6 shows the 2-km simulated reflectivity at 18 UTC 1 Oct. The structure

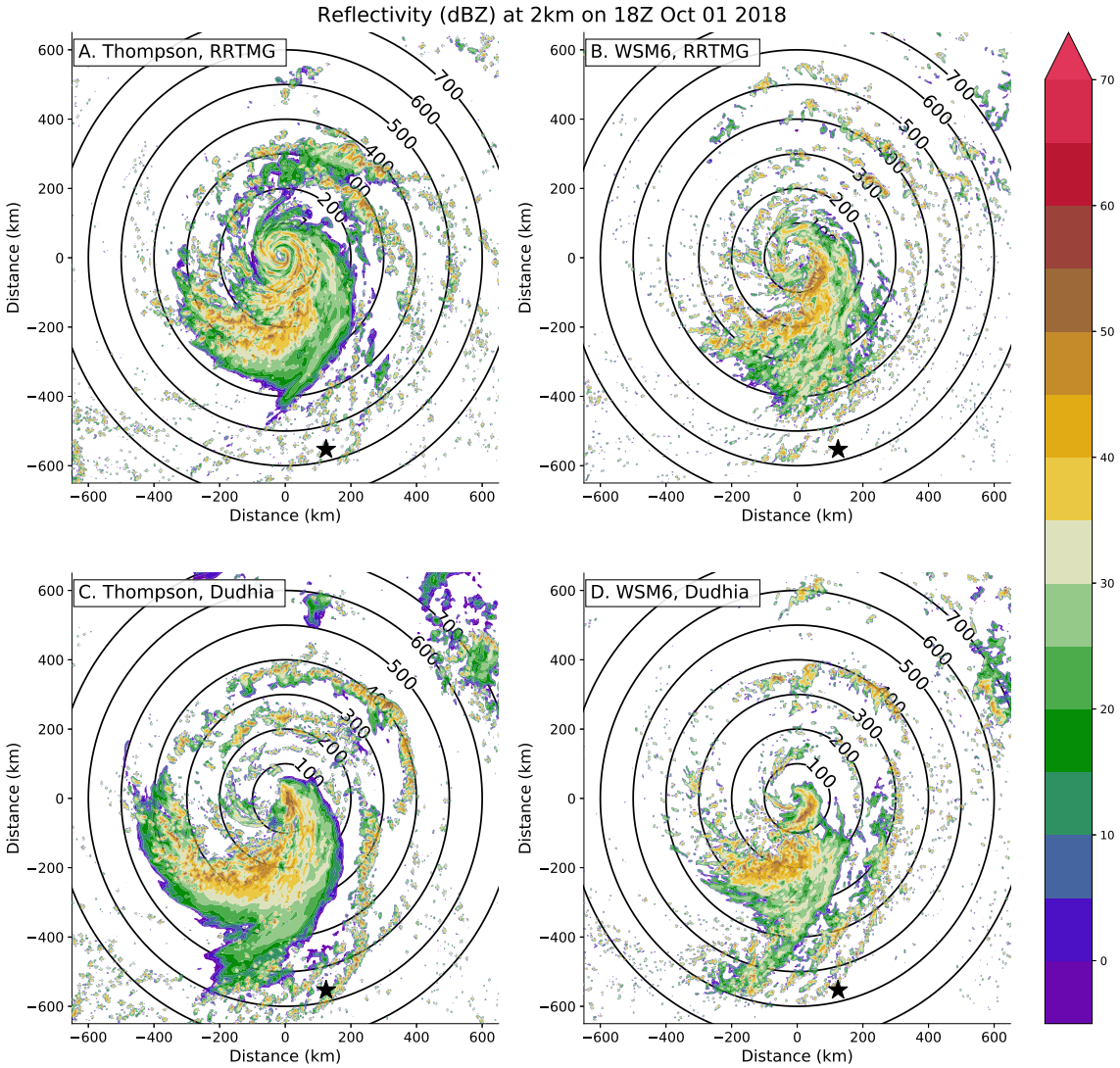

FIG. 5.6. Same as Fig. 5.3 but for 18 UTC 1 Oct.

of Typhoon Kong-rey is fairly consistent between the simulations, which is at forecast hour 66. The primary rainband is now located on the south side of Kong-rey's center, which is located in the down-shear quadrants. The consistent location of the primary rainband suggests that the overall synoptic patterns are not governing the differences in structure and intensity of the simulated TCs. The structure of the Thompson with RRTMG TC shows a more axisymmetric reflectivity profiles near the center of the storm, which is indicative of its stronger intensity. The WSM6-RRTMG simulation also appears to have banding that has managed to axisymmeterize around the center, while both Dudhia simulations show a wavenumber-1 asymmetry of convection near the center. Overall, the experiments with

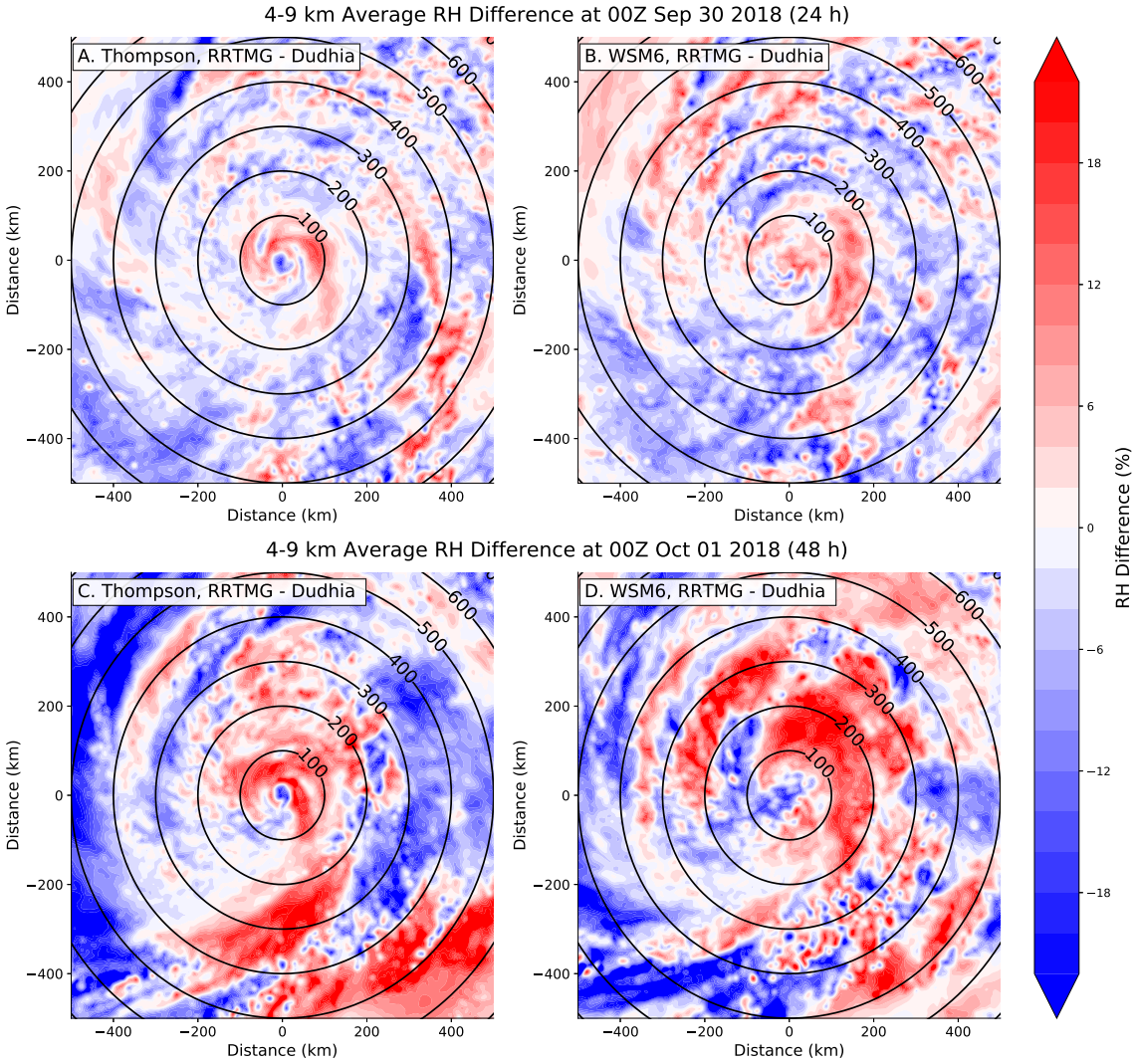

FIG. 5.7. The difference between the 4-9 km averaged RH between the RRTMG and Dudhia experiments for the Thompson (a, c) and WSM6 (b, d) microphysics. The differences are shown for two separate time periods 24 h (a, b) and 48 h (c, d) into the simulations at 00 UTC 30 Sep and 00 UTC 1 Oct, respectively. RH fields are filtered using a 2D gaussian filter to remove convective scale perturbations and to improve figure readability. Range rings every 100 km are shown to orient the reader.

the Dudhia shortwave radiation appear more asymmetric than those with RRTMG regardless of the microphysics at this time. The difference between the Dudhia and RRTMG TC structure could be related to changes in the thermodynamics environment driven by differences in shortwave heating.

To investigate why asymmetries were more pronounced in the Dudhia experiments compared to the RRTMG experiments at longer forecast times, the differences in the moisture are examined. Figure 5.7a-b shows the difference in 4-9 km average relative humidity (RH) at the 24-h mark between the RRTMG and Dudhia schemes of the Thompson and WSM6 experiments. The RH shows larger values

in the RRTMG simulations compared to Dudhia near the inner-core of the storms. The RH at radii beyond 200 km on average is higher in the Dudhia simulations. The differences in RH at the 24-h mark (00 UTC 30 Sep) corresponds to 09L time and the RH differences become larger in the afternoon. The differences also accumulate as evident by the differences in RH at the 48-h mark (00 UTC 1 Oct) shown in Fig. 5.7c-d. The larger RH anomalies >20% are found in in the upshear region on the northeast side of the storms. The higher RH closer to the storm center and in the upshear region in the RRTMG experiments compared to the Dudhia experiments seems to be related to the convective organization and development of an eyewall. Entrainment of the drier air into convection near the center of the Dudhia TCs prevents the development and axisymmeterization of the eyewall which favors a weaker storm intensity (Tang and Emanuel 2010). It should be noted because the WSM6-Dudhia experiment is already weaker and the RH anomalies occur at a slightly larger radius, the drier air compared to the WSM6-RRTMG has a smaller effect on the overall intensity of the storm. Since Thompson-Dudhia was ∼20 hPa deeper at that time and the drier air is closer to the center, the effects on the intensity are larger. Questions remain as to whether this dry air is caused by direct shortwave heating differences or are caused by an indirect response to the distribution of stratiform precipitation or a combination of both. The overall differences show that both the microphysics and shortwave radiation plays an important role in the structure and intensity of the simulated TCs that are important to identify.

Another component that has yet to be explored is how the size of the TCs evolved. Figure 5.8 shows the evolution of the radius of maximum winds (RMW) at an altitude of 1 km in the four experiments. The RMW is derived from the axisymmetric tangential wind field and will be heavily impacted by the strong primary rainband that sets up in the simulations shown in Fig. 5.3. The strength of the primary rainband and the diabatic heating it generates in the different microphysics schemes will contribute to the different locations of the RMW evident at the early times. By 00 UTC 30 Sep (24 h) the RMW has become modified by both the microphysics and the shortwave radiation scheme such that the Thompson microphysics is favoring a smaller RMW compared to the WSM6, while Dudhia experiments are creating slightly larger storms compared to the RRTMG experiments. Because the RMW is not necessarily well defined in weaker TCs, the variability is larger in the WSM6 experiments. The entrainment of dry air into the eyewall of the Thompson-Dudhia experiment leads to the expanding RMW with time beyond 12 UTC 30 Sep. Around 06 UTC 1 Oct, the RMW in the WSM6-Dudhia experiment stops expanding and redevelops in a similar location as the WSM6-RRTMG experiment. A movement inwards

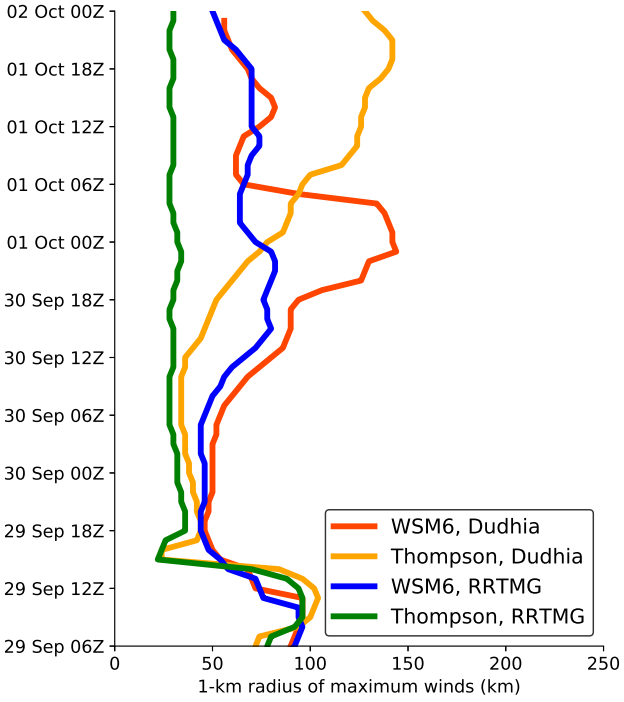

FIG. 5.8. The evolution of the radius of maximum wind (RMW) at 1-km for each experiment. The tangential winds are smoothed using a gaussian filter prior to calculation to improve figure readability.

of the RMW is not surprising because bands of convection radially inward can more easily project onto the axisymmetric mean where the inertial stability is large.

The preceding section has analyzed the effects that changing the microphysics and shortwave radiation scheme has on the simulation of Typhoon Kong-rey's intensity and structure evolution. The simulations all do a good job in characterizing the initial structure of the TC with the Thompson scheme creating an increased amount of stratiform precipitation. The enhanced stratiform precipitation likely contributes to faster generation of the mid-level vortex and genesis in the Thompson experiments compared to the WSM6 experiments. The larger amount of stratiform in the Thompson experiments can largely be attributed to overall reduced rain evaporation rates in stratiform regions compared to the single moment WSM6 experiments which has an assumed rain size distribution shape parameter (Morrison et al. 2009). The primary obstacle for genesis and RI is the northeasterly vertical wind shear, which the Thompson experiments are initially able to overcome. The effects of the different shortwave radiation schemes accumulate with time and are strongest in the late evening. The largest difference between the Dudhia and RRTMG schemes is tied to the upshear regions of drier air that reduces the

strength of the inner-core convection and overall intensity evolution. Only the Thompson-RRTMG experiment realistically capture the intensity evolution of Typhoon Kong-rey, and this chapter will now focus on whether the experiments were able to capture the observed diurnal oscillations in the brightness temperature from PISTON.

5.4 Simulating Diurnal Oscillations in the Outflow Layer

Although only the Thompson-RRTMG experiment was able to capture the overall intensity of Typhoon Kong-rey, it is unclear if any of the experiments are able to capture the diurnal oscillations in the brightness temperatures shown in the observations from PISTON. These diurnal oscillations were coupled with diurnally driven outflow jets that were observed from thermodynamic soundings above the position of the R/V *Thomas G. Thompson*. The outflow jets were followed by outward propagating convective rainbands which were consistent with Dunion et al. (2019). It will be examined whether the simulations were able to capture the various aspects of these diurnal pulses and potential differences due to the microphysics and shortwave schemes. Although asymmetries are fairly pronounced at the beginning of the experiments due to vertical wind shear, the diurnal oscillations in an axisymmetric framework is analyzed to allow for a more coherent analysis with time and comparison with the observations from PISTON.

First, the simulated brightness temperatures are examined. The outgoing longwave radiation (OLR) is used as a proxy for the infrared (IR) brightness temperature which will be highly correlated to the 10.4 μm brightness temperatures from the AHI. Planck's law is used to convert the OLR at the top of the model simulation to a brightness temperature. While the simulated IR brightness temperatures are capturing both the cirrus and thicker anvil cirrus, the two cannot confidently be differentiated in this chapter. Figure 5.9 shows the evolution of the axisymmetric brightness temperatures for each experiment. To first order, the Thompson microphysics scheme produces a larger amount of ice and snow at the upper-levels contributing to more similar emissivity values over a large area. The colder temperatures also indicates that the convection in the Thompson experiments are reaching higher altitudes. The WSM6 experiments have larger variability in the simulated IR brightness temperatures compared to the Thompson experiments and are overall warmer. If the results are compared directly to the observed 220 K brightness temperature, the WSM6 experiments are too warm with the coldest temperatures extending not far enough from the center. The Thompson experiments have brightness temperatures that are too cold extending too far radially outwards compared to the observations. The

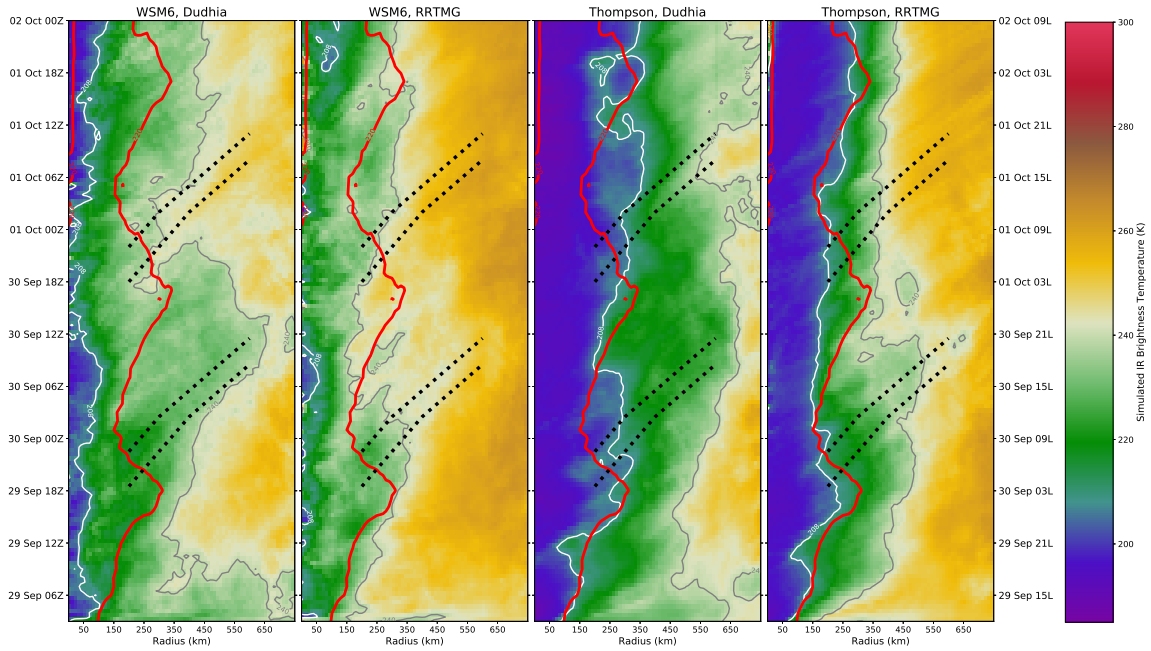

FIG. 5.9. The evolution with time of the axisymmetric simulated brightness temperatures from each of the experiments. The rightmost ordinate shows the local time for reference with the diurnal cycle. The black dotted lines represent the expected timing bounds for the diurnal pulses found in Dunion et al. (2014). The white and gray contour lines are the simulated 208 K and 220 K temperatures similar to Fig. 4.8. The red solid line is the axisymmetric 220 K brightness temperature contour that was observed from the AHI during PISTON.

shortwave radiation scheme plays a role in the extent of the upper-level clouds because the Dudhia scheme produces larger areas of colder brightness temperatures compared to the RRTMG experiments. It is important to remind the reader that the same longwave radiation schemes are employed in each experiments such that the IR differences shown are due solely to changes in the cloud distributions and interactions with the shortwave radiation.

In Fig. 5.9 there does not appear to be any robust diurnal oscillations in the simulated brightness temperatures comparable to the observations of PISTON. Regardless of the biases in the schemes towards warmer/colder brightness temperatures, none of the experiments produce a classical diurnal pulse in regards to Dunion et al. (2014) or an off the clock diurnal oscillation shown in Chapter 4. The initial expansion of the cloud canopy from 06 UTC (15L) 29 Sep to 06 UTC (15L) 30 Sep is present to varying degrees in the experiments which seems to highlight some key differences between the models. The first outward expansion on 29 Sep was the only diurnal pulse like feature in the simulated brightness temperatures that is remotely close to the observations. The Thompson-Dudhia experiment shows

the least realistic brightness temperature evolution which covers too large of an area. The Thompson-Dudhia experiment is the only model that does not indicate any warming of the upper-level cloud layer associated with direct shortwave heating and/or descent and associated adiabatic warming. The edge of the cloud canopy in the WSM6-Dudhia experiments expands too far radially outwards and persists too long which is similar to Thompson-Dudhia, but does a better job in warming the 150-350 km radii cloud layer starting around 12L 30 Sep. Both RRTMG experiments also indicate a warming and dissipation of the clouds but disagree somewhat on the timing likely due to the differences in thickness of the cloud layer. The lack of consistent diurnal oscillations may be related to the weaker intensity of the storm compared to reality; however, even the stronger Thompson-RRTMG experiment did not exhibit detectable diurnal oscillations in the brightness temperatures. The underlying reason for the overall weaker TC intensity, being the vertical wind shear and dry air entrainment could also play a role in disrupting the diurnal cycle of convection and weakening outward propagating rainbands (Knaff et al. 2019; Ditchek et al. 2019a). At this point it is uncertain whether the lack of diurnal cycles is because of a misrepresentation of upper-level clouds and their dynamics or related to other parameterizations in the models.

In addition to the diurnal oscillations in the brightness temperature, associated outflow jets were also observed. Figure 5.10 shows the evolution of the maximum outflow and maximum inflow throughout the experiments. Overall there are a few differences between the experiments to consider. The Thompson-RRTMG experiment is the only experiment to capture the intensification of Typhoon Kongrey and has the strongest maximum inflow; however, it curiously also has a consistently weaker maximum outflow compared to the other simulations. The strongest maximum outflow is found in the Dudhia experiments which are curiously not associated with the periods of intensification. The strongest outflow winds in the Thompson-Dudhia occur after 12 UTC (21L) 30 Sep which is when the peak intensity and strong inflow of the storm begins to weaken due to dry air entrainment into the eyewall convection. A stronger outflow is generally considered an indicator for intensification (Merrill 1988; Komaromi and Doyle 2017), but the lack of connection with the inflow supports the argument for entrainment of drier mid-level air into the inner-core convection. It should be noted that the strongest outflow jet in the WSM6-Dudhia occurs 12 hours later than that of the Thompson-Dudhia but does not appear to to be coincident with dry-air entrainment because the maximum inflow increases sharply

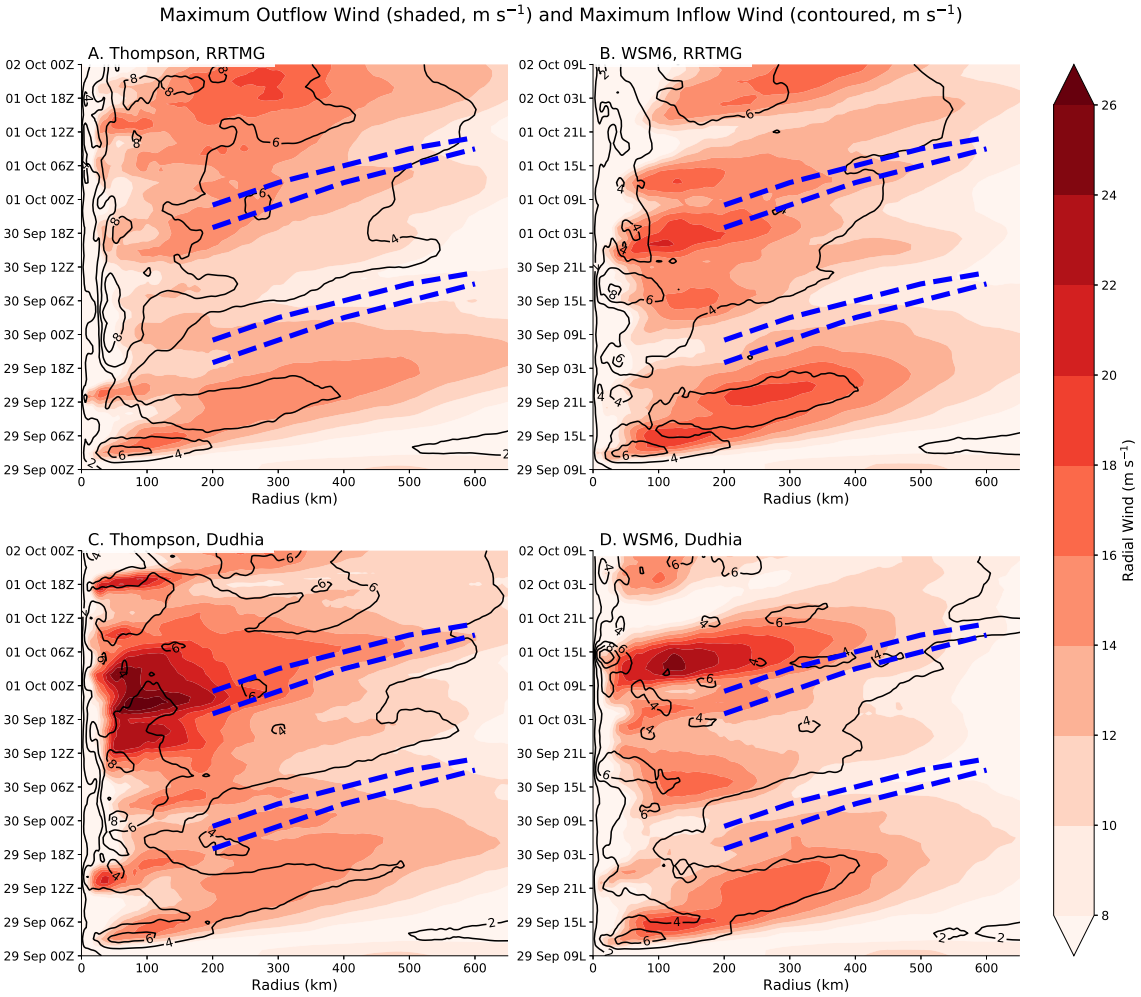

FIG. 5.10. Evolution of the maximum axisymmetric radial wind at any altitude (i.e. max outflow; shaded) and the minimum axisymmetric radial wind at any altitude (i.e. max inflow; contoured). Both max inflow and outflow are contoured are every 2 m s^{-1}. The blue dashed lines represent the expected timing range of the diurnal pulses found in Dunion et al. (2014). The ordinate of (a) and (c) are shown in UTC while the ordinate of (b) and (d) are shown in local standard time. The radial wind is filtered using a 2D gaussian filter to improve readability.

and the intensity increases (Fig. 5.2a) at that time. It should be noted that directly comparing the maximum inflow and outflow to the observations from PISTON is difficult; however, the diurnal variability is explored.

Based on the results of Dunion et al. (2019) it is expected to see diurnally driven outflow jets around the approximate times highlighted using the blue dashed lines in Fig. 5.10. None of the experiments resolved the diurnal pulses in the outflow layer on the “Dunion" clock which is consistent with the observations and the interpretation of the simulated IR brightness temperatures. Near the beginning of all four experiments from 06 UTC (15L) 29 Sep to 06 UTC (15L) 30 Sep, there is an outward propagating

outflow jet that is coincident with the expanding cloud canopy in Fig 5.9. The outward propagating outflow maximum was slightly stronger and more robust in the WSM6 experiments compared to the Thompson experiments. Although there is some variability in the outflow speeds during the expansion of the cloud canopy, the differences between the Dudhia and RRTMG experiments are small. The RRTMG experiments produced a smaller areal extent of upper-level clouds compared to the Dudhia experiments yet they had similar maximum outflows. The shortwave radiation schemes are likely heating different portions of the upper-level clouds which is causing a faster warming and dissipation of the clouds in the RRTMG scheme compared to the Dudhia.

The WSM6 experiments also appear to have more robust oscillations in the peak outflow on diurnal time scales. Everyday between 09-15L in the WSM6 experiments there is a peak in the maximum outflow which is maximized between radii of 100-150 km. The peaks in outflow at these times correspond to the diurnal cycle of shortwave heating and suggests a dynamic response to the heating in the outflow layer which is consistent with the idealized simulations shown in Chapter 3 and previous studies (Navarro and Hakim 2016; Ruppert and O'Neill 2019). The diurnal oscillations in the outflow of the Thompson experiments is harder to discern because the outflow is more variable with less pronounced peaks. Multiple diurnal oscillations in the Thompson-Dudhia scheme are masked by the strong outflow during the period where the TC intensity is weakening. The entrainment of dry air leading to weakening convection could disrupt the diurnal cycle of convection in the Thompson-Dudhia. There also seems to be another diurnal signal in some of the experiments where peak outflow closer to the center of the TCs is strongest in the overnight to early morning (12Z-20Z, 21L-05L) hours, corresponding to the expected diurnal cycle of convection. The peak outflow at these times (21L-05L) are generally located radially inward of the afternoon outflow peaks and does not extend to large radii. These smaller outflow maximums collocated with the diurnal cycle of convection do not appear to be robust but could be related to the diurnal cycle of convection. The maximum inflow shown in Fig. 5.10 could also be used to qualitatively evaluate the Gray and Jacobson (1977) mechanism for enhancing nocturnal convection by enhancing low-level inflow due to the differences in longwave cooling between the clear-air and cloudy regions of the storm. Between 00 UTC (09L) 29 Sep to 00 UTC (09L) 30 Sep the 4 m s^{-1} maximum inflow contour closely follows the maximum outflow in each experiment suggesting to some degree that they may be coupled to convection. From 06-18 UTC (15L-03L) 30 Sep (1 Oct) there is another expansion in the 4 m s^{-1} maximum inflow contour radially outward but with weaker outflow above. The timing of this radially outward propagating region of inflow seems to be related more

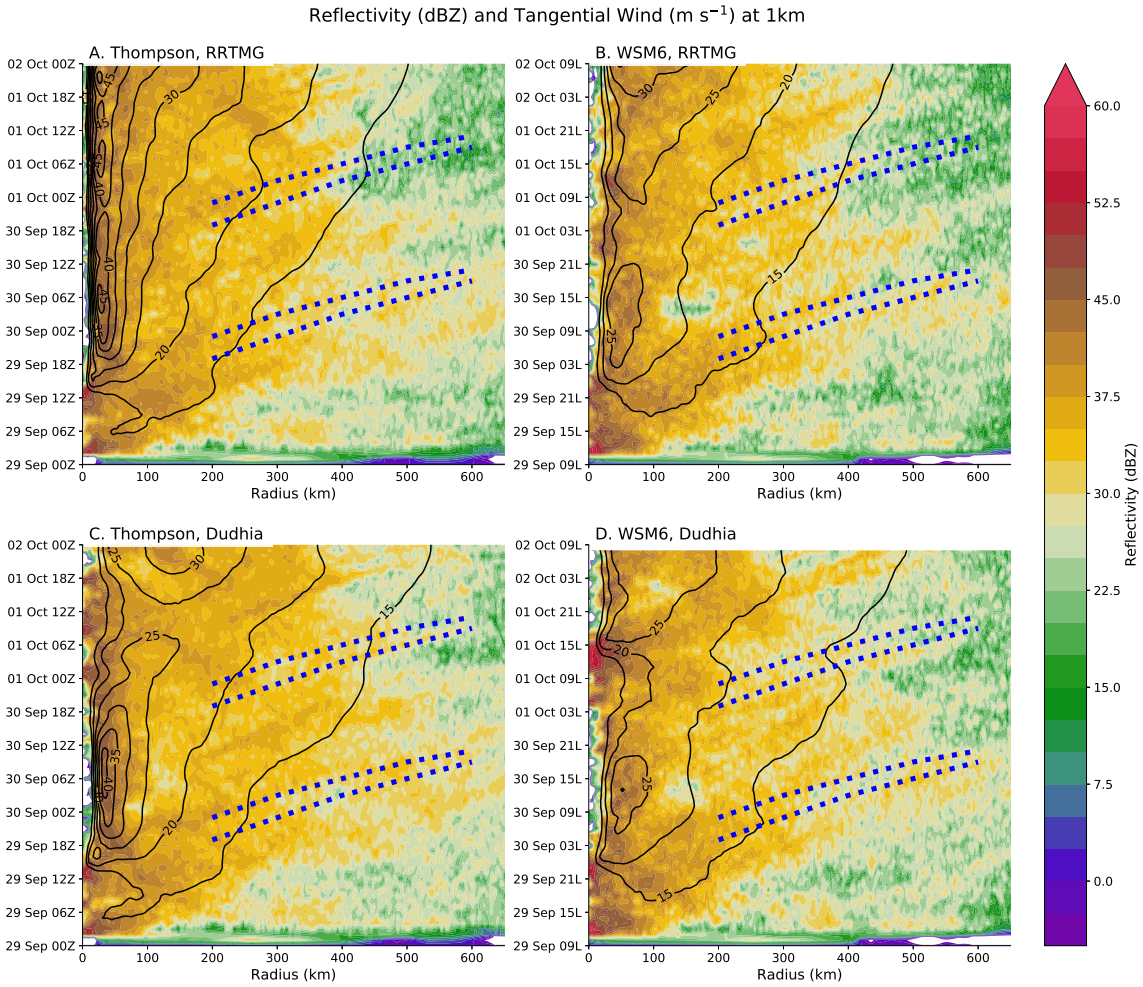

FIG. 5.11. The evolution of the axisymmetric simulated reflectivity at 1 km for each experiment is shown. The axisymmetric tangential winds at a height of 1 km are shown and contoured at 5 m s^{-1} intervals starting at 15 m s^{-1}. The blue dotted lines represent the expected timing range of the diurnal pulses found in Dunion et al. (2014). The ordinates of (a) and (c) are shown in UTC while the ordinate of (b) and (d) are shown in local standard time. The tangential wind only is filtered using a gaussian filter to improve readability.

to outward propagating convection than the diurnal cycle convection driven by enhanced nocturnal low-level convergence.

The maximum inflow and outflow within each experiment tended to move radially outwards together suggesting that convection could be coupled to the features. To verify whether or not there were outward propagating rainbands the axisymmetric simulated 10-cm wavelength reflectivity of each experiment is examined in Fig. 5.11. The tangential winds are also shown in each experiment to explore the relationship between the inner rainbands and tangential wind expansion. Overall, there are no pronounced differences in the reflectivity profiles or the tangential wind expansion between experiments.

The Thompson experiments produced slightly larger wind fields compared to the WSM6 experiments but that is likely due in part to the intensity differences. Consistent with the upper-level outflow and low-level inflow, there appears to be outward propagating areas of reflectivity >30 dBZ. The outward moving convection appears in all of the experiments but is slightly stronger and propagates sooner in the Thompson experiments which could be related to the more pronounced stratiform precipitation. The outward propagating rainbands are indistinguishable from the large area of high reflectivity radially inwards from 200 km through 12 UTC (21L) 29 Sep and are not deep enough to penetrate the outflow layer because they are not represented in the simulated IR. The area of high reflectivity inwards of 200 km does not propagate but is instead a nearly continuous feature of the axisymmetric profiles corresponding to the strong primary rainband shown in Fig. 5.3 and Fig. 5.6. Although there does seem to be outward propagating rainbands at the times consistent with the diurnal oscillations from PISTON and the simulated outflow layer, there is no clear lull in activity between expected diurnal pulses. The lack of diurnal pulses on the expected “Dunion" clock is a consistent feature that is also in agreement with the other variables shown and the observations from PISTON.

In this section it has been shown that while there were not pronounced diurnally driven oscillations in the simulated brightness temperatures, there were diurnally driven outflow jets that seem to be correlated with radially outwards propagating rainbands. The lack of connection between the simulated IR and the convection is partially related to how shortwave radiation leads to dissipation and warming of the upper-level clouds between the RRTMG and Dudhia experiments. The differences between the anvil clouds in the Thompson and WSM6 are likely tied to the fall speeds of the ice and snow distributions. The Thompson experiments produces overall too uniform of upper-level clouds with more snow/ice compared to the WSM6 experiments. Diurnal maxima in outflow tended to be more pronounced in the WSM6 experiments and is likely driven be a dynamic response to the shortwave heating but could also be a response from the convection that is moving radially outwards. Overall the simulation of the outward moving convection coupled with outflow jets are consistent with the observations from PISTON in each of the experiments.

5.5 Sensitivity to Shortwave Scheme

Now that it has been shown that there is some degree of diurnal oscillations in the outflow layer that are colocated with outward moving convective rainbands, it is unclear if the diurnal cycle of convection that was shown using the observations from PISTON is also consistent in the modeling studies. The

day-night CFADs from PISTON shown in Fig. 4.5 suggested that there was a nighttime enhancement of reflectivity aloft and overall taller convection at night compared with slightly larger reflectivity values in the mid-lower levels during the day. CFADs of simulated reflectivity can be directly compared with the observations using the estimated ship location relative to Typhoon Kong-rey at each time; however, the storm relative position leads to sampling inconsistencies depending on the location of the primary rainband and different storm sizes. In order to avoid differences in the timing of rainbands with respect to ship position and also to improve the sample size, all convective points are included from 300-500 km to calculate the diurnal differences in reflectivity CFADs. The 300-500 km radii are used because the closest points that SEA-POL would have observed given its 120 km range would have been ~300 km away from the storm center. In comparing the reflectivity between the simulations and observations it should be noted that the simulated reflectivity includes values that would be below the noise level of the measured return power for SEA-POL. The simulations therefore provide unrealistic numbers of weak echo regions at upper-levels when compared with the observations.

The day-night differences in convective reflectivity CFADs for each experiment are shown in Fig. 5.12. The larger number of points in the experiments compared to the observations reduces the overall magnitude of the differences between the day-night simulated CFADs and the day-night observed CFADs. The overall distribution of reflectivity is largely controlled by the microphysics scheme such that the larger reflectivity values are reached in the Thompson experiments compared to the WSM6 experiments, particularly between 2-10 km. These large reflectivity values >60 dBZ found in the Thompson scheme are all elevated and relatively infrequent. The day-night differences between each experiment vary but the Thompson-Dudhia, WSM6-Dudhia, and WSM6-RRTMG all show a tripole structure above 5 km with a negative anomaly sandwiched by positive anomalies. The upper-level tripole structure suggests that during the day, there are areas of both larger reflectivity values that are elevated and weaker reflectivity values at lower altitudes compared to at night. In all cases the daytime has a stronger positive anomaly located at lower altitudes and lower reflectivity values, which suggests that the shortwave heating led to on average shallower echo tops consistent with the observations from SEA-POL. In the Thompson-RRTMG experiment there is a dipole structure at upper levels, where at night there is a pronounced shift towards larger reflectivity values and a shift towards lower reflectivity values during the day at most altitudes. The day-night differences in the Thompson-RRTMG are also more pronounced below 5 km which is in contrast to the other experiments. The WSM6-RRTMG has a similar shift at night towards larger reflectivity values indicating that the RRTMG scheme may

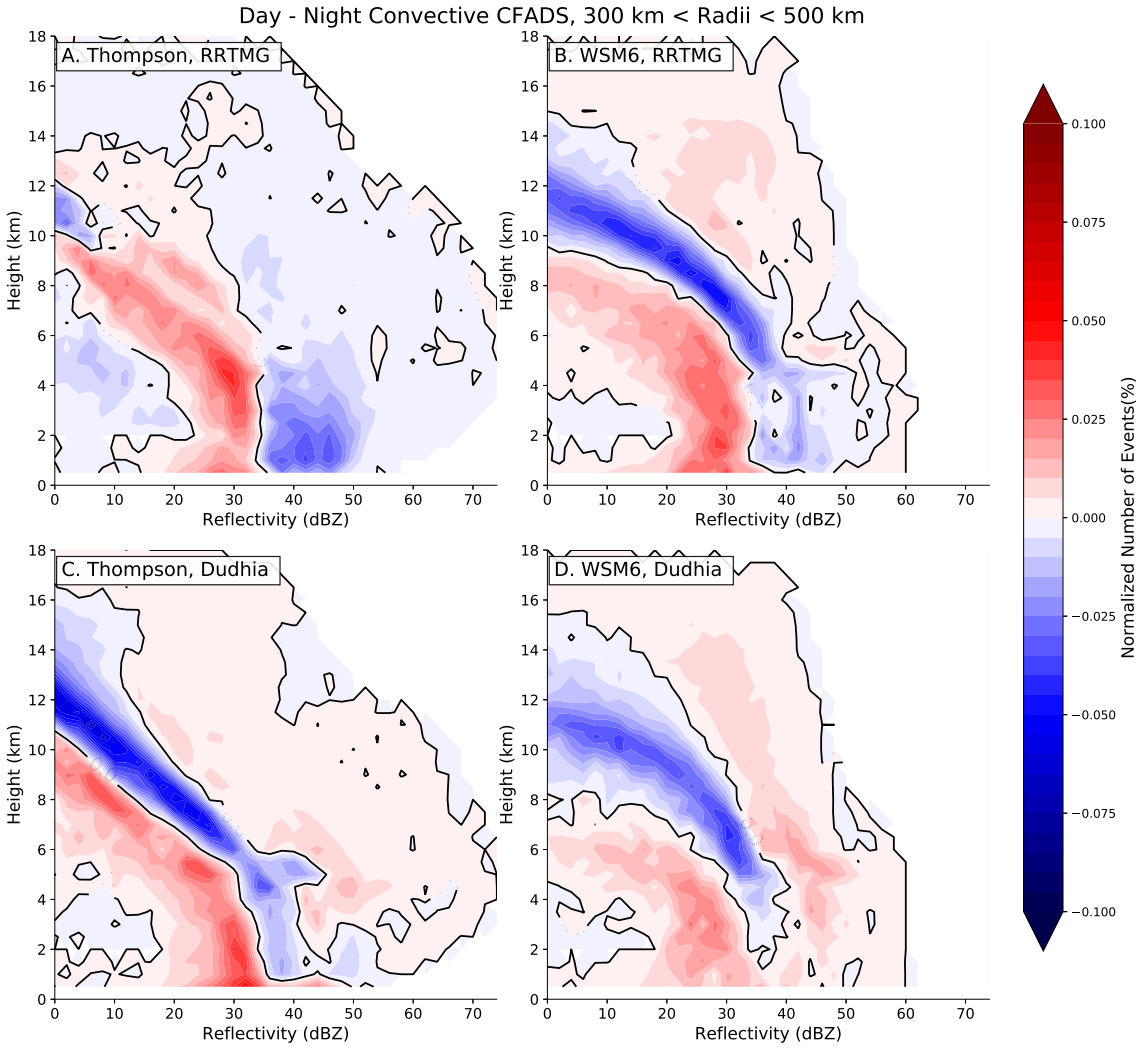

FIG. 5.12. Daytime (21-09 UTC) minus nighttime (09-21 UTC) CFAD of reflectivity for convective identified echoes in each simulation of Typhoon Kong-rey. CFADs are for the radii between 300 and 500 km at all time periods and are binned at 2 dBZ intervals. CFADs are normalized by the total number of points in each CFAD to remove differences between the amount of convection in the samples. White regions are where no values were recorded in either the day or nighttime sample. The black line is the zero difference contour line.

contribute to larger diurnal variability in convection near the surface. The observations from PISTON around Typhoon Kong-rey showed higher reflectivity during the day at low-mid levels which is more consistent with what is shown by the Dudhia experiments.

One key distinction in understanding the comparison of Fig. 5.12 and Fig. 4.5 is that the simulated experiments had varying degrees of upper-level clouds represented in the simulated IR imagery. Even though the observations collected during PISTON were all under an expansive cirrus canopy, using the 300-500 km radii in the experiments causes a varying degree in the amount of clouds overhead

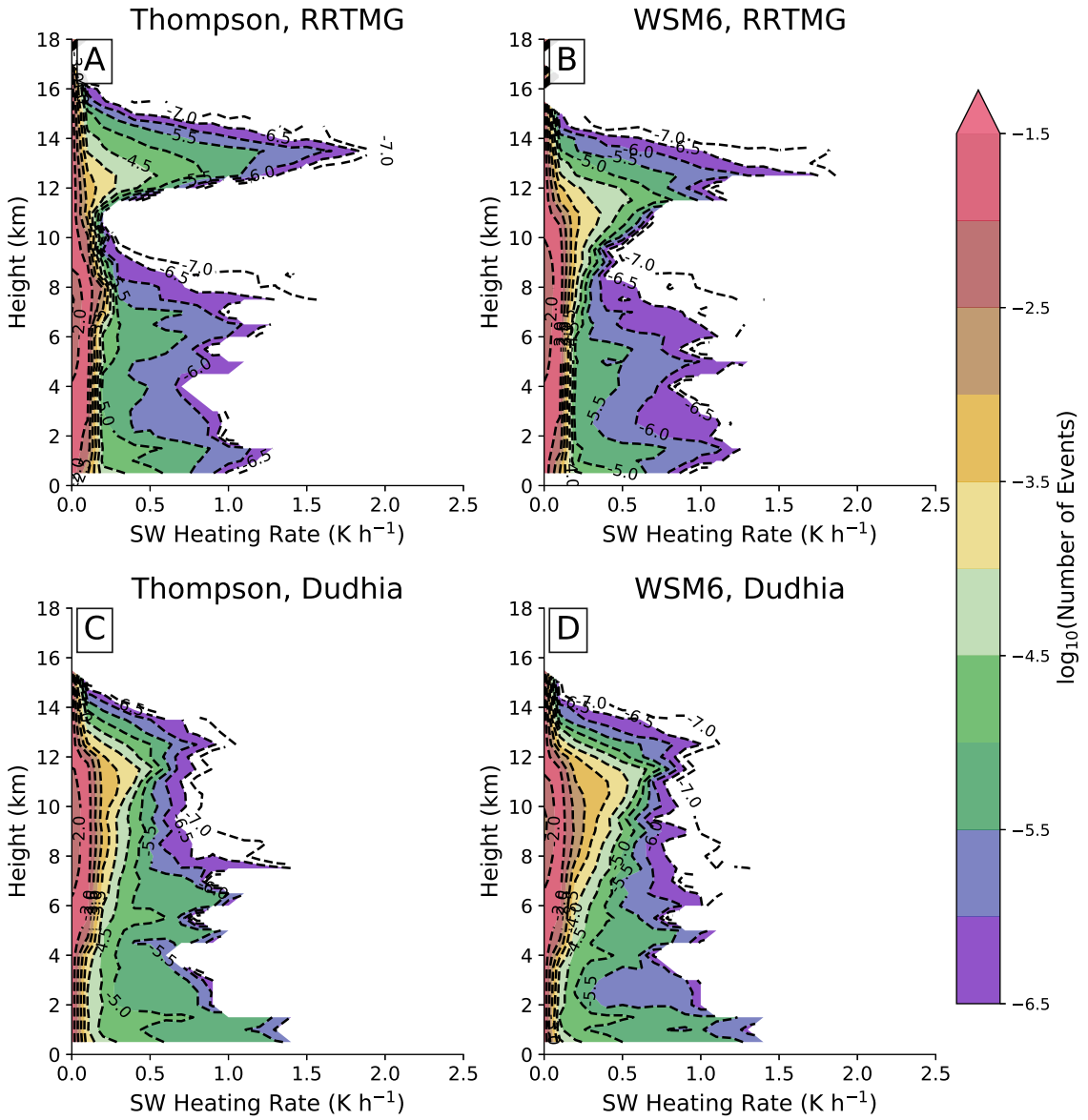

FIG. 5.13. The distribution of shortwave (SW) heating rates with height in the single domain experiments. The microphysics-shortwave radiation schemes of Thompson-RRTMG (a), WSM6-RRTMG (b), Thompson-Dudhia (c), and WSM6-Dudhia (d) are shown which are the same used in the simulations of Typhoon Kong-rey. Shortwave heating tendencies are binned every 0.1 K h^{-1}. Shaded is the log of the number of events in a bin which has been normalized by the total number of events. The dashed contour lines show the same value as what is shaded but extends to lower frequency events.

which alters the physical understanding. Regardless of the methodology, the lack of cirrus canopy in the WSM6-RRTMG scheme does not produce enough upper-level cirrus and thicker anvil cirrus in Typhoon Kong-rey to allow for a conclusive comparison of the mechanisms contributing to the diurnal cycle.

To diagnose the differences in the CFADs and the previously discussed structural differences in the experiments caused by the shortwave radiation and microphysics schemes, the distribution of heating rates with respect to height from the single domain experiments are analyzed in Fig. 5.13. The heating rates in the single domain experiment allows for a better comparison of the systematic differences between the schemes which are not dependent on the TC circulation differences. Equation 5.1 describes the shortwave heating rates ($\left(\frac{dT}{dt}\right)_{SW}$) where C_p is the specific heat content of air at constant pressure, ρ is the density of air, and F_{net} is the difference between the upwards and downwards fluxes from the layer.

$$\left(\frac{dT}{dt}\right)_{SW} = -\frac{1}{C_p \rho}\frac{dF_{net}}{dZ} \tag{5.1}$$

The heating rates in the RRTMG scheme maximize at a higher altitude ~13-13.5 km compared to the 12-12.5 km in the Dudhia scheme. The RRTMG scheme produces a sharper vertical gradient in the heating similar to what was shown in the idealized comparisons in Fig. 3.1 but this vertical gradient is sensitive to the microphysics scheme. The Thompson-RRTMG produces a local minimum in shortwave heating at an altitude of 11 km while the shortwave heating rates in the WSM6-RRTMG experiment gradually decreases to lower values. The differences at the upper-level are important for controlling the static stability of the upper-atmosphere and the longevity of cirrus clouds. The heating rates in the Dudhia schemes, regardless of the thickness of upper-level clouds tends to distribute heat further down into the cloud which may lead to weak ascent within those clouds, enhanced turbulence through the layer, and contribute to the longer lifetimes and areal extent that was shown in the Dudhia experiments in Fig. 5.9. The heating rates between 8-12 km are where larger frequency of stronger heating rates in the Dudhia scheme are found compared to the RRTMG schemes. The Dudhia scheme therefore leads to more pronounced in-cloud heating which could explain the drier regions at upper-levels shown in Fig. 5.7.

Below 9 km the shortwave heating rate distributions in Fig. 5.13 are fairly similar with the largest but uncommon heating rates around 1 K h^{-1}. The Dudhia experiments for some curious reason has the strongest heating rates found in any column occurring below 1500 m in the boundary layer. Since the heating rate due to a negative flux divergence is inversely related to the density of the layer, the same flux convergence in the upper-troposphere would cause larger heating rates than the same amount in the boundary layer. In order to generate these large heating rates close to the surface, an optically thick cloud with clear skies above are expected. One explanation for the the strong boundary layer heating

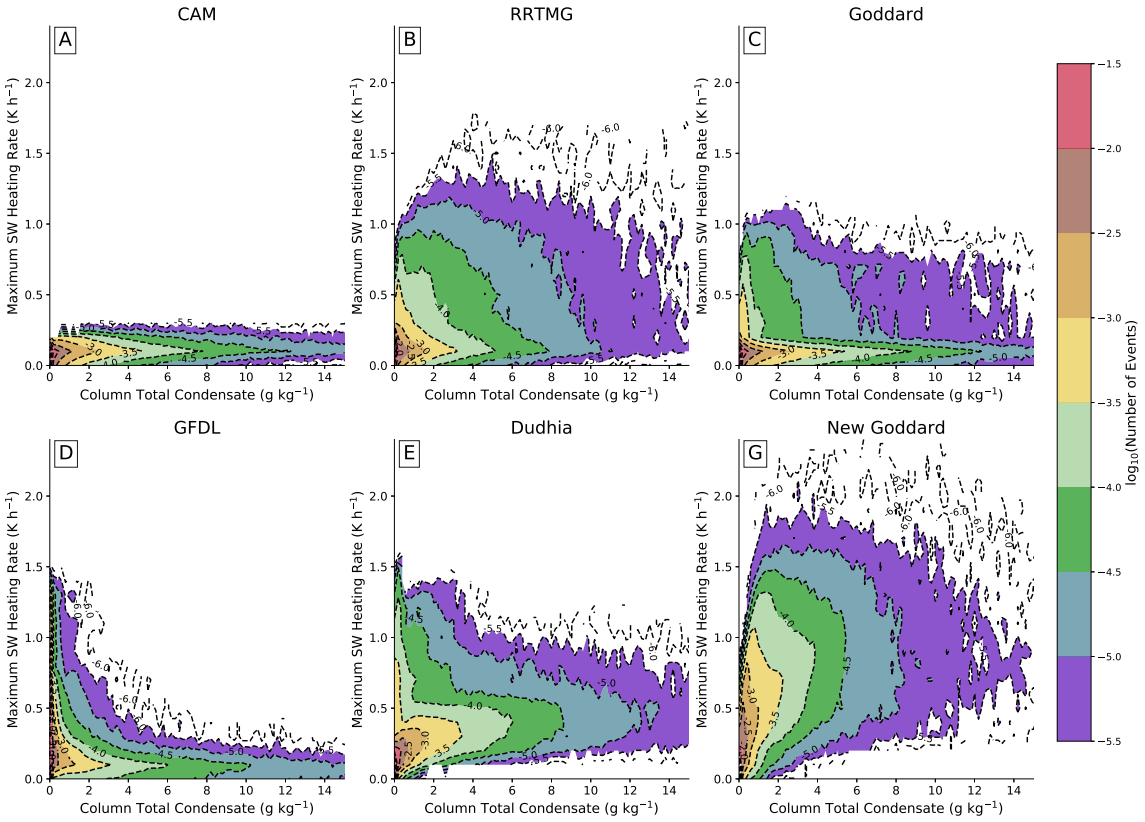

FIG. 5.14. The relationship between total condensate and maximum shortwave (SW) heating rate in a column. The Thompson microphysics is shown coupled with the shortwave radiation schemes of CAM (a), RRTMG (b), Goddard (c), GFDL (d), Dudhia (e), and New Goddard (g). Shaded is the log of the number of events in a bin which has been normalized by the total number of events.

in Dudhia could be related to the interaction with the YSU scheme; however, the RRTMG experiments do not have the same magnitudes of heating despite using the same scheme.

Although the simulations of Typhoon Kong-rey are computationally too expensive to evaluate the full sensitivity to shortwave radiation schemes, sensitivity tests are employed in a single domain experiment. To evaluate the sensitivity of the experiments to the shortwave radiation scheme the joint frequency distribution between column integrated total condensate and maximum shortwave radiation is shown for a number of experiments. Figure 5.14 shows the joint frequency distributions using different shortwave radiation schemes that all have the Thompson microphysics. Figure 5.14b and 5.14e corresponds to the Thompson-RRTMG and Thompson-Dudhia experiments which are the basis of the experiments and are included for reference with the other schemes. The Thompson-RRTMG experiment shows a broad relationship between the column total condensate and maximum shortwave radiation which is expected. Large heating rates above 1 K h^{-1} can occur in deep optically thick

clouds with large values of total condensate leading to more absorption within the thickest topmost layers. Clouds that have lower total condensates can still have large peak heating rates when they are elevated and the density of the layer is lower. As noted in Fig. 5.13, the peak shortwave heating in Thompson-Dudhia tended to occur in the boundary layer, which in Fig. 5.14 translates to columns with integrated total condensate values < 1 g kg^{-1}. The large heating rates in the boundary layer of the Thompson-Dudhia scheme appears to be an artifact that is also present in the GFDL and to some degree the Goddard schemes (Fig. 5.14c, d). It is unclear at this point what is causing this effect which was initially believed to be due to thin upper-tropospheric cirrus clouds or due to ozone absorption in the stratosphere (which is not present in Dudhia). More testing would be required to determine whether the YSU boundary layer scheme is driving the boundary layer heating and why it is not found in the RRTMG and New Goddard schemes. Overall the RRTMG and New Goddard schemes provide the most realistic relationship between column total condensate and maximum shortwave heating although the New Goddard scheme produces larger peak heating rates. The CAM and GFDL shortwave schemes have similar shortwave heating rates that are nearly fixed for thicker clouds which may be caused be a lack of coupling between the microphysics and radiation scheme.

In this section an attempt has been made to compare the observations from PISTON to the four experiments to evaluate the diurnal cycle of convection in the rainbands. The comparison is limited because of the lack of realistic upper-level clouds that were actively simulated in some experiments. The experiments tended to create a tripole upper-level difference in convective reflectivity that indicated both a weakening of convection during the day and a slight enhancement at times. The differences between nocturnal and daytime convection were fairly consistent between experiments with the largest differences between the Dudhia and RRTMG schemes arising at low levels. The Dudhia scheme was shown to heat the low-levels at larger rates than the RRTMG scheme and heat more within the cloud compared to the RRTMG scheme which tends to heat the upper-portion of the cloud layers.

5.6 Conclusions

Fovell et al. (2016) showed that radiation and cloud microphysics processes can affect tropical cyclone motion, the strength and breadth of the wind field, and characteristics of the anvil cloud and are therefore necessary to represent in operational forecast models. While Fovell et al. (2016) showed that the most important radiation-microphysics interaction in their experiments was due to longwave

warming in the anvil, the sensitivity between the microphysics and shortwave radiation was not well resolved because of averaging over the diurnal cycle. This chapter has shown that the cloud microphysics and shortwave radiation schemes play an important role in the forecasted intensity and structure of Typhoon Kong-rey. The large sensitivity appears to be related to a combination of factors at different time periods, where the biases in the microphysics schemes dominate the model differences over the first ∼36 hours and biases in the shortwave radiation amplify and dominate the differences between experiments at longer lead times.

The goal of this chapter was to compare high-resolution simulations with observations to improve our understanding of the radiative-microphysics interactions that influence tropical cyclone size and intensity forecasts. Among the four experiments using combinations of WSM6 and Thompson microphysics and RRTMG and Dudhia shortwave schemes, only the Thompson-RRTMG experiment was able to resolve similar intensification rates of Typhoon Kong-rey. The amount of convective and stratiform precipitation was influenced by both the microphysics and radiation schemes that were important for the intensification of Typhoon Kong-rey. Past studies have shown that single-moment microphysics schemes will underestimate stratiform precipitation compared to a double-moment scheme (Morrison et al. 2009); however, the RRTMG further reduces the stratiform precipitation compared to the Dudhia shortwave radiation. The Dudhia scheme also tended to create a drier upshear region that contributed to a weakening of the convection near the center and may have been caused by direct shortwave heating in the layers.

It has been known that hurricane intensification is difficult to forecast and it has been shown that vertical wind shear plays a role in the forecast errors. Chapter 2 showed that when low-moderate vertical-wind shear was present, the intensity forecast error distribution was wider. The experiments shown here suggests that the interactions between the microphysics and radiation scheme is a contributor to the uncertainty in the intensity and size forecasts. Rios-Berrios (2020) found that modified rain evaporation rates due to longwave radiation played a large role in the timing of RI in a sheared environment. Rios-Berrios (2020) used the WSM6 for the microphysics and RRTMG shortwave radiation scheme and concluded that full diurnal radiation led to reduced variability in intensification timing compared to when no radiation was concluded. Based on the experiments here, the simulations in Rios-Berrios (2020) likely would have underestimated the amount of stratiform precipitation which

could have further reduced the variability by strengthening the mid-level vorticity and further moistening the low-levels. Rios-Berrios (2020) also noted that the WSM6-RRTMG setup is common for idealized studies evaluating the effects of vertical wind shear on TC intensity, which warrants more study of the effects of vertical wind shear on TC intensification using more realistic double-moment or bin microphysics schemes.

One limitation of the present work is that the sensitivity of the experiments to stochastic perturbations of convection has not been assessed. Therefore the uncertainty and statistical significance of the intensity and structural evolution between the experiments is left unresolved due to computational limits. It would be reasonable to assume a small degree of uncertainty in regards to the intensity evolution of the four experiments shown here because the uncertainty is likely damped to some degree by the shortwave radiation (Trabing et al. 2019; Rios-Berrios 2020). Nonlinear interactions between radiation and cloud microphysics in environments of moderate vertical wind shear have yet to be fully explored and should be the focus of future studies. The high-resolution simulations presented here are computationally too expensive to be run as an ensemble without reducing temporal and spatial resolution. The multiple experiments using a single domain allows for further comparisons between model setups creating a simplified ensemble to evaluate the fundamental differences between the shortwave radiation schemes. The various shortwave radiation schemes and the location and magnitudes of heating play a large role in changing the diurnal variability constrained by the representation of the upper-level clouds.

The experiments were able to simulate an expansion of cold simulated brightness temperature near the beginning of the simulations but did not show evidence for diurnal pulses in the brightness temperatures. The experiments did, however, show evidence for diurnally driven outflow jets that seem to be correlated with radially outwards propagating rainbands in the axisymmetric means. The lack of connection between the simulated IR and the convection is partially related to the more focused radiative heating anomalies in RRTMG in the upper-level clouds compared to the broader vertical extent of heating in the Dudhia scheme. The Thompson experiments produce overall more uniform upper-level clouds with more snow/ice compared to the WSM6 experiments which is related to the fall speeds. Diurnal maxima in outflow tended to be more pronounced in the WSM6 experiments and could be a dynamic response to the shortwave heating (Navarro and Hakim 2016) or a response from the convection that is moving radially outwards. It is difficult to say which came first in this scenario and warrants further testing. Qualitatively the simulation of the outward moving convection coupled with

outflow jets are consistent with the observations from PISTON in each of the experiments. The explicit simulation of these convective rainbands indicate that the observations from PISTON were sampling a consistent feature of Typhoon Kong-rey's rainbands and not stochastic outer-rainband convection. The experiments also suggest that these areas of convection are to some extent predictable, although it should be noted that the experiments are not true forecast since the boundaries are forced by the GDAS analysis at each time.

In this chapter, it has been shown that the varying shortwave schemes can produce a fairly large difference in the relationship between maximum shortwave heating rates and column integrated total condensate. The implications of these heating rates are important for accurately simulating the upper-level cloud structures and diurnal oscillations in the clouds. Some of the shortwave schemes such as the CAM and GFDL schemes are not coupled to the Thompson microphysics scheme which leads to erroneous representations of the heating rates within clouds and may have contributed to the smaller effects of shortwave radiation found in select experiments of Fovell et al. (2016). In WRF version 3.9 there are 8 shortwave radiation schemes, 8 longwave radiation schemes, 25 variations of microphysics schemes, and 13 variations of boundary layer schemes resulting in 20,800 total combinations of these physics parameterization alone. To the authors knowledge (and WRF support team, K. Werner personal communication), there is no documentation on best practices for the use of various microphysics, radiation schemes, and boundary layer schemes. While it is important to have various schemes tuned for better representation of mid-latitude storm dynamics vs. tropical convection, the documentation of multi-physics interactions is lacking. More sensitivity tests and comparisons between model schemes are warranted and should be an important area for future work.

CHAPTER 6

CONCLUSIONS AND FUTURE WORK

The collection of projects in this dissertation aim to improve intensity and size forecasts through an improved understanding of the sensitivity of inner-core rainbands to shortwave radiation. In Chapter 2 it was shown that intensity forecast errors are larger for tropical cyclones that undergo rapid intensity changes, suggesteding that improved understanding of the processes that affect the inner-core convection will lead to improved intensity forecasts. Chapter 3 has shown that shortwave radiation plays a role in the strength of rainband convection which leads to changes in the timing of eyewall replacement cycles (ERCs) and associated intensity changes. Observational evidence from PISTON of diurnal oscillations in the strength of Typhoon Kong-rey's rainband convection and in the outflow layer associated with convectively coupled diurnal pulses was provided in Chapter 4. Chapter 5 showed that the interactions between the microphysics and shortwave radiation schemes modified the structure of the rainbands and the intensity of a simulated Typhoon Kong-rey.

In Chapter 2 the characteristics of official National Hurricane Center (NHC) intensity forecast errors are examined for the North Atlantic and East Pacific basins. It is shown how rapid intensification (RI) and rapid weakening (RW) influence yearly NHC forecast errors for forecasts between 12 to 48 hours in length. In addition to being the tail of the intensity change distribution, RI and RW are at the tails of the forecast error distribution. Yearly mean absolute forecast errors are positively correlated with the yearly number of RI/RW occurrences and explain roughly 20% of the variance in the Atlantic and 30% in the East Pacific. The higher occurrence of RI events in the East Pacific contributes to larger intensity forecast errors overall but a better probability of detection and success ratio. Statistically significant improvements to 24-h RI forecast biases have been made in the East Pacific and to 24-h RW biases in the Atlantic. Over-ocean 24-h RW events cause larger mean errors in the East Pacific that have not improved with time. Environmental predictors from the Statistical Hurricane Prediction Scheme (SHIPS) are used to diagnose what conditions lead to the largest RI and RW forecast errors on average. The forecast error distributions widen for both RI and RW when tropical systems experience low vertical wind shear, warm sea surface temperature, and moderate low-level relative humidity. Consistent with existing literature, the forecast error distributions suggest that improvements to our observational capabilities, understanding, and prediction of inner-core processes is paramount to both RI and RW prediction.

There has been a growing emphasis on communication of forecast uncertainty to improve the communication of risks to the public (Marks et al. 2019). While there is a “cone of uncertainty" for track forecasts based on previous years forecast errors, the intensity forecasts do not have such uncertainty estimates. The relationship between the intensity forecast errors and the environmental predictors suggests that the thermodynamic environment could be used to provide uncertainty estimates for intensity forecasts. Because the SHIPS developmental database uses the perfect prog forecast, Chapter 2 was unable to consider when the environmental forecast was different than expected. Future work therefore relating uncertainty estimates from the environmental predictors should also investigate the possibility of using select environmental predictors from an ensemble such as from the Global Ensemble Forecast System (GEFS). It would be interesting to compare whether diagnosing forecast uncertainty using the environmental variables from the ensembles would provide similar or better forecast uncertainties compared to the intensity variability in the ensemble itself.

The sensitivity of ERCs to shortwave radiation is examined in Chapter 3 by varying the solar constant and diurnal cycle at different times prior to an ERC using the Weather Research and Forecasting model. The magnitude of shortwave radiation plays an important role in modifying the timing of the ERC with non-linear interactions amplifying the ERC formation differences at longer lead-times. Shortwave radiation has a delaying effect on the ERC primarily through its modifications of the distribution of convective and stratiform heating profiles in the rainbands. Shortwave radiation reduces the amount and strength of convection in the model domain which increases the amount of stratiform precipitation that is weaker in magnitude. The primary mechanism by which shortwave radiation reduces the intensity and frequency of convection in the rainbands is through heating of the mid-upper troposphere which stabilizes the region and reduces convective available potential energy. Although ERCs are largely driven by inner-core processes, the overall negative effect of shortwave radiation on the inner rainbands suggests that ERCs may be more prevalent or occur faster at night. Future work using the climatology of ERCs shown in Sitkowski et al. (2011), or the resulting Microwave-based Probability of ERC (M-PERC; Kossin and Sitkowski 2012) logistic regression model, could be used to further assess the role of the diurnal cycle on ERCs.

A growing body of work has documented the existence of diurnal oscillations in the tropical cyclone outflow layer, which have been examined primarily using satellites or numerical models. Detailed observations and case study analyses of diurnal pulses are lacking. Questions remain on the vertical extent of diurnal pulses and whether diurnal pulses are coupled to convective bands or constrained to the

outflow layer. The cirrus canopy itself is not well understood and how it effects the diurnal cycle of convection in the tropical cyclone rainbands. In Chapter 4, observations collected during the Propagation of Intraseasonal Tropical Oscillations (PISTON) field campaign show evidence of diurnal oscillations in the upper-level clouds of Typhoon Kong-rey (2018). Over a 3.5 day period where a broad distribution of cold upper-level clouds was overhead, detailed observations of Typhoon Kong-rey's rainbands show that convection had reduced echo tops but overall enhanced reflectivity and differential reflectivity aloft. Shortwave heating in the upper-levels increased the stability profile during the day which could help to explain the diurnal differences in convective structure. Under the cirrus canopy, nocturnal convection was deeper and daytime convection shallower which was the opposite of the rest of the PISTON dataset. Diurnal oscillations were found to be coupled to radially outward propagating convective rainbands that were preceded ∼6 hours by outflow jets. The cooling pulses occurred earlier than suggested by previous studies and were asymmetric spatially which is likely due to a combination of the vertical wind shear and storm intensity.

With further support that diurnal pulses are convectively coupled from the observations during PISTON, future work should explore the relationship between diurnal pulses and eyewall replacement cycles. Eyewall replacement cycles which feature an axisymmeterization of convection associated with the primary rainband, seem to be relatively stationary features that tend to cause a weakening of convection in the primary eyewall and move radially inward. In contrast, the convective component of the usually axisymmetric diurnal pulses move radially outward and is not thought to have any effect on the strength of the primary eyewall. One could speculate that the location of the inner-rainband in reference to the rapid filamentation zone of the tropical cyclone will play a large role in whether the rainband moves radially inward or outward; however, the degree to which the intensity of the rainband matters is unclear. Future work should investigate whether ERCs and diurnal pulses can occur simultaneously. O'Neill et al. (2017) showed using an idealized model that diurnal waves propagating in TCs were interrupted by ERCs, which suggests that diagnosing diurnal pulses in realtime could offer added benefits to short term forecasts.

Although the experiments in Chapter 5 were unable to explicitly resolve diurnal pulses in the brightness temperatures of the simulations of Typhoon Kong-rey, the diurnal pulses were present in the outflow and tended to be to some degree convectively coupled. The diurnal pulses may have been present but not accounted for in other modeling studies (Tang et al. 2017; Trabing et al. 2019; Smith et al. 2020) and should be a topic of further research. Questions also arise as to how important simulating diurnal

pulses are to forecasting tropical cyclone intensity change and size, although the interactions between the radiation and cloud microphysics clearly matter. It has been commonly noted that in studies that include radiation, there is more active rainband convection and the simulations tend to develop larger tropical cyclone wind fields (Bu et al. 2014; Trabing et al. 2019). Given that the surrounding moisture field has been shown to be a constraint on storm size (Martinez et al. 2020), what role does outward moving rainbands associated with diurnal pulses play in moving moisture and vorticity outwards? It is unknown whether outward propagating rainbands could be a contributor to larger wind fields and broader areas of TC precipitation noted in past studies. The radially outward propagating rainbands on diurnal time scales could subsequently be predicted leading to not only better quantitative precipitation forecasts, but also better forecasts of storm size.

Aberson, S. D., A. Aksoy, K. J. Sellwood, T. Vukicevic, and X. Zhang, 2015: Assimilation of high-resolution tropical cyclone observations with an ensemble kalman filter using HEDAS: Evaluation of 2008–11 HWRF forecasts. *Mon. Wea. Rev.*, **143**, 511–523, doi: 10.1175/MWR-D-14-00138.1.

Bell, M. M., 2019: *nsf-lrose/lrose-blaze: lrose-blaze-20190105*. URL `https://doi.org/10.5281/ZENODO.2532758`.

Bell, M. M. and M. T. Montgomery, 2019: Mesoscale Processes during the Genesis of Hurricane Karl (2010). *J. Atmos. Sci.*, **76 (8)**, 2235–2255, doi: 10.1175/JAS-D-18-0161.1.

Bellenger, H., Y. N. Takayubu, T. Ushiyuma, and K. Yoneyama, 2010: Role of diurnal warm layers in the diurnal cycle of convection over the tropical indian ocean during mismo. *Mon. Wea. Rev.*, **138**, 2426–2433.

Bhatia, K. T. and D. S. Nolan, 2013: Relating the skill of tropical cyclone intensity forecasts to the synoptic environment. *Wea. Forecasting*, **28**, 961–980, doi: 0.1175/WAF-D-12-00110.1.

Brown, B. R., M. M. Bell, and A. J. Frambach, 2016: Validation of simulated hurricane drop size distributions using polarimetric radar. *Geophys. Res. Lett.*, **43**, 910–917, doi: 10.1002/2015GL067278.

Browner, S. P., W. L. Woodley, and C. G. Griffith, 1977: Diurnal Oscillation of the Area of Cloudiness Associated with Tropical Storms. *Mon. Wea. Rev.*, **105 (7)**, 856–864, doi: 10.1175/1520-0493(1977)105<0856:DOOTAO>2.0.CO;2.

Bu, Y. P., R. G. Fovell, and C. K. L., 2014: Influence of cloud-radiative forcing on tropical cyclone structure. *J. Atmos. Sci.*, **71**, 1644–1662, doi: 10.1175/JAS-D-13-00265.1.

Cangialosi, J. P., E. Blake, M. DeMaria, A. Penny, A. Latto, E. N. Rappaport, and V. Tallapragada, 2020: Recent progress in tropical cyclone intensity forecasting at the national hurricane center. *Wea. Forecasting*, 1–30, doi: 10.1175/WAF-D-20-0059.1.

Cangialosi, J. P. and J. L. Franklin, 2014: *2013 National Hurricane Center Forecast verification report*. NOAA/National Hurricane Center, [Available online at : `https://www.nhc.noaa.gov/verification/pdfs/Verification_2013.pdf`].

Cheng, C.-J. and C.-C. Wu, 2018: The role of wishe in secondary eyewall formation. *J. Atmos. Sci.*, **75**, 3823–3841.

Chou, M. D. and M. J. Suarez, 1994: *An efficient thermal infrared radiation parameterization for use in general circulation models*. NASA Tech. Memo.

Chou, M. D. and M. J. Suarez, 1999: *A solar radiation parameterization for atmospheric studies*. NASA Tech. Memo.

Ciesielski, P. E., P. H. Haertel, R. H. Johnson, J. Wang, and S. Loehrer, 2011: Developing high-quality field program sounding datasets. *Bull. Amer. Meteor. Soc.*, **93**, 325–336.

Collins, W. D., et al., 2006: The Formulation and Atmospheric Simulation of the Community Atmosphere Model Version 3 (CAM3). *J. Climate*, **19 (11)**, 2144–2161, doi: 10.1175/JCLI3760.1.

Craig, G., 1996: Numerical experiments on radiation and tropical cyclones. *Quart. J. Roy. Meteor. Soc.*, **122**, 415–422, doi: 10.1002/qj.49712253006.

DeMaria, M., J. A. Knaff, and J. Kaplan, 2006: On the decay of tropical cyclone winds crossing narrow landmasses. *J. Appl. Meteor. Climatol.*, **45**, 491–499.

DeMaria, M., M. Mainelli, L. K. Shay, J. A. Knaff, and J. Kaplan, 2005: Further improvements to the Statistical Hurricane Intensity Prediction Scheme (SHIPS). *Wea. Forecasting*, **20**, 531–543.

DeMaria, M., C. R. Sampson, J. A. Knaff, and K. D. Musgrave, 2014: Is tropical cyclone intensity guidance improving? *Bull. Amer. Meteor. Soc.*, **95**, 387–398, doi: 10.1175/BAMS-D-12-00240.1.

Didlake, A. C. and M. J. Kumjan, 2018: Examining storm asymmetries in hurricane irma (2017) using polarimetric radar observations. *Geophys. Res. Lett.*, **45**, 13,513–13,522.

Didlake, A. C., J. D. Reasor, R. F. Rogers, and L. W.C., 2018: Dynamics of the transition from spiral rainbands to a secondary eyewall in Hurricane Earl (2010). *J. Atmos. Sci.*, **75**, 2909–2929.

Ditchek, S. D., K. L. Corbosiero, R. G. Fovell, and J. Molinari, 2019b: Electrically active tropical cyclone diurnal pulses in the atlantic basin. *Mon. Wea. Rev.*, **147**, 3595–3607.

Ditchek, S. D., J. Molinari, K. L. Corbosiero, and R. G. Fovell, 2019a: An objective climatology of tropical cyclone diurnal pulses in the atlantic basin. *Mon. Wea. Rev.*, **147**, 592–605.

Doyle, J. D., J. R. Moskaitis, and Coauthors, 2017: A view of tropical cyclones from above. *Bull. Amer. Meteor. Soc.*, **74**, 2113–2134, doi: 10.1175/BAMS-D-16-0055.1.

Dudhia, J., 1989: Numerical study of convection observed during the winter monsoon experiment using a mesoscale two dimensional model. *J. Atmos. Sci.*, **46**, 3077–3107, doi: 10.1175/1520-0469(1989)046<3077:NSOCOD>2.0.CO;2.

Dunion, J. P., C. D. Thorncroft, and N. D. S., 2019: Tropical cyclone diurnal cycle signals in a hurricane nature run. *Mon. Wea. Rev.*, **147**, 363–388, doi: 10.1175/MWR-D-18-0130.1.

Dunion, J. P., C. D. Thorncroft, and V. C. S., 2014: The tropical cyclone diurnal cycle of mature hurricanes. *Mon. Wea. Rev.*, **142**, 3900–3919, doi: 10.1175/MWR-D-13-00191.1.

Duran, P. and J. Molinari, 2016: Upper-tropospheric low richardson number in tropical cyclones: Sensitivity to cyclone intensity and the diurnal cycle. *J. Atmos. Sci.*, **73**, 545–554, doi: 10.1175/JAS-D-15-0118.1.

Duran, P. and J. Molinari, 2019: Tropopause evolution in a rapidly intensifying tropical cyclone: A static stability budget analysis in an idealized axisymmetric framework. *J. Atmos. Sci.*, **76**, 209–229, doi: 10.1175/JAS-D-18-0097.1.

Eliassen, A., 1952: Slow thermally or frictionally controlled meridional circulations in a circular vortex. *Astrophys. Norv.*, **5**, 19–60.

Emanuel, K. and F. Zhang, 2016: On the predictability and error sources of tropical cyclone intensity forecasts. *J. Atmos. Sci.*, **73**, 3739–3747, doi: 10.1175/JAS-D-16-0100.1.

Fels, S. B. and M. D. Schwarzkopf, 1981: An efficient, accurate algorithm for calculating CO2 15 μm band cooling rates. *Journal of Geophysical Research: Oceans*, **86 (C2)**, 1205–1232, doi: 10.1029/JC086iC02p01205.

Fovell, R. G., K. L. Bu, Y. P. Corbosiero, W. Tung, Y. Cao, H. Kuo, L. Hsu, and H. Su, 2016: Influence of cloud microphysics and radiation on tropical cyclone structure and motion. *Meteor. Monogr.*, **56**, 11.1–11.27, doi: 10.1175/AMSMONOGRAPHS-D-15-0006.1.

Fovell, R. G., K. L. Corbosiero, A. Seifert, and K.-N. Liou, 2010: Impact of cloud-radiative processes on hurricane track. *Geophys. Res. Lett.*, **37**, doi: 10.1029/2010GL042691.

Gall, R., J. Franklin, F. Marks, E. N. Rappaport, and F. Toepfer, 2013: The hurricane forecast improvement project. *Bull. Amer. Meteor. Soc.*, **94**, 329–343, doi: 10.1175/BAMS-D-12-00071.1.

Gray, W. M. and R. W. Jacobson, Jr., 1977: Diurnal variation of deep cumulus convection. *Mon. Wea. Rev.*, **105**, 1171–1188, doi: 10.1175/1520-0493(1977)105,1171:DVODCC.2.0.CO;2.

Hendricks, E. A., M. S. Peng, B. Fu, and T. Li, 2010: Quantifying environmental control of tropical cyclone intensity change. *Mon. Wea. Rev.*, **138**, 3243–3271, doi: 10.1175/2010MWR3185.1.

Hong, G., G. Heygster, and R. C. A. M., 2006a: Effect of cirrus clouds on the diurnal cycle of tropical deep convective clouds. *J. Geophys. Res.*, **111**, D06 209, doi: 10.1029/2005JD006208.

Hong, S.-Y. and J.-O. J. Lim, 2006: The WRF Single-Moment 6-Class Microphysics Scheme (WSM6). *J. Korean Meteor. Soc.*, **42 (2)**, 129–151.

Hong, S.-Y., Y. Noh, and J. Dudhia, 2006b: A new vertical diffusion package with an explicit treatment of entrainment processes. *Mon. Wea. Rev.*, **134**, 2318–2341, doi: 10.1175/MWR3199.1.

Houze, J., Robert A., S. A. Rutledge, T. J. Matejka, and P. V. Hobbs, 1981: The Mesoscale and Microscale Structure and Organization of Clouds and Precipitation in Midlatitude Cyclones. III: Air Motions and Precipitation Growth in a Warm-Frontal Rainband. *J. Atmos. Sci.*, **38 (3)**, 639–649, doi: 10.1175/1520-0469(1981)038<0639:TMAMSA>2.0.CO;2.

Houze, R. A. J., 2010: Review: Clouds in tropical cyclones. *Mon. Wea. Rev.*, **138**, 293–344, doi: 10.1175/2009MWR2989.1.

Iacono, M. J., J. S. Delamere, E. J. Mlawer, M. W. Shepard, S. A. Clough, and W. D. Collins, 2008: Radiative forcing by long-lived greenhouse gases: Calculations with the AER radiative transfer models. *J. Geophys. Res.*, **113**.

Irish, J. L., D. T. Resio, and J. J. Ratcliff, 2008: The Influence of Storm Size on Hurricane Surge. *J. Phys. Oceanogr.*, **38**, 2003–2013, doi: 10.1175/2008JPO3727.1.

Jiménez, P. A., J. Dudhia, J. F. González-Rouco, J. Navarro, J. P. Montávez, and E. García-Bustamante, 2012: A Revised Scheme for the WRF Surface Layer Formulation. *Mon. Wea. Rev.*, **140 (3)**, 898–918,

doi: 10.1175/MWR-D-11-00056.1.

Jones, S. C., P. A. Harr, and Coauthors, 2003: The extratropical transition of tropical cyclones:Forecast challenges, current understanding, and future directions. *Wea. Forecasting*, **18**, 1052–1092.

Kaplan, J. and M. DeMaria, 1995: A simple empirical model for predicting the decay of tropical cyclone winds after landfall. *J. Appl. Meteor.*, **34**, 2499–2512.

Kaplan, J. and M. DeMaria, 2003: Large-scale characteristics of rapidly intensifying tropical cyclones in the north atlantic basin. *Wea. Forecasting*, **18**, 1093–1108.

Kaplan, J., M. DeMaria, and J. A. Knaff, 2010: A revised tropical cyclone rapid intensification index for the atlantic and eastern north pacific basins. *Wea. Forecasting*, **25**, 220–241, doi: 10.1175/2009WAF2222280.1.

Kaplan, J., C. M. Rozoff, and Coauthors, 2015: Evaluating environmental impacts on tropical cyclone rapid intensification predictability utilizing statistical models. *Wea. Forecasting*, **30**, 1374–1396, doi: 10.1175/WAF-D-15-0032.1.

Knaff, J. A., C. J. Slocum, and K. D. Musgrave, 2019: Quantification and exploration of diurnal oscillations in tropical cyclones. *Mon. Wea. Rev.*, **147**, 2105–2121, doi: 10.1175/MWR-D-18-0379.1.

Komaromi, W. A. and J. D. Doyle, 2017: Tropical Cyclone Outflow and Warm Core Structure as Revealed by HS3 Dropsonde Data. *Mon. Wea. Rev.*, **145 (4)**, 1339–1359, doi: 10.1175/MWR-D-16-0172.1.

Kossin, J. P., 2002: Daily Hurricane Variability Inferred from GOES Infrared Imagery. *Mon. Wea. Rev.*, **130 (9)**, 2260–2270, doi: 10.1175/1520-0493(2002)130<2260:DHVIFG>2.0.CO;2.

Kossin, J. P. and M. DeMaria, 2016: Reducing operational hurricane intensity forecast errors during eyewall replacement cycles. *Wea. Forecasting*, **31**, 601–607, doi: 10.1175/WAF-D-15-0123.1.

Kossin, J. P. and M. Sitkowski, 2012: Predicting Hurricane Intensity and Structure Changes Associated with Eyewall Replacement Cycles. *Wea. Forecasting*, **27 (2)**, 484–488, doi: 10.1175/WAF-D-11-00106.1.

Li, Q. and Y. Wang, 2012: Formation and quasi-periodic behavior of outer spiral rainbands in a numerically simulated tropical cyclone. *J. Atmos. Sci.*, **69**, 997–1020.

Liang, J., L. Wu, G. Gu, and Q. Liu, 2016: Rapid weakening of Typhoon Chan-Hom (2015) in a monsoon gyre. *J. Geophys. Res.*, **121**, 9508–9520, doi: 10.1002/2016JD025214.

Marks, F. J., N. Kurkowski, M. DeMaria, and M. Brennan, 2019: *Hurricane Forecast Improvement Project Years Ten to Fifteen Strategic Plan*. NOAA.

Martinez, J., M. M. Bell, R. F. Rogers, and J. D. Doyle, 2019: Axisymmetric Potential Vorticity Evolution of Hurricane Patricia (2015). *Journal of the Atmospheric Sciences*, **76 (7)**, 2043–2063, doi: 10.1175/JAS-D-18-0373.1.

Martinez, J., C. Nam, and M. Bell, 2020: On the contributions of incipient vortex circulation and environmental moisture to tropical cyclone expansion. *J. Geophys. Res.*

Mecikalski, J. R. and G. J. Tripoli, 1998: Inertial Available Kinetic Energy and the Dynamics of Tropical Plume Formation. *Mon. Wea. Rev.*, **126 (8)**, 2200–2216, doi: 10.1175/1520-0493(1998)126<2200:IAKEAT>2.0.CO;2.

Melhauser, C. and F. Zhang, 2014: Diurnal radiation cycle impact on the pregenesis environment of hurricane karl (2010). *J. Atmos. Sci.*, **71**, 1241–1259, doi: 10.1175/JAS-D-13-0116.1.

Merrill, R. T., 1988: Characteristics of the Upper-Tropospheric Environmental Flow around Hurricanes. *Journal of the Atmospheric Sciences*, **45 (11)**, 1665–1677, doi: 10.1175/1520-0469(1988)045<1665:COTUTE>2.0.CO;2.

Merritt, E. and R. Wexler, 1967: Cirrus canopies in tropical storms. *Mon. Wea. Rev.*, **95**, 111–120, doi: 10.1175/1520-0493(1967)095<0111:CCITS>2.3.CO;2.

Mlawer, E. J., S. J. Taubman, P. D. Brown, M. J. Iacono, and S. A. Clough, 1997: Radiative transfer for inhomogeneous atmospheres: RRTM, a validated correlated-k model for the longwave. *J. Geophys. Res.*, **102**, 16 663–16 682, doi: 10.1029/97JD00237.

Morrison, H., G. Thompson, and V. Tatarskii, 2009: Impact of Cloud Microphysics on the Development of Trailing Stratiform Precipitation in a Simulated Squall Line: Comparison of One- and Two-Moment Schemes. *Monthly Weather Review*, **137 (3)**, 991–1007, doi: 10.1175/2008MWR2556.1.

Muramatsu, T., 1983: Diurnal-variations of satellite-measured tbb areal distribution and eye diameter of mature typhoons. *J. Meteor. Soc. Japan*, **61**, 77–90.

Na, W., J. L. McBride, X.-H. Zhang, and Y.-H. Duan, 2018: Understanding biases in tropical cyclone intensity forecast error. *Wea. Forecasting*, **33**, 129–137, doi: 10.1175/WAF-D-17-0106.1.

Navarro, E. L. and G. J. Hakim, 2016: Idealized numerical modeling of the diurnal cycle of tropical cyclones. *J. Atmos. Sci.*, **73**, 4189–4201, doi: 10.1175/JAS-D-15-0349.1.

Navarro, E. L., G. J. Hakim, and H. E. Willoughby, 2017: Balanced response of an axisymmetric tropical cyclone to periodic diurnal heating. *J. Atmos. Sci.*, **74**, 3325–3337, doi: 10.1175/JAS-D-16-0279.1.

Nicholls, M. E., 2015: An investigation of how radiation may cause accelerated rates of tropical cyclogenesis and diurnal cycles of convective activity. *Atmos. Chem. Phys.*, **15**, 9003–9029, doi: 10.5194/acp-15-9003-2015.

Nolan, D. S., 2007: What is the trigger for tropical cyclogenesis? *Aust. Meteor. Mag.*, **56**, 241–266.

Nystrom, R. G. and F. Zhang, 2019: Practical uncertainties in the limited predictability of the record-breaking intensification of hurricane patricia (2015). *Mon. Wea. Rev.*, **147**, 3535–3556, doi: 10.1175/MWR-D-18-0450.1.

O'Neill, M. E., D. Perez-Betancourt, and A. A. Wing, 2017: Accessible environments for diurnal-period waves in simulated tropical cyclones. *Journal of the Atmospheric Sciences*, **74 (8)**, 2489–2502, doi: 10.1175/JAS-D-16-0294.1.

Pasch, R. J., A. B. Penny, and R. Berg, 2019: *National Hurricane Center Tropical Cyclone Report: Hurricane Maria (AL152017)*. National Hurricane Center, [Available online at : `https://www.nhc.noaa.gov/data/tcr/AL152017_Maria.pdf`].

Pendergrass, A. G. and H. E. Willoughby, 2009: Diabatically induced secondary flows in tropical cyclones. part I: Quasi-steady forcing. *Mon. Wea. Rev.*, **137**, 805–821.

Powell, M. D. and T. A. Reinhold, 2007: Tropical Cyclone Destructive Potential by Integrated Kinetic Energy. *Bull. Amer. Meteor. Soc.*, **88 (4)**, 513–526, doi: 10.1175/BAMS-88-4-513.

Powell, S. W., R. H. Houze, and S. R. Brodzik, 2016: Rainfall-type categorization of radar echoes using polar coordinate reflectivity data. *J. Atmos. Oceanic Technol.*, **33**, 523–538, doi: 10.1175/JTECH-D-15-0135.1.

Rappaport, E. N., J. L. Franklin, A. B. Schumacher, M. DeMaria, L. K. Shay, and E. J. Gibney, 2010: Tropical cyclone intensity change before u.s. gulf coast landfall. *Wea. Forecasting*, **25**, 1380–1396, doi: 10.1175/2010WAF2222369.1.

Razin, N., P. Brown, J. Knaff, K. Musgrave, and M. Bell, 2019: *Tropical Cyclone Precipitation, Infrared, Microwave, and Environmental Database (TC PRIMED)*. 2019 CoRP Science Symposium, College Park, MD .

Rios-Berrios, R., 2020: Impacts of Radiation and Cold Pools on the Intensity and Vortex Tilt of Weak Tropical Cyclones Interacting with Vertical Wind Shear. *J. Atmos. Sci.*, **77 (2)**, 669–689.

Rivoire, L., T. Birner, J. A. Knaff, and N. Tourville, 2020: Quantifying the Radiative Impact of Clouds on Tropopause Layer Cooling in Tropical Cyclones. *J. Climate*, **33 (15)**, 6361–6376, doi: 10.1175/JCLI-D-19-0813.1.

Rogers, R. F., et al., 2017: Rewriting the Tropical Record Books: The Extraordinary Intensification of Hurricane Patricia (2015). *Bulletin of the American Meteorological Society*, **98 (10)**, 2091–2112, doi: 10.1175/BAMS-D-16-0039.1.

Rotunno, R. and K. A. Emanuel, 1987: An air-sea interaction theory for tropical cyclones. Part II: Evolutionary study using a nonhydrostatic axisymmetric numerical model. *J. Atmos. Sci.*, **44**, 542–561.

Rozoff, C. M. and J. P. Kossin, 2011: New probabilistic forecast models for the prediction of tropical cyclone rapid intensification. *Wea. Forecasting*, **26**, 677–689, doi: 10.1175/WAF-D-10-05059.1.

Ruppert, J. H. and M. E. O'Neill, 2019: Diurnal cloud and circulation changes in simulated tropical cyclones. *Geophys. Res. Lett.*, **46**, 502–511, doi: 10.1029/2018GL081302.

Rutledge, S. A., V. Chandrasekar, B. Fuchs, J. George, F. Junyent, B. Dolan, P. C. Kennedy, and K. Drushka, 2019: Sea-pol goes to sea. *Bull. Amer. Meteor. Soc.*, **100**, 2285–2301, doi: 10.1175/BAMS-D-18-0233.1.

Schott, T., C. Landsea, and Coauthors, 2012: *The Saffir-Simpson hurricane wind scale*. NOAA/National Hurricane Center, [Available online at : `http://www.nhc.noaa.gov/pdf/sshws.pdf`].

Sitkowski, M., J. P. Kossin, and C. M. Rozoff, 2011: Intensity and structure changes during hurricane eyewall replacement cycles. *Mon. Wea. Rev.*, **139**, 3829–3847.

Skamarock, W. C., J. Klemp, and Coauthors, 2008: *A description of the Advanced Research WRF version 3*. NCAR Tech. Note NCAR/TN-475+STR, doi: 10.5065/D68S4MVH.

Smith, W. P., M. E. Nichols, and R. A. Pielke, 2020: The role of radiation in accelerating tropical cyclogenesis in idealized simulations. *J. Atmos. Sci.*, **77**, 1261–1277.

Steiner, M. R., R. A. Houze, and S. E. Yuter, 1995: Climatological characterization of three-dimensional storm structure from operational radar and rain gauge data. *J. Appl. Meteor.*, **34**, 1978–2007, doi: 10.1175/1520-0450(1995)034,1978:CCOTDS.2.0.CO;2.

Steranka, J., E. Rodgers, and R. Gentry, 1977: The role of equivalent blackbody temperature in the study of atlantic ocean tropical cyclone. *Mon. Wea. Rev.*, **112**, 2338–2344, doi: 10.1175/1520-0493(1984)112,2338:TDVOAO.2.0.CO;2.

Stevenson, S. N., K. L. Corbosiero, and S. F. Abarca, 2016: Lightning in eastern north pacific tropical cyclones: A comparison to the north atlantic. *Mon. Wea. Rev.*, **144 (1)**, 225–239, doi: 10.1175/MWR-D-15-0276.1.

Sundqvist, H., 1970: Numerical simulation of the development of tropical cyclones with a ten-level model. Part II. *Tellus*, **5**, 504–510.

Tang, B. and K. Emanuel, 2010: Midlevel Ventilation's Constraint on Tropical Cyclone Intensity. *J. Atmos. Sci.*, **67 (6)**, 1817–1830, doi: 10.1175/2010JAS3318.1.

Tang, X., Z. Tan, J. Fang, Q. Sun, and F. Zhang, 2017: Impacts of diurnal radiation cycle on secondary eyewall formation. *J. Atmos. Sci.*, **74**, 3079–3098, doi: 10.1175/JAS-D-17-0020.1.

Tang, X. and F. Zhang, 2016: Impacts of the diurnal radiation cycle on the formation, intensity, and structure of Hurricane Edouard (2014). *J. Atmos. Sci.*, **73**, 2871–2892, doi: 10.1175/JAS-D-15-0283.1.

Thompson, G. and T. Eidhammer, 2014: A study of aerosol impacts on clouds and precipitation development in a large winter cyclone. *J. Atmos. Sci.*, **71**, 3636–3658, doi: 10.1175/JAS-D-13-0305.1.

Tiedtke, M., 1989: A comprehensive mass flux scheme for cumulus parameterization in large-scale models. *Mon. Wea. Rev.*, **117**, 1779–800, doi: 10.1175/1520-0493(1989)117<1779:ACMFSF>2.0.CO;2.

Trabing, B. C., M. M. Bell, and B. R. Brown, 2019: Impacts of radiation and upper tropospheric temperatures on tropical cyclone structure and intensity. *J. Atmos. Sci.*, **76**, 3079–3098, doi: 10.1175/JAS-D-16-0165.1.

Van Sang, N., R. K. Smith, and M. T. Montgomery, 2008: Tropical cyclone intensification and predictability in three dimensions. *Quart. J. Roy. Meteor. Soc.*, **134**, 563–582, doi: 10.1002/qj.235.

Wang, Y., 2009: How do outer spiral rainbands affect tropical cyclone structure and intensity? *J. Atmos. Sci.*, **66**, 1250–1273.

Wang, Y.-F. and Z.-M. Tan, 2020: Outer Rainbands–Driven Secondary Eyewall Formation of Tropical Cyclones. *J. Atmos. Sci.*, **77 (6)**, 2217–2236, doi: 10.1175/JAS-D-19-0304.1, URL `https://doi.org/10.1175/JAS-D-19-0304.1`.

WMO, 1957: Definition of the tropopause. *WMO Bull.*, **6**, 136.

Wood, K. M. and E. A. Ritchie, 2015: A definition for rapid weakening of North Atlantic and eastern North Pacific tropical cyclones. *Geophys. Res. Lett.*, **10**, 091–097, doi: 10.1002/2015GL066697.

Wu, Q. and Z. Ruan, 2016: Diurnal variations of the areas and temperatures in tropical cyclone clouds. *Quart. J. Roy. Meteor. Soc.*, **142**, 2788–2796, doi: 10.1002/qj.2868.

Xu, J. and Y. Wang, 2010: Sensitivity of tropical cyclone inner-core size and intensity to the radial distribution of surface entropy flux. *J. Atmos. Sci.*, **67**, 1831–1852.

Xu, K.-M. and D. A. Randall, 1995: Impact of interactive radiative transfer on the macroscopic behavior of cumulus ensembles. part II: Mechanisms for cloud-radiation interactions. *J. Atmos. Sci.*, **52**, 800–817, doi: 10.1175/1520-0469(1995)052,0800: IOIRTO.2.0.CO;2.

Yuter, S. E. and R. A. Houze, 1997: Measurements of raindrop size distributions over the pacific warm pool and implications for z–r relations. *J. Appl. Meteor.*, **36**, 847–867, doi: 10.1175/ 1520-0450(1997)036,0847:MORSDO.2.0.CO;2.

Zhang, J., J. P. Dunion, and D. S. Nolan, 2020: In situ observations of the diurnal variation in the boundary layer of mature hurricanes. *Geophys. Res. Lett.*, **47**, 2019GL086 206, doi: 10.1029/2019GL086206.

Zhou, S., Y. Ma, and X. Ge, 2016: Impacts of the diurnal cycle of solar radiation on spiral rainbands. *Adv. Atmos. Sci.*, **33**, 1085–1095, doi: 10.1007/s00376-016-5229-5.

Zhu, Z. and P. Zhu, 2014: The role of outer rainband convection in governing the eyewall replacement cycle in numerical simulations of tropical cyclones. *J. Geophys. Res.*, **119**, 8048–8072.